Pattern formation on Si surfaces by low-energy ion beam erosion

Dissertation

zur Erlangung des Grades des Doktors der Ingenieurwissenschaften
der Naturwissenschaftlich-Technischen Fakultät III
Chemie, Pharmazie, Bio- und Werkstoffwissenschaften
der Universität des Saarlandes

von

Marina Inés Cornejo

Saarbrücken / Leipzig
2011

Tag des Kolloquims: 29.07.2011

Dekan: Prof. Dr. Wilhelm F. Maier

Berichterstatter: Prof. Dr.-Ing. Frank Mücklich

    Prof. Dr. Dr. h.c. Bernd Rauschenbach

Vorsitz: Prof. Dr. David Scheschkewitz

Akad. Mitarbeiter: Dr.-Ing. Frank Aubertin

Abstract

Self-organization by low-energy ion beam erosion provides an alternative route for the fabrication of nanostructures on different materials in only one step. This study focuses on the experimental analysis of erosion of Si surfaces using a broad-beam ion source, exploring the underlying mechanisms of pattern formation. The correlation of the topography evolution with different erosion parameters was studied; namely, ion beam incidence angle, ion energy, fluence, as well as other specific parameters of the broad-beam ion source were analyzed.

At near normal incidence nanopatterns were formed only when Fe atoms were simultaneously incorporated during ion erosion, otherwise, the surface remained smooth. For the given experimental setup, the Fe flux can be regulated by the ion beam parameters. Among the nanopatterns formed, ripples with wavelength ~ 40 nm – 70 nm and amplitude up to ~ 10 nm are of special interest due to their high regularity. Although the physical mechanisms behind the topography evolution are not completely understood, a complex interplay between Fe incorporation, curvature dependent sputtering and different relaxation mechanisms seems to be responsible for the pattern formation.

At higher incidence angles, on the other hand, it is evident that angle dependent sputtering dominates the topography evolution and larger structures evolved.

It is shown that the topography can be tuned, up to certain degree, choosing the appropriate parameters.

Kurzfassung

Selbstorganisationprozesse bei der niederenergetischen Ionenstrahlerosion sind ein interessanter alternativer Ansatz für die Herstellung von Nanostrukturen mit geringem technologischen Aufwand. Der Schwerpunkt dieser Arbeit lag auf dem experimentellen Verständnis der Musterbildung auf Si-Oberflächen bei der Erosion unter Verwendung von Breitstrahlionenquellen. Iinsbesondere wurde die Korrelation zwischen den entstehenden Oberflächentopographien und den verschiedenen relevanten Erosions-parametern (z. B. Einfallswinkel der Ionen, Ionenenergie, Fluenz) analysiert.

Für kleine Einfallswinkel (zur Oberflächennormalen) können nur mit simultanem Einbau von Eisen Muster entstehen, andernfalls bleiben die Oberflächen glatt. Der Fe-Fluss wird durch verschiedene Quellenparamter kontrolliert. Bei den entstehenden Mustern sind vor allem hoch-geordnete Ripple-Strukturen mit Perioden zwischen 40 und 70 nm und Amplituden von ca. 10 nm von speziellem Interesse. Obwohl noch nicht endgültig aufgeklärt, geht man davon aus, dass die Musterbildung durch das komplexe Wechselspiel zwischen Eiseneinbau, dem krümmungsabhängigen Zerstäubungsprozess sowie verschiedenen Relaxationsprozessen verursacht wird.

Für größere Ioneneinfallswinkel konnte gezeigt werden, dass der Mechanismus des gradienten-abhängigen Zerstäubens die Entwicklung der Oberflächentopographie massgeblich bestimmt.

Insgesamt ist es möglich, dass durch die geeignete Parameterwahl ein Vielzahl von Oberflächentopographien zu realisieren.

Acknowledgements

This work could not have been accomplished without the collaboration of many people.

In first place, I would like to thank Prof. Dr. Dr. h.c. Bernd Rauschenbach, director of the Leibniz-Institute of Surface Modification (IOM), for giving me the chance to carry out this work and for his continuous support.

I am sincerely thankful also to Prof. Dr. Frank Mücklich, head of the Chair of Functional Materials, Department of Materials Science and Engineering, at the Saarland University. He kindly accepted the duty of supervising this thesis. I thank him for that and for the very helpful discussions and his friendly advice.

I would like also to express my gratitude to Dr. Frank Frost for his patient guidance throughout the different phases of this study. He is not only an excellent scientist but also a great person. I am glad to have had the chance to have been part of his research group during these years.

To the other members of the group, Dr. Bashkim Ziberi (at the present at the Faculty of Mathematical and Natural Science at the State University of Tetova, Macedonia) and Jens Völlner, with whom I shared the daily work, I am also very grateful. I thank them for the continuous assistance, the friendly and helpful discussions and for making me feel I could always count on them.

Many people at IOM collaborated on this work. In particular, I would like to acknowledge Dietmar Hirsch (SEM and SIMS measurements), Prof. Dr. Thomas Höche (at the present at the Fraunhofer Institute for Mechanics of Materials, IWM, for the HRTEM and EELS measurements), Dr. Jürgen W. Gerlach (RBS measurements), Christoph Meinecke (RBS), Dr. Joachim Zajadacz (FIB). I also would like to thank Horst Neumann, Dr. Dieter Flamm and Frank Scholze for their help with the ion beam equipment. I warmly thank Dr. Darina Manova for her constructive comments and suggestions on a preliminary version of this thesis. I am also grateful to her for her friendly support during these last years. Eva Salamatin, Dr. Klaus Zimmer, Ingrid Herold, Agnes Mill, Andreas Nickel and Thomas Freyer have also invested some of their time helping me with my work and I am greatly thankful to them.

I would like to express my gratitude to all the people working at the Administration and the Physical Department at IOM, as all of them helped me in one or other way. I am very grateful to them for their help and for creating a nice friendly working environment.

TABLE OF CONTENTS

Chapter 1

Introduction

The bombardment of solid surfaces with energetic ions is used in a large number of techniques, for instance in ion cleaning, ion etching, and film deposition. It is also used in many surface analysis methods, either to perform depth profiling, e.g. in combination with Auger Electron Spectroscopy (AES) or X-ray Photoelectron Spectroscopy (XPS), or to generate particles to be analyzed, e.g. Secondary Ion Mass Spectroscopy (SIMS). In many cases, the surface topography and roughness are affected, which may be a drawback when ion erosion is used, for example, as shaping or finishing technique. However, in other applications this effect can be exploited, e.g. to change the chemical, biological, or optical response of a surface.

An additional use of ion erosion is the fabrication of periodic structures that evolve by self-organization. This phenomenon was first reported in 1962 by Navez [1], who observed the formation of periodic patterns on glass due to the bombardment with low-energy ions. Since that time, the ion-induced pattern formation has been intensively studied. It represents an alternative route for the fabrication of nanostructured materials. It has been shown that different types of patterns in the nanometer scale can be generated in a wide variety of materials, e.g. elemental and compound semiconductors [2-8], single and polycrystalline metals [9-15], oxides [16-19]. By the use of broad-beam sources, large surface areas can be patterned in only one step.

However, although the ion-induced patterning has been studied for about fifty years, a complete understanding of the phenomenon has not been achieved yet.

There are many parameters involved in the pattern formation. This, on the one hand, indicates that there are many degrees of freedom for the tuning of the patterns but, on the other hand, makes the study of the technique very complex. Some of the parameters that determine the topography evolution under ion erosion are the substrate material, ion species, ion energy, substrate temperature, fluence, ion flux, ion incidence angle. Additionally, it has been recently shown that the intentional or unintentional incorporation of metallic atoms plays an important role in the pattern formation [20-25]. The physical mechanisms behind pattern formation are not completely understood. It is known that many atomic processes are activated by the collision of the energetic ions

with the substrate surface. Several theoretical models have been developed to explain the evolution of the topography under ion erosion. According to most of them, the pattern formation is the result of the interplay of curvature dependent sputtering and different relaxation mechanisms. No model takes into account the incorporation of metals.

The focus of this study is set on the erosion of silicon surfaces with Kr^+ with energies up to 2000 eV using a Kaufman-type broad-beam ion source. The objective of this work is the experimental analysis of the role of the erosion conditions, in order to enable a better tuning of the nanostructures and explore the underlying mechanism of the pattern formation. Additionally to several typical experimental parameters that are known to affect the topography evolution, i.e. ion energy, ion incidence angle, and fluence, here some characteristic parameters of the Kaufman-type ion source are examined. Besides, the simultaneous incorporation of metals, in particular Fe, is investigated.

This work is organized as follows: chapter 2 focuses on the state of art of the technique, with a short summary of the main experimental results reported in the last decades about the role of erosion conditions in the pattern formation. Next, the interactions between the incident ions and the substrate are briefly described and the main theoretical approaches of the ion-induced pattern formation are summarized.

In chapter 3, the ion erosion facility used for this study is presented. The main parameters that determine the ion beam properties are discussed. Besides, the techniques utilized for the characterization of the silicon surfaces after ion erosion are addressed.

Chapter 4 contains experimental observations on the influence of several parameters on the pattern formation. First, a short overview of the effect of the ion beam incidence angle is given. For the sake of clarity, the results concerning erosion at low and high incidence angles are presented separately. The role of different erosion parameters is studied; namely, ion beam incidence angle, fluence, ion energy, and some ion source parameters are investigated.

In chapter 5 the simultaneous incorporation of Fe during ion erosion is analyzed. The co-sputtering of Fe is an inherent feature of the ion erosion facility used and the Fe flux can be controlled by some erosion parameters. The correlation of the ion source parameters, Fe concentration on the silicon samples after erosion, and the resulting topography is determined.

In chapter 6 the results presented in the two previous chapters are discussed to establish the connection between the experimental conditions, pattern formation, and underlying processes.

In chapter 7 a short summary and outlook are given.

Chapter 2

Self-organization by ion beam erosion

Self-organization by ion beam erosion has been intensively studied since it was discovered [1]. Thanks to the numerous experimental and theoretical studies, certain understanding of the processes involved and control over the topography evolution has been achieved. However, there are still many unsolved issues that require further study.

The diversity of nanostructures that can be formed in only one step in a wide variety of materials (e.g. elemental and compound semiconductors [2-8], single and polycrystalline metals [9-15], oxides [16-19]) makes this technique an attractive alternative route for the production of nanopatterned surfaces.

There is a wide variety of nanostructures that can be fabricated by ion-induced self-organization. Some of the different topographies formed on Si and Ge under different experimental conditions are shown in Fig. 2.1. The AFM images give a first impression of the variety of topographies that can result from ion erosion on Si and Ge. They were formed under different experimental conditions: ion energy between 300 eV and 2000 eV, ion beam incidence angles (angle formed between the axis of the beam and the surface normal) from 0° to 75°, using different ion species (Ar^+, Kr^+, Xe^+). Some of them were obtained with simultaneous rotation of the substrate with respect to its surface normal during irradiation. Two interesting types of patterns are dots and wave-like features (here called ripples), which can be quite regular.

In this chapter, on rather a descriptive level, the possibilities offered by the self-organization by ion beam erosion and the state of knowledge about the processes involved will be presented. In section 2.1 a short review about experimental observations will be given, setting the focus on the ion erosion of silicon. It will be shown that a certain control of the topography evolution can be achieved by choosing the appropriate experimental conditions. Next, in section 2.2, the interaction of the incident ions with the solid substrate will be discussed and in section 2.3 the physical mechanisms that are thought to be responsible for the topography evolution and the main theoretical approaches will be briefly described.
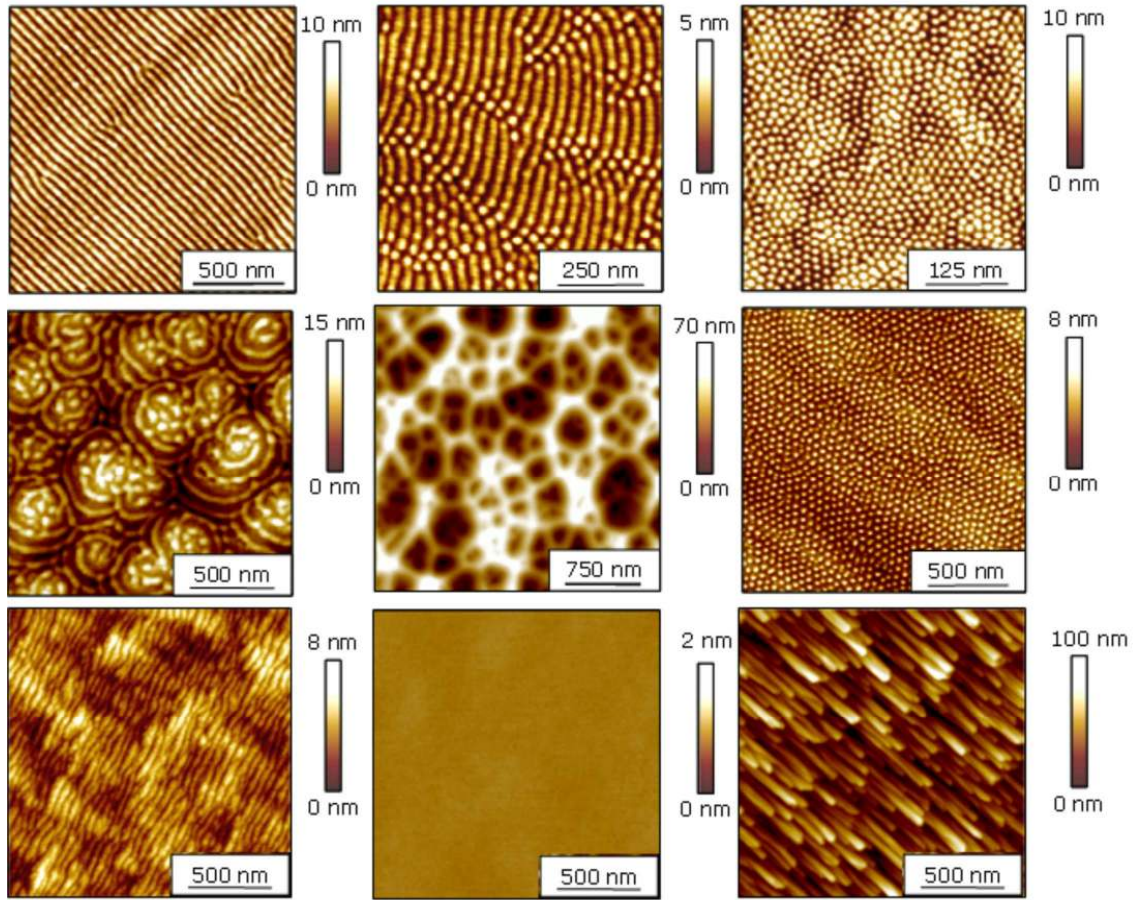
Figure 2.1. AFM images of different topographies produced on Si and Ge surfaces by low-energy ion beam erosion under different experimental conditions.

2.1. Experimental observations review

The formation of relatively regular structures induced by ion erosion was first reported in 1962. Navez observed that wave-like structures (ripples) evolved on glass surfaces due to the irradiation with air ions [1]. Since then, this phenomenon has been intensively studied in order to understand the processes involved and to be able to control the topography evolution.

The ion-induced nanostructures have been produced on single-crystalline semiconductors (Si, Ge, compound semiconductors) [2-6, 8, 26-28], single-crystalline metals (Cu, Ag) [9, 12, 14, 15], polycrystalline metals (Ag, Au, Pt) [10, 11, 13] and amorphous materials (SiO_2) [16-19].

The resulting topography is highly affected by the experimental conditions: angle of incidence of the ions, fluence, substrate temperature, ion energy, flux, etc. The sample manipulation during the irradiation also influences the topography evolution; i.e.

simultaneous sample rotation. Latest studies reported also growing evidence of the importance of co-deposition of metals during the irradiation of Si and Ge surfaces.

The many operational parameters that determine the topography evolution indicate that there are many degrees of freedom for tailoring the surface topography but they also make the understanding of the phenomenon a challenge.

2.1.1. General experimental conditions

For the self-organized patterning by ion beam erosion ions from inert gases are usually used. The differences in the self-organized nanostructures formed on Si and Ge using Ar^+, Kr^+ and Xe^+ are in some cases not significant and not easily correlated with the difference in atomic number and atomic weight of the ions. However, there is a limitation with respect to the relation of the ion and substrate masses. No structure seems to evolve when the incident ions are lighter than the substrate atoms. This seems to be the reason why the pattern formation on Ge surfaces is not achieved using Ar and Ne is not appropriate for the patterning of Si [29]. The explanation for this effect may be related with the distribution of the deposited energy. Using heavier ions, the energy distribution is concentrated closer to the surface and, in consequence, more recoils are produced. Another reason could be related to the fact that for decreasing ion mass the ejected atoms from the substrate and backscattered projectile ions become more important and both contribute to the preferential erosion of peaks compared with valleys, thus leading to additional smoothening.

According to the published studies, focused and unfocused ion beams can be used with varying diameters. The use of broad beam sources (ion beam diameter from 3 cm to 20 cm or larger) represents an advantage for potential industrial applications.

Nevertheless that mostly low energies (up to 2000 eV) are used [2-4, 16, 26, 28, 30-34], the self-organization has also been observed at higher energies (4 keV - 50 keV) [1, 5, 35, 36].

2.1.2. Effect of operational parameters on topography evolution on silicon

Due to its technological importance and the simplicity provided as a one-component material, Si has been intensively studied. The different topographies formed by the ion-induced self-organization processes on Si and their dependence on the experimental parameters have been investigated in the last decades. Another reason to study Si is that

after several minutes of irradiation, even at low ion energies, a surface layer of the crystalline material amorphisizes eliminating the effects that could be related to the crystalline structure of the material. This is valid, in general, for semiconductor materials at temperatures up to some hundreds degree Celsius. Next, the effect of some experimental parameters on the pattern formation on Si will be presented.

2.1.2.1. Ion beam incidence angle

It is known since the self-organization by ion beam erosion was first observed, that the incidence angle of the ions plays an important role on the topography evolution [1, 5, 37]. The incidence angle α considered here is the angle formed between the ion beam direction and the surface normal. Navez [1] observed in 1962 that the direction of the ripples was dependent on the incidence angle. For ion beam incidence close to grazing angles ripples parallel to the ion beam projection on the surface (wave vector perpendicular to the beam) evolved and at lower angles, ripples oriented perpendicular to the beam direction (wave vector parallel to the ion beam) were observed. Carter et al. [5] reported in 1977 the formation of perpendicular-mode ripples at $\alpha = 45°$ and parallel columnar structures at $\alpha = 75°$ on Si by bombardment with 40 keV Ar$^+$.

This change in the structure orientation was successfully predicted by Bradley and Harper model (BH) [37]. This model was the first one that explained the formation of ripples by ion erosion and it will be described in subsection 2.3. The BH model predicts that when the incidence angle is below the *critical angle*, which is in general ~ 70°-75°, ripples perpendicular to the ion beam projection on the surface evolve. The critical angle depends on the material, ion species and ion energy. At incidence angles larger than this critical angle, features parallel to the ion beam projection on the surface are formed.

Many experimental observations are in agreement with the predictions of the BH model about the orientation of the features. However, the number of studies about the topic increased rapidly with the time and numerous dissimilar experimental observations on the effect of the incidence angle were reported.

For example, Ziberi et al. [31, 38, 39] observed the formation of perpendicular mode ripples on Si at near normal incidence, in agreement with the BH model. However, they also found the formation of dots at an incidence angle near 30° and that smooth surfaces were stable under ion erosion at incidence angles between ~ 35° - 60° for ion energy up

to 2000 eV. The stability of smooth surfaces and the formation of dots at near normal incidence were not contemplated by the first models.

Madi et al. [40] observed the smoothening of the Si surface during the irradiation with 1000 eV Ar$^+$ at $\alpha = 10°$ instead of ripple formation. According to Zhang et al. [36], no pattern evolves on Si bombarded with Xe$^+$ at $\alpha = 30°$ with different ion energy (from 1000 eV to 50 keV). The formation of perpendicular-mode ripples on Si at $\alpha = 30°$ was observed by Habenicht et al. [41] but under very different conditions; they produced ripples using focused ion beam, 30 keV Ga$^+$. The ripples formed by erosion with noble gas ions at near normal incidence have been reported on Si and Ge only by Ziberi et al. [29, 31, 32, 38] and on Ge by Carbone et al. [28].

There are also disparities in the observations for bombardment of Si with Ar$^+$ at normal incidence. The formation of holes without regular distribution was observed on Si(001) sputtered with 500 eV Ar$^+$ at normal incidence by Ziberi et al. [38]. These observations are consistent with the report from Madi et al. [42], who presented the formation of holes with $E_{ion} < 600$ eV. However, while Ozaydin et al. [43] observed no pattern evolution by bombardment of Si(001) with Ar$^+$ $E_{ion} = 1000$ eV, under the same experimental conditions Gago et al. [44] reported the formation of nanodots. The formation of dots was also observed with $E_{ion} = 1200$ eV [2]. These are only some examples that show the disagreement on the experimental results reported.

Reports about the high incidence angle region do not show so numerous contradictory experimental observations. Perpendicular-mode ripples are formed at incidence angles near 60° and 65°. They have similar dimensions as the perpendicular-mode ripples formed at near normal incidence; their amplitude can reach ~ 10 nm and their wavelength ranges between ~ 30 nm and 70 nm. At incidence angles higher than ~ 70°, parallel-mode waves or columnar structures with relatively high amplitude evolve. There are many reports about the ripples and columnar structures on Si obtained at incidence angles in the range ~ 60° to 80° [3, 4, 26, 36, 45, 46].

2.1.2.2. Substrate rotation

As it was mentioned in the previous subsection, the orientation of the nanostructures formed is determined by the direction of the ion beam. If the sample is rotated around its surface normal during irradiation, the anisotropy given by the beam direction is eliminated. It is observed that under certain conditions, the rotation during ion

bombardment suppresses pattern formation, enhancing smoothening of surfaces [47]. Nevertheless, in many cases the rotation does not suppress roughening; it only decreases its rate. It has been found that domains of hexagonally ordered dots formed on Si irradiated at high ion incidence angles (e.g. $\alpha = 75°$) with simultaneous sample rotation [38, 48, 49]. Due to the rotation, the hexagonally ordered domains present a random azimuthal distribution. These dots may have a lateral size (deduced from the distance between neighbors) between 30 nm and 50 nm and a relatively narrow size distribution when large fluences are reached.

As it was mentioned in the previous subsection, dots can be also formed on Si surfaces without rotation of the sample at normal incidence [2] or at α near 30° choosing the appropriate operational parameters [32, 50]. However, these dots formed without simultaneous rotation present larger size distribution even after long erosion times, they have, in general, lower amplitudes and they are not ordered in domains.

2.1.2.3. Fluence

According to most experimental studies, the amplitude of perpendicular-mode ripples and dots (formed with or without sample rotation) on Si increases with the time up to saturation [4, 31, 38, 51]. The amplitude saturation was also observed on other materials (Ge, compounds semiconductors, Cu) and it may be related to the nonlinear effects that become effective after a certain erosion time. As the nonlinear effects are not contemplated in BH model, this model does not predict saturation.

The wavelength of the features on silicon is, in general, not affected by the fluence at room temperature [29, 38]. However, at high temperatures coarsening was observed for parallel- and perpendicular-mode ripples on Si at temperatures between 873 K to 1023 K ($E_{ion} = 250$ eV – 1200 eV, $\alpha = 60°$) [4]. An increase of the characteristic length scale with the fluence was also found at temperatures higher than 673 K on Si(001) with 1000 eV Ar$^+$ normal incidence irradiation [43].

It was observed as well that the ordering of the some features at room temperature increases with the fluence [29, 38]. Additionally, as it was already mentioned, the size distribution of the dots formed at $\alpha = 75°$ with rotation of the sample becomes narrower with the erosion time [38].

2.1.2.4. Ion energy

The influence of the ion energy (E_{ion}) also depends on the substrate temperature. It was shown that at room temperature and using low energies the amplitude and the wavelength or period of the ripples formed at near normal incidence increased with E_{ion}; the wavelength could be tuned from ~ 35 nm to 75 nm varying E_{ion} from 500 eV to 2000 eV [31]. The lateral size of the dots formed at $\alpha = 75°$ at room temperature with simultaneous sample rotation was also observed to vary with E_{ion}, e.g. the lateral size of dots formed by Kr$^+$ irradiation varied from 25 nm to 50 nm when E_{ion} increased from 300 eV to 2000 eV [52].

Although the effect of E_{ion} should be further investigated, this dependence of the lateral size of the ripples and dots on E_{ion} may represent an interesting tool for the control of the size of the features. It was observed, in general, that at room temperature, the wavelength of the ripples formed at α between 60° and 65° also increased with increasing E_{ion}. For example, it was reported that the wavelength of the ripples was ~ 50 nm for $E_{ion} = 2000$ eV [53] and ~ 1000 nm for $E_{ion} = 100$ keV [54].

On the other hand, at high substrate temperatures (~ 973 K), Brown and Erlebacher [4] observed that when E_{ion} increased from 250 eV to 1200 eV (Ar$^+$), there was a significant decrease in the ripples amplitude and wavelength on Si(111) at $\alpha = 60°$. The observations from Brown and Erlebacher are in accordance with BH model, where the only relaxation mechanism considered is the thermally activated diffusion. Using higher ion energy ($E_{ion} = 60$ keV $-$ 100 keV), Hazra et al. [54] found that with the increase of E_{ion} the amplitude of the ripples formed on Si(001) at $\alpha = 60°$ decreased while the wavelength increased.

At low temperatures the surface is amorphized due to ion erosion, while at high temperature the substrate surface remains crystalline. The amorphization begins when the fluence reaches the amorphization threshold, then the thickness of the amorphous layer increases and saturates after a short time. Together with the incidence angle, E_{ion} has a strong influence in the amorphous layer thickness; according to reported studies, with $E_{ion} = 2000$ eV the layer is some nanometers deep ($\sim 3 - 8$ nm) [38] and with 120 keV it can reach a depth larger than 250 nm [46]. Due to the amorphization of the surface layer, no significant differences have been found in the topography evolution at low temperatures in the different crystal orientations. In chapter 4, it will be shown that

even at room temperature the effect of ion energy on the pattern formation is more complex as it was observed so far.

2.1.2.5. Substrate temperature

The influence of the substrate temperature in the pattern formation has been also studied. Again, a comparison of the experimental observations reported is not simple due to the many experimental parameters involved. As an example, the observations from Erlebacher et al. [26] could be mentioned. In agreement with the BH model, which predicts that the ripples wavelength increases with temperature, they observed that increasing the temperature from 733 K and 873 K the ripples wavelength increased on Si(001) bombarded with 750 eV Ar^+ at $\alpha = 67.5°$. Gago et al. [44], on the other hand, who studied the influence of the temperature in the dot formation on Si(001) by bombardment with 1000 eV Ar^+ at normal incidence, found that the pattern was not affected by the substrate temperature up to 425 K; between 425 K and 525 K the dot height and wavelength decreased with the temperature and finally above 550 K no pattern evolved.

Most experimental observations agree that in the case of Si, the temperature shows no influence when the substrate temperature is low. At low temperatures the Si surface is amorphized by the ion bombardment while at high temperature it remains crystalline. The transition from one case to the other depends on the sputter conditions. For the bombardment of Si(001) with 1000 eV Ar^+, the transition was observed between 673 K and 773 K [43].

2.1.2.6. Simultaneous metal incorporation

Until some years ago, in most studies about the self-organization by ion erosion, the ion bombardment was considered free of contamination. However, the incorporation of foreign atoms during bombardment with noble gas ions is, under certain experimental conditions, difficult to avoid, in particular when broad-beam sources are used. The incorporated atoms may affect the topography evolution.

The structuring by ion beam erosion in the presence of impurities has been first observed several decades ago [55]. Cones or pyramids on the micron size were formed by ion bombardment with a concurrent supply of a seed material [55-59]. Although the structures presented in this study are much smaller, it has been suggested that the

inadvertent incorporation of impurities may also play an important role in their formation.

Ozaydin et al. investigated the relevance of the incorporation of Mo [22, 23, 60, 61] during the ion erosion of Si surfaces at normal incidence. As they fixed the Si samples using Mo clips, they observed that after bombardment with 300 eV Ar$^+$ at normal incidence, dots on the major part of sample surface and ripple-like structures near the Mo clips were formed [60].

The role of the simultaneous metal incorporation was also studied by Sánchez-García et al [24, 25]. They showed that the irradiation at normal incidence with simultaneous metal incorporation (Fe and Mo) led to the formation of nanoholes or nanodots on Si surfaces. They observed that the topography could be changed from nanoholes to nanodots by increasing the ion current density or increasing the fluence at low ion current density. They correlated this change from holes to dots with a decrease of the metal content on the substrate surface.

Hofsäss and Zhang studied the ion erosion with simultaneous co-sputtering, which they called *surfactant sputtering*. They combined different substrates and surfactants and proposed a simple model to explain steady state coverage of a substrate with surfactant atoms. The experimental observations and the model can be found in [62, 63].

Macko et al. [21] observed that due to the irradiation with Kr$^+$, $E_{ion} = 2000$ eV, at $\alpha \leq 45°$ no pattern evolved on pure Si surfaces, while with the co-sputtering of a stainless steel target, ripples and dots were formed.

It is necessary further investigation about the incorporation of metals during erosion in order to understand its effect in the pattern formation.

2.1.3. Other materials

The ion beam erosion as a patterning technique can be applied to a wide variety of materials beside Si. Here some examples will be given.

2.1.3.1. Germanium

Germanium is also an important semiconductor with many uses in electronics. So far, there are only few reports about the pattern formation by low-energy ion beam erosion on Ge surfaces [6, 28, 39, 64]. Ziberi et al. [39, 52] reported the formation of dots and ripples at $\alpha = 0°$ and $\alpha = 5°$, respectively, at room temperature after irradiation of

Ge(001) with 2000 eV Xe[+]. Increasing the ion beam incidence angle, dots were formed on the surface together with ripples ($\alpha = 10°$) and at $\alpha > 30°$, the surface remained smooth. Also Carbone et al. [28] observed the simultaneous presence of ripples and dots after the irradiation of Ge(001) with 1000 eV Xe[+] at $\alpha = 10°$. As in the case of other semiconductor materials, Ge is amorphized due to the ion erosion at room temperature and at high temperatures it remains crystalline. Chason et al. [6] studied the irradiation of Ge(001) with 1000 eV Xe[+] at $\alpha = 55°$ and observed that at 423 K the surface amorphized and the roughness reached a steady state value without ordered structure formation. At 523 K and 573 K, the surface remained crystalline, and ripples perpendicular to the ion beam projection on the surface were formed.

2.1.3.2. III/V semiconductors

The ion induced self-organization on III/V semiconductors has been also investigated. The studies have shown that in many cases there is a preferential sputtering, due to the different sputtering yields of the components, which leads to the enrichment of the surface with one component. Thus, the ion erosion of InP and GaAs results in an enrichment of In and Ga, respectively [65, 66]. The preferential sputtering makes the understanding of the processes involved even more difficult than for elementary materials. With respect to the nanostructures formed by ion erosion, one interesting example is the nanodots on GaSb formed at normal incidence by low energy Ar^{+} erosion. Facsko et al. [7] produced nanodots on GaSb with hexagonal ordering by bombardment with 420 eV Ar^{+} at normal incidence. They studied the effect of the fluence and they observed that in the fluence range of 4×10^{17} cm^{-2} to 4×10^{18} cm^{-2}, the period of the dots increased from 18 nm to 50 nm. They observed also that the ordering increased and then the features stabilized. They showed that the dots (or cones) kept the crystalline structure of the bulk GaSb and they were covered by a 2 nm amorphous layer. In a related study Facsko et al. [27] found that the wavelength of the nanodots on GaSb produced at normal incidence increased with E_{ion} (proportional to the square root of the ion energy) over a large range of energies.

The formation of nanodots organized in hexagonally ordered domains on InP and GaSb after Ar^{+} bombardment but under oblique ion incidence with simultaneous sample rotation were reported by Frost et al [8]. They showed that due to the bombardment at room temperature with Ar^{+}, $E_{ion} = 500$ eV, $\alpha = 40°$ dots with a lateral size of ~ 85 nm

were formed. The effect of the ion beam incidence angle under these sputter conditions was investigated. Domains of hexagonally arranged dots were formed at $\alpha \leq 50°$; with further increase of the ion beam incidence angle the periodic pattern vanished and at $\alpha = 80°$ dot formation was again observed but with smaller dot size than for $\alpha \leq 50°$. The height and wavelength of the dots at $\alpha = 40°$ increased with increasing E_{ion} (energy ranged from 350 eV to 1200 eV). The sample temperature seems to be critical for InP under these conditions. In the range of 285 K to 375 K, the wavelength and roughness increased with temperature. The dots had the same crystalline structure as the InP bulk material, only covered by a thin amorphous layer. As mentioned above, due to preferential sputtering effects the amorphous layer showed an enrichment in In. More details about the formation of dots on InP and GaSb can be found in [8, 34]. Self-organized patterns can be also produced on InAs and InSb by ion beam erosion [67].

2.1.3.3. Insulators

Self-organization by ion erosion can also occur on isolators. Among them, SiO_2 is the most studied material. Flamm et al. [17] studied the irradiation with 800 eV Ar^+ at different incidence angles. They observed that at $\alpha < 40°$ no regular pattern evolved and that the roughness of the surface was slightly increased. At $\alpha \sim 40° - 70°$ perpendicular-mode ripples formed and at $\alpha \sim 80°$ the orientation of the features was rotated by 90°.

In agreement to these results, Mayer et al. [18] observed the formation of ripples oriented perpendicular to the ion beam direction after 1000 eV Xe^+ bombardment at $\alpha = 55°$. Perpendicular-mode ripple formation on SiO_2 was also observed after bombardment with 1000 eV Ar^+ at $\alpha = 45°$ [19].

Toma et al. [16] studied the pattern formation on glass due to bombardment with 800 eV Ar^+ and found that perpendicular- and parallel-mode ripples were formed at $\alpha = 35°$ and 75°, respectively.

The temporal evolution of the ripples was studied and the increase of ripples wavelength and amplitude with the fluence was observed [16-18]. It was found that the size of the ripples (wavelength and amplitude) increased with increasing E_{ion} [17-19]. On the contrary, no correlation between the wavelength and the ion flux was observed [17]. The effect of the temperature in the ripples wavelength was found to be negligible

when $T < 473$ K while an Arrhenius-like increase of the wavelength at higher T was observed [19].

2.1.3.4. Metals

The response of crystalline metals to the ion bombardment differs from that of semiconductors and amorphous materials. The difference in the behavior is mainly due to the higher diffusivity in metals and the non-directional character of the metallic bonds. Generally, the ion bombardment of metals does not imply amorphization. Thus, the behavior can not be explained by Bradley and Harper model. In crystalline metals an additional destabilizing mechanism that may represent a patterning driving force has to be considered, i.e. the effect of the Ehrlich-Schwoebel (ES) energy barriers. The ES barriers oppose the diffusion toward downhill direction. Depending on the experimental conditions the nanostructure orientation on monocrystalline metals can be given by the crystallographic orientation (when diffusive regime dominates) or the direction of the ion beam (at grazing incidence angles and low substrate temperature to enhance the erosion regime). Mounds, parallel- and perpendicular-mode ripples can be produced. On polycrystalline metals the grain boundaries do not hinder the formation of coherent ripple patterns if the erosive regime dominates. Numerous examples and a complete description of the ion-beam erosion on metals can be found in [11, 12, 68-71].

2.2. Ion-target interaction

When a solid surface is bombarded with energetic ions, many processes are initiated due to the collision of the incident ions with the nuclei and electrons of the material atoms [72, 73]. The projectiles transfer some or all their energy and momentum to the substrate atoms, ionizing them, displacing them from their places, exciting their electrons or even generating their ejection from the solid (sputtering). Additionally, electrons and photons may be emitted. A fraction of the incident ions is backscattered due to collisions with nuclei from surface and near-surface atoms.

The ions that penetrate the solid surface are decelerated and their trajectory is deflected (scattering) due to the collisions. They pass through the material until eventually they lose all their energy and come to a stop. The atoms that are removed from their original sites are subsequently slowed down in the solid by the same mechanisms as the incident ions. They may also remove other atoms from their lattice sites (recoil atoms). Thus, a

collision cascade develops. There are three regimes [72] depending on the type of displacement cascade: near-threshold, where the energy transferred is only sufficient to produce some isolated recoils, linear-cascade, where a limited fraction of substrate atoms are set in motion and are involved in the collision cascade, and spike or non-linear cascade valid for bombardment with high-energy, heavy ions or molecular ions; here the density of recoil atoms is high and moving atoms collision becomes frequent and the linearity assumption breaks down.

The linear-cascade is the regime that applies to the present work. In general, it is convenient to treat the interaction between two particles at a time; the collisions are approximated to sequence of binary collisions, i.e. sequence of independent collisions between a moving particle and a still atom. If the energy and momentum are conserved, the collision is termed elastic (nuclear stopping), and it is inelastic (electronic stopping) if there is a conversion between kinetic and potential energy. At the ion energies used in this study, nuclear stopping dominates. The elastic collisions result from repulsive Coulombic interactions between the incident ion nucleus and the substrate atom nucleus. The energies of the ions and substrate atoms after an elastic collision depend on the energy of the incident ions and the masses of the ions and substrate atoms.

The distance travelled by the ions, which is mainly determined by the ion energy and the mass matching, is called the ion range. The energy that they lose as they pass through the material is known as stopping power ($-\mathrm{d}E/\mathrm{d}x$). Since the energy loss involves collision with atoms (from the substrate) that are subject to statistical fluctuations, the stopping power and also the ion range are subjected to fluctuations. The stopping cross section is also important to describe the interaction of incident ions and solid matter and it is defined as $S(E) = -1/n \, \mathrm{d}E/\mathrm{d}x$, where n is the atomic density. Here, only the nuclear stopping cross section S_n will be considered. S_n gives the average energy dissipated during the collision processes. For low ion energies, where the screening of the Coulomb interaction is essential, the nuclear stopping cross section according to Sigmund [74] is given by:

$$S_n\left(E_{ion},T\right) = \int_0^{T_{max}} T d\sigma\left(E_{ion},T\right) \tag{2.1}$$

where E_{ion} is the initial ion energy, $d\sigma$ is the differential elastic cross section, T is the transferred energy, $T_{max} = \gamma E_{ion}$, with $\gamma = 4M_1M_2/(M_1+M_2)^2$; M_1 and M_2 are the masses

of the incoming ion and substrate atom, respectively. For low energies the cross section can be approximated by:

$$d\sigma(E_{ion},T) \cong C_m E_{ion}^{-m} T^{-1-m} dT \qquad (2.2)$$

with:

$$C_m = \frac{\pi}{2} \lambda_m a_s^2 \left(\frac{M_1}{M_2}\right)^m \left(\frac{2Z_1 Z_2 e^2}{a_s}\right)^{2m} \qquad (2.3)$$

where Z_1 and Z_2 are the atomic numbers of the incoming ion and substrate atom, respectively, a_s the screening length, m characterizes the power potential employed to describe the interatomic interaction between atoms; it varies slowly from $m = 1$ at high energies, down to $m \approx 0$ at very low energies. λ_m is a dimensionless function of the parameter m which increases over this range of m $\lambda_1 = 0.5$ to $\lambda_0 \approx 24$. The nuclear stopping cross-section is:

$$S_n(E_{ion},T) = \frac{1}{1-m} C_m \gamma^{1-m} E_{ion}^{1-2m} \qquad (2.4)$$

With respect to the ion range, because of ion scattering, the average path length $R(E)$ is simple to calculate but difficult to measured. In principle, it can be derived from the stopping cross sections [72]:

$$R(E) = \frac{1}{n} \int_0^E \frac{dE}{[S_n(E)]} \qquad (2.5)$$

The average projected range R_p (the projection of R on the direction of the ion beam) and the penetration depth are more readily accessible. R_p is smaller than the average path length by a factor which depends on the mean path, scattering angles, and, consequently, on the specific path of an individual ion.

Under certain conditions, the creation of defects due to ion bombardment can lead to the amorphization of crystalline materials. Ion energy, ion mass, ion flux and substrate temperature are the critical parameters controlling the amorphization process. The amorphization occurs when the fluence reaches the amorphization threshold; the thickness of the amorphous layer increases and then it saturates. The thickness of the saturated amorphous layer can range from a few nm to some tens of nm at low energies. The temperature of the substrate can determine whether the effects generated within the collision cascade are stable or whether they can migrate and annihilate. In the case of silicon, temperature lower than ~ 900 K produces relaxation of the amorphous structure,

while at higher temperatures these layers regrow by solid epitaxy on the underlying crystalline substrate [75].

The atoms of the surface or near surface that receive a momentum in the direction of the surface of the solid with enough energy to overcome the surface binding are emitted or sputtered. The removal of surface and near surface atoms by direct momentum transfer in a collision cascade is called physical sputtering. The sputtering yield (Y) is a characteristic parameter to describe sputtering, and it is defined as the ratio of the number of sputtered target atoms to the number of incident ions. The sputtering yield is determined by a number of factors, i.e. ion species, target material, ion energy, incidence angle. There is a critical value of ion energy below which no sputtering takes place. Above the critical value, as the incident ion energy increases, Y increases, reaches a maximum and then decreases as the energy is further increased. This is because the incident ions are implanted to a greater depth and displaced atoms cannot easily reach the surface. The incidence angle of the incident ions has a strong influence in the sputtering yield.

With respect to the incidence angle, some terms should be defined. For the description of the experiments, the ion beam incidence angle α is usually used, i.e. the angle between the ion beam with the macroscopic surface normal. However, if the substrate surface is not perfectly smooth, the ions will hit the substrate at different angles on the surface. Therefore, the local incidence angle θ is introduced to refer to the angle between the ion trajectory and the local surface normal. For amorphous, amorphizable and polycrystalline materials, it is observed that Y increases monotonically with θ, due to the increase of the deposited energy near the surface. It reaches a maximum at θ ~ 60° - 80° and decreases sharply as θ gets close to 90°, due to the higher proportion of ions that are reflected. The incidence angle, at which Y is maximal, will be called here θ_p.

If physical sputtering is the only process considered, the ion bombardment of a solid surface, which is stochastic in nature, will produce the increase of surface roughness with the fluence. Additionally, Sigmund [76, 77] showed that local variations in the sputter rate may occur on the solid surface when features are present on the surface. The features dimensions should be similar to the size of the zones where the ions deposit their energy. In his theory about sputtering of amorphous materials, Sigmund [76, 77] proposed that the sputtering yield was proportional to the deposited energy in elastic
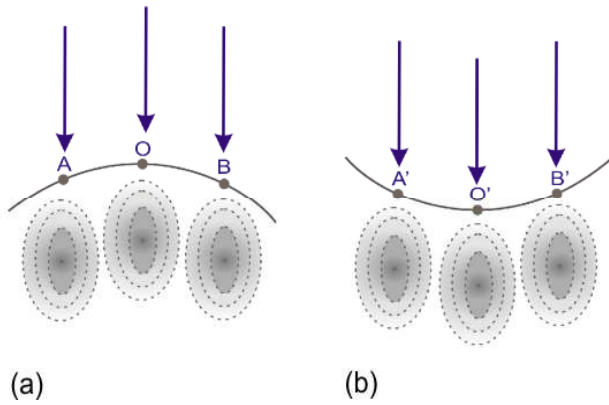
Figure 2.2. Schematic representation of ions colliding at a crest (a) and a trough or valley (b). The arrows indicate the direction of the ions. The dotted lines represent contours of equal energy deposition for ions striking at the positions *A, O, B, A', B'* and *O'*.

collision in the surface $F_D(E, \theta, x = 0)$ where E is the total energy deposited, θ the local ion incidence angle, and x the depth of the energy deposition. The sputter yield is given by:

$$Y(E,\theta) = \Lambda F_D(E,\theta,0) \tag{2.6}$$

where Λ is a material-dependent constant.

Sigmund approximated the deposited energy profile by a Gaussian. The average energy deposited at a point $r(x, y, z)$ in the target by an ion travelling along the z axis is given by:

$$F_D(r) = \frac{E}{(2\pi)^{3/2}\sigma\mu^2} \times exp\left[-\frac{[z-h_0+a]^2}{2\sigma^2} - \frac{x^2+y^2}{2\mu^2} \right] \tag{2.7}$$

Here, r represents a point (x, y, z) in the target, a the average depth of the deposited energy, σ and μ the widths of the distribution parallel and perpendicular to the beam direction, respectively, and h_0 the height at zero time.

This theory implies that the erosion rate at local minima in the surface profile is larger than at local maxima, which leads to an increment of the roughness [77]. In Fig. 2.2 the impingement of ions at a crest (Fig. 2.2 a) and a trough (Fig. 2.2 b) is represented.

The energy deposited at the point O by ions striking the surface at O is the same as the deposited energy at O' by ions striking the surface there. However, the energy deposited at O by ions hitting the surface at A is lower than that deposited at O' by ions hitting at A'. Similar situation can be considered for B and B'. Therefore, the rate of erosion at O' is greater than that at O. The curvature dependent sputtering leads to the increase of the amplitude of the features present on the initial surface or created by the stochastic fluctuation of the sputtering process.

2.3. Theoretical approaches for surface evolution under ion erosion

In the previous section the effects of the bombardment of solid surfaces with energetic ions were briefly discussed. However, taking these effects in consideration is not enough to explain the self-organization of nanostructures due to ion erosion. More complex mechanisms seem to be responsible for the morphological evolution of the surface. Typically, the surface of the substrate is far from equilibrium during the bombardment and many atomistic surface processes become effective.

There are many theoretical models that try to explain the resulting topography. Nevertheless, a complete understanding of the physical processes has not been achieved yet.

Some of the models are microscopic models, based on Monte Carlo and Molecular Dynamic simulation. The processes are analyzed at the atomic level. Some microscopic models have provided useful information about the physical mechanisms behind the structures formation [78-80].

However, in order to describe the spatial and temporal evolution of the surface topography continuum models are more appropriate. In continuum models, the topography is described as a continuous function and the atomic and crystalline structure is not considered. Differential partial equations are used to describe the spatial and temporal evolution. A brief discussion about the main continuum models will be presented in this section. The first model developed to explain the ripples formation by ion erosion was the model from Bradley and Harper.

2.3.1. Bradley and Harper model

In 1988 Bradley and Harper proposed the first model that explained the formation of ripples on amorphous materials under ion bombardment [37]. The model is based on Sigmund's theory [76, 77] and it is extended to continuum surface profiles. The linear continuum equation describing the surface topography evolution combines the curvature dependent sputtering with surface smoothing due to thermally activated surface diffusion:

$$\frac{\partial h}{\partial t} = -\upsilon_0(\theta) + \upsilon'_0(\theta)\frac{\partial h}{\partial x} + \frac{Ja}{n}Y_0(\theta)\left[\Gamma_x(\theta)\frac{\partial^2 h}{\partial x^2} + \Gamma_y(\theta)\frac{\partial^2 h}{\partial y^2}\right] - B\nabla^2\nabla^2 h \qquad (2.8)$$

The first term on the r.h.s. of Eq. 2.8 represents the erosion rate of the flat surface, the second one the lateral movement of the structures on the surface, the third term the

curvature dependent sputtering and the last term the surface diffusion. J represents the ion flux, a the mean depth of deposited energy, n the atomic density, B is the diffusion coefficient (in this case of the thermally activated diffusion), and Γ_x and Γ_y the coefficients that describe geometrical distribution of the deposited energy and they are expressed as:

$$\Gamma_x(\theta) = \frac{A}{B_1} \sin\theta - \frac{B_2}{2B_1}\left(1 + \frac{A^2}{2B_1}\right)\cos\theta - \frac{AC}{B_1^2}\left(3 + \frac{A^2}{B_1}\right)\cos\theta \qquad (2.9)$$

$$\Gamma_y(\theta) = -\frac{\mu^2}{a^2}\left(\frac{1}{2}B_2 + \frac{AC}{B_1}\right)\cos\theta \qquad (2.10)$$

where:

$$A = \left(\frac{a}{\sigma}\right)^2 \sin\theta \qquad (211)$$

$$B_1 = \left(\frac{a}{\sigma}\right)^2 \sin^2\theta + \left(\frac{a}{\mu}\right)^2 \cos^2\theta \qquad (2.12)$$

$$B_2 = \left(\frac{a}{\sigma}\right)^2 \cos\theta \qquad (2.13)$$

$$C = \frac{1}{2}\left[\left(\frac{a}{\mu}\right)^2 - \left(\frac{a}{\sigma}\right)^2\right]\sin\theta\cos\theta \qquad (2.14)$$

$$D = \frac{1}{8}\left[\left(\frac{a}{\mu}\right)^2 \sin^2\theta + \left(\frac{a}{\sigma}\right)^2 \cos^2\theta\right] \qquad (2.15)$$

The coefficients a, σ and μ are related to the Gaussian energy distribution and are defined as in Eq. 2.7. The orientation of the ripples is determined by the coefficient Γ_x or Γ_y with the minimum value. Using Eq. 2.9 – 2.15, the variation of Γ_x and Γ_y with the ion incidence angle θ for Si(001) irradiated with Kr$^+$ with 2000 eV was estimated and it is shown in Fig. 2.3. The energy distribution parameters used were $a = 4.9$ nm, $\sigma = 2.0$ nm, and $\mu = 1.0$ nm, calculated using SRIM 2008.04 [81, 82].

It is observed that Γ_x has a negative or positive value depending on the incidence angle, while Γ_y is always negative. At normal incidence, where $\Gamma_x = \Gamma_y$, no preferential orientation is observed; depressions or hills may evolve, probably as a result of the simultaneous formation of waves with different directions. At off-normal incidence and up to the *critical angle* θ_c, which in this case is $\sim 75°$, it is observed that $\Gamma_x < \Gamma_y$, thus the ripples are perpendicular to the ion beam projection on the surface. For larger
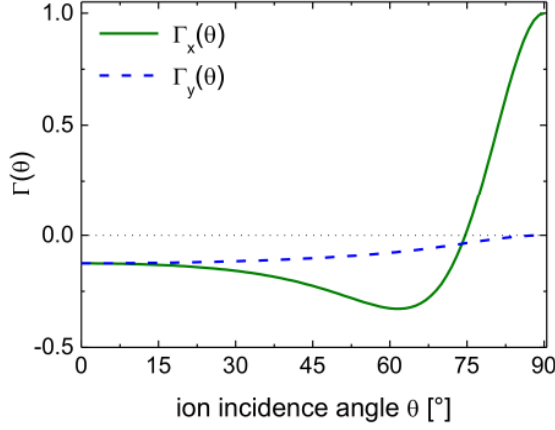
Figure 2.3. Variation of Γ_x and Γ_y with the ion incidence angle, calculated for Kr^+ irradiation of silicon with $E_{ion} = 2000$ eV.

incidence angles, where $\Gamma_x > \Gamma_y$, the ripples are parallel to the ion beam direction. There is no significant difference when these calculations are done for lower E_{ion} and for Ar^+ instead of Kr^+.

With respect to the dominant wavelength λ of the ripples, the model predicts:

$$\lambda(\theta) = 2\pi \left(\frac{2nB}{JaY_0(\theta)|\Gamma(\theta)|} \right)^{1/2} \qquad (2.16)$$

where $\Gamma(\theta) \equiv \min [\Gamma_x(\theta), \Gamma_y(\theta)]$. The other components of Eq. 2.16 were already defined for Eq. 2.8. From Eq. 2.3 and 2.4, the ion energy dependence of the ripples wavelength can be approximated to:

$$\lambda \sim \frac{1}{E_{ion}^{1/2}} \qquad (2.17)$$

It has to be mentioned here that in the BH model redeposition, shadowing and reflection are not taken into account. Thus, the model is valid only for small amplitude features and incidence angles smaller than that for which the sputter yield is maximal, θ_p.

BH model can, in general, successfully predict some experimental observations such as ripples orientation, and the exponential growth of the amplitude at short times. At long erosion times, however, the ripples amplitude saturates and this fact can not be explained by this model. The saturation has been attributed to the effect of the nonlinear processes that become effective at long times. Another implication of BH model is that the wavelength of the ripples should decrease for increasing E_{ion} (see Eq. 2.16 and 2.17) but as it was mentioned in section 2.1, at room temperature the opposite effect is observed. Furthermore, BH model implies that flat surfaces would remain flat due to the

23

absence of valleys and troughs. However, experimental observations show that under ion bombardment, in many cases, different types of structures evolve on initially flat surfaces.

In addition, the thermally activated diffusion does not seem to be the main relaxation mechanism at low substrate temperatures. Evidence of this is the fact that the surface does not smoothen after ceasing the ion bombardment and keeping the temperature constant [83].

More generalized theories that consider the stochastic nature of the ion arrival to the substrate, include high-order linear and nonlinear effects and additional relaxation mechanisms [78, 84-89].

2.3.2. Advanced continuum theories

In order to overcome some of the problems of the BH model, Cuerno and Barabási [90] added some terms to the differential equations that described the topography evolution. Terms representing nonlinear effects were added. The nonlinear effects are related to the incidence angle dependent sputtering yield and are responsible for the surface roughness saturation in time. Additionally, to account the stochastic arrival of ions, they added a term corresponding to Gaussian white noise η with zero mean and variance proportional to the flux J. Adding these two effects, the evolution of the topography height with the time is:

$$\frac{\partial h}{\partial t} = -\upsilon_0 + \upsilon'_0 \frac{\partial h}{\partial x} + v_x \frac{\partial^2 h}{\partial x^2} + v_y \frac{\partial^2 h}{\partial y^2} + \frac{\lambda_x}{2}\left(\frac{\partial h}{\partial x}\right)^2 + \frac{\lambda_y}{2}\left(\frac{\partial h}{\partial y}\right)^2 - B\nabla^2(\nabla^2 h) + \eta \quad (2.18)$$

The first term on the r.h.s of Eq. 2.18 represents the erosion rate of the flat surface, the second one the lateral movement of the structures on the surface, the third and forth are related to the curvature dependent sputtering, the fifth and sixth to the non-linear effects (i.e., the angle dependent sputtering), the seventh represents the surface diffusion and the last one the Gaussian white noise. The coefficients v_x and v_y can be rewritten, in terms of the BH equation (Eq. 2.8) as:

$$v_{x,y} = \frac{Ja}{n} Y_0(\theta)\Gamma_{x,y}(\theta) \quad (2.19)$$

Restricting the case to the symmetric one ($\sigma = \mu$), the coefficients in Eq. 2.18 are given by:

$$\upsilon_0 = \frac{F}{\sigma}c \tag{2.20}$$

$$\upsilon'_0 = \frac{F}{\sigma}s\left(a_\sigma^2 c^2 - 1\right) \tag{2.21}$$

$$\lambda_x = \frac{F}{\sigma}c\left\{a_\sigma^2\left(3s^2 - c^2\right) - a_\sigma^4 s^2 c^2\right\} \tag{2.22}$$

$$\lambda_y = \frac{F}{\sigma}c\left\{a_\sigma^2 c^2\right\} \tag{2.23}$$

$$v_x = \frac{F}{\sigma}a_\sigma\left\{2s^2 - c^2 - a_\sigma^2 s^2 c^2\right\} \tag{2.24}$$

$$v_y = -\frac{F}{2}a_\sigma^2 c^2 \tag{2.25}$$

where $F \equiv (E_{ion}Jp/(2\pi)^{1/2}\exp(-a_\sigma^2/2)$, p is a proportionality constant between power deposition and rate of erosion, $s \equiv \sin(\theta)$, $c \equiv \cos(\theta)$, and $a_\sigma \equiv a/\sigma$.

Eq. 2.18 resembles an anisotropic, noisy version of the Kuramoto-Sivashinsky (KS) equation [91, 92], which was originally proposed to describe chemical waves and flame fronts.

Park et al. [87] demonstrated that at short times ripples formation is described by the linear theory and after a characteristic time nonlinear effects dominate the topography evolution. The time at which the surface roughness begins to saturate is called crossover time t_c. Depending on λ_x and λ_y, after the crossover time, the nonlinear terms may destroy the ripples morphology and lead to kinetic roughening (when $\lambda_x \lambda_y < 0$) or a new morphology of rotated ripples may evolve (when $\lambda_x \lambda_y > 0$).

Facsko et al. [85] used a damped version of KS equation to explain the formation of dots under normal incidence ion bombardment or off-normal with simultaneous sample rotation on III-V semiconductors and Si surfaces:

$$\frac{\partial h}{\partial t} = -\upsilon_0 - \chi h + v\nabla^2 h - B\nabla^4 h + \frac{\lambda}{2}\left(\nabla h\right)^2 + \eta \tag{2.26}$$

The diffusion coefficient B, which is assumed isotropic, stands for the sum of all diffusion coefficients, i.e. thermal diffusion and ion-induced diffusion. The term $-\chi h$ introduces an additional dissipation [85, 93]. At certain values of χ, the solution of Eq. 2.26 corresponds to highly regular patterns with large domains of hexagonal ordering [85]. The origin of the hexagonal order is related to the damping term $-\chi h$. The ordering in hexagonal domains and the stabilization of the dots at long erosion times are

successfully predicted using this equation. The mechanism behind the damping term is not known with certainty. It may be related to redeposition; some of the sputtered particles may hit the surface and be redeposited, in particular in the case of structures with large aspect ratio. The redeposition may lead to a higher deposition rate in the depressions compared to the hillocks.

Vogel et al. [94] presented also an anisotropic damped version of KS, but they extended its application to erosion at oblique incidence. They could reproduce many different types of patterning observed experimentally, i.e. hexagonally arranged dots or ripples depending on the incidence angle. However, they could not either explain the physical meaning of the damping factor.

2.3.3. Relaxation mechanisms besides thermally activated diffusion

The BH model considers the thermally activated diffusion as the relaxation mechanism that counteracts the roughening due to the curvature dependent sputtering. However, as it was already mentioned, it was demonstrated that it could not alone explain the experimental observations [83]. Additional relaxations mechanisms have been included in theoretical models formulated after the BH model.

Makeev and Barabási [95] introduced ion-induced effective surface diffusion (ESD) as relaxation mechanism. ESD is reminiscent to surface diffusion but does not imply mass transport along the surface. It involves preferential erosion of peaks, leading to smoothing. Introducing ESD to BH equation and neglecting thermal diffusion (which is valid for low temperatures), the temporal evolution of the height is:

$$\frac{\partial h}{\partial t} = -\upsilon_0 + \upsilon'_0 \frac{\partial h}{\partial x} + v_x \frac{\partial^2 h}{\partial x^2} + v_y \frac{\partial^2 h}{\partial y^2} + \frac{\lambda_x}{2}\left(\frac{\partial h}{\partial x}\right)^2 + \frac{\lambda_y}{2}\left(\frac{\partial h}{\partial y}\right)^2 - D_x^I \frac{\partial^4 h}{\partial x^4} - D_y^I \frac{\partial^4 h}{\partial y^4} \quad (2.27)$$

The ESD coefficients D_x^I and D_y^I can be again determined from the parameters that describe the distribution of the deposited energy, from the ion flux, and the ion incidence angle. According to this approach, the wavelength of the ripples is independent of the ion flux and fluence. Also considering ESD, the wavelength increases with increasing ion energy, as it is generally observed at room temperature. However, the ripples wavelengths predicted are smaller than the experimental values, which indicates that ESD is not the only relaxation mechanism active.

It has been suggested that in the case of amorphous materials, ion-induced viscous flow confined to a thin layer at the surface contributes also to the smoothing [6, 19]. The ion-

induced viscous flow relaxation is considered to be driven by surface tension in a surface layer with reduced viscosity. The thickness of the layer is assumed to be equal to the ion penetration depth [19]. Ion-induced viscous flow leads to more accurate predictions of the temperature and ion energy dependence of the ripples wavelength for the bombardment of SiO_2 with Ar^+ than other relaxation mechanisms. The variation of the ripples wavelength considering ion-induced viscous flow is related to the temperature dependence of the viscosity. Chason et al. [6] studied the evolution of Ge surfaces during low-energy ion erosion. They observed that at temperatures of 423 K and below, the surface is amorphous and at 523 K it remains crystalline. They stated that surface diffusion is the primary smoothing mechanism on crystalline surface, while viscous flow is dominant for amorphous surfaces.

Carter and Vishnyakov [83] proposed as additional relaxation mechanism, the directed flux of atoms parallel to the surface and induced by ion bombardment. When ions are bombarded to a solid surface, they transfer not only energy but also momentum. As the ion penetrates a target, a resolved component of the momentum gained by the target is, close to the surface, antiparallel to the direction of the ion penetration, but for deeper penetration becomes parallel to the ion direction. This implies that for ions that penetrate the target obliquely, there is a component of the momentum parallel to the surface and other component normal to it. Ballistic drift is believed to play an important role particularly in the ion bombardment of silicon at near normal incidence. For normal incidence the transverse momentum will be zero, but atoms will be displaced both parallel and transverse to the incident ion direction, what it is called effective ballistic diffusion [96]. Since ballistic diffusivity and ballistic drift are dependent on the deposited energy distribution, local changes in the surface curvature will affect them. Ballistic diffusivity could explain the temperature insensitivity of ripples formation at low temperatures, but it can not alone explain the lack of ripples formation at near normal incidence, which was observed in many experimental studies [36, 40, 97]. It is thought that in that case, the ballistic drift can compensate the curvature dependent sputtering, leading to a net smoothing.

# Chapter 3

Experiments and analysis methods

In this chapter the experimental setup for the ion bombardment experiments and the characterization techniques used are presented. First, in section 3.1, the broad-beam ion equipment is described. The main operational parameters and their effect on the ion beam properties are discussed. Next, in sections 3.2 and 3.3, the physical and chemical characterization techniques used to analyze the silicon samples after ion erosion are addressed.

3.1. Ion beam equipment and characterization of the ion beam

Broad-beam ion sources [98-100] are widely used in surface modification processes. Much of their technology was originally developed for space propulsion [99]. The function of an ion beam source is to produce ions and accelerate these ions to high velocities so they are ejected downstream from the source. It consists basically of a discharge chamber, where the operating gas is introduced, an electron source used to ionize the gas and form the plasma, an extraction system that extracts the ions from the discharge chamber and accelerates them and a neutralizer situated downstream from the source.

In Fig. 3.1 a schematic representation of the ion beam equipment used for this study is shown. The source used is a home-built Kaufman-type source (ISA 150) that generates a beam of ~ 180 mm diameter. As electron source, a hot filament cathode is used, which consists of a tungsten wire that is heated to emit electrons.

There is a discharge current of electrons flowing to the anode ring ($I_{dis} \leq 5$ A), which is determined by the filament heating current. The discharge voltage (~ 30 V $\leq U_{dis} \leq 150$ V) controls the acceleration of the emitted electrons in the filament sheath [101]. The discharge voltage (U_{dis}) provides the electron energy needed to sustain the plasma in the discharge chamber. A magnetic field is generated using permanent magnets to control the movement of the electrons such that they have several collisions with the gas atoms before reaching the anode. In addition to the plasma excitation, the source performance is strongly influenced by the multiaperture grid system used. The Kaufman-type broad-beam ion source used here is equipped with a double grid system.
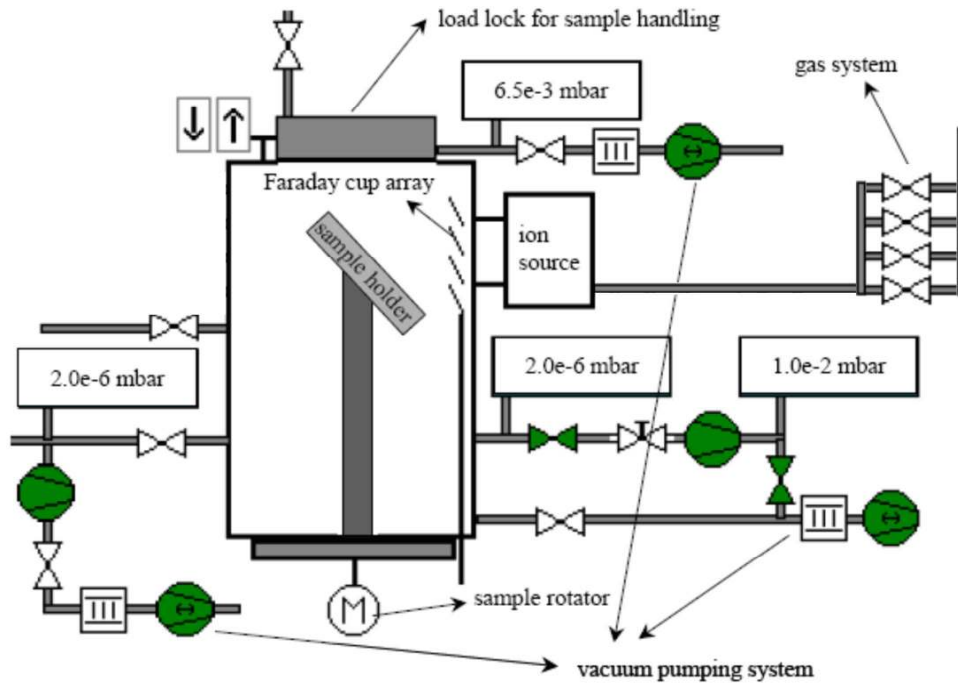
Figure 3.1. Schematic view of the ion beam equipment.

The grids are disc-shape graphite electrodes with apertures on them. Each grid has ~ 3000 hexagonally arranged apertures of 2.5 mm diameter. The total grid opening is 180 mm. The grid closest to the discharge chamber, which has a thickness of 1 mm, is the screen grid. Moving downstream, the 2 mm thick accelerator grid is placed. For most experiments presented here, the distance between the grids was 2 mm. The ions are extracted by applying specific potentials to each grid. A potential diagram of the ion acceleration process is presented in Fig. 3.2.

To accelerate the ions into the beam, the entire discharge chamber region, or source body, is raised to the potential corresponding to the desired ion energy (e.g. 1000 V for 1000 eV ions) by a power supply connected between the anode and ground. The anode potential is determined by the potential applied to the screen grid (U_{scr}); it is the sum of U_{scr} and U_{dis}. The ions that leave the plasma have the energy corresponding to the anode potential. Therefore, the anode potential is also known as beam potential U_b and, in the given experimental setup, can be varied from 100 V to 2000 V. The second grid, the accelerator grid, is at the acceleration potential (U_{acc}), which is negative with respect to ground and establishes an electric field along the source center-line.
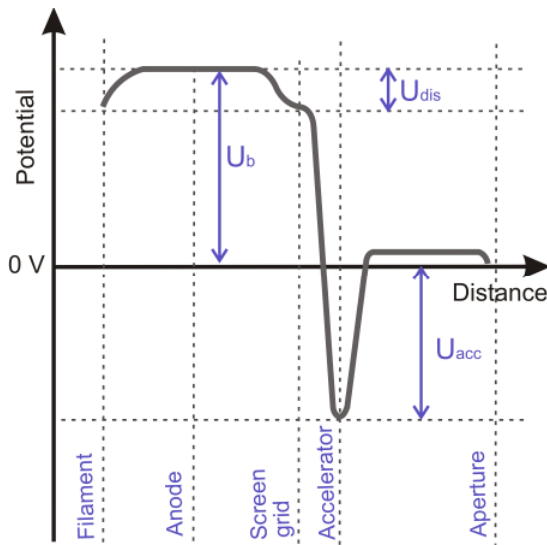
Figure 3.2. Potential configuration across the ion source.

The acceleration voltage can be varied between -1000 V $\leq U_{acc} \leq$ -10 V. Positive ions in the discharge chamber that drift close to this electric field are accelerated and extracted through the grid apertures. The beam extracted through one aperture is defined as a beamlet and the beam is formed by the superposition of all the beamlets. The trajectories of the ions are not perfectly parallel to the source axis, but divergent; i.e. the beam broadens with the distance from the source. U_{acc} determines the angular distribution of the ions within a single beamlet and in consequence, the divergence of the beam.

The grid material, its mechanical, electrical, thermal and chemical properties as well as its sputter yield under different conditions plays an important role in the life time and long term stability. Here graphite is used due to the small sputter yield and low thermal expansion coefficient.

Downstream from the extraction system, the neutralizer (hot filament tungsten wire) is placed. The purpose of the neutralizer is to emit electrons into the environment downstream from the ion beam source. The emitted electrons provide a charge balance for the ions coming from the source and the secondary electrons that leave the sample due to the ion bombardment.

To summarize, important parameters are the cathode filament current (the electrical current applied to heat the filament cathode so electrons are emitted from its surface), discharge voltage (voltage established between the filament cathode and anode, this determines the electron energy for ionizing collisions in the discharge chamber), discharge current (electrical current established between the filament cathode and

anode, this current controls the ion production rate), neutralizer filament current (electrical current applied to the neutralizer, this current heats the filament so electrons are emitted), source gas flow, beam voltage (positive voltage applied to the discharge plasma), beam current (total ion current extracted or leaving the source), acceleration voltage (negative voltage applied to the accelerator grid), accelerator current (charge-exchange current collected by accelerator grid), neutralizer emission current (electron current emitted by the neutralizer).

The mean free path length of the ions is ~ 1 m for the working pressures used, and the distance between the sample holder and the extraction system was 400 mm. Therefore, most of the extracted ions will reach the sample surface without collisions that could affect their kinetic energy.

The base pressure in the vacuum chamber was 1×10^{-6} mbar. Depending on the gas flow, the operation pressure varied from 5×10^{-5} mbar (Kr^+) to 1×10^{-4} mbar (Ar^+).

To avoid thermal effects, the samples were mounted on a water-cooled (temperature approx. 285 K) substrate holder. The sample can be rotated with respect to its axis with up to 12 rotations per minute. Additionally, the sample holder can be tilted from 0° to 90° with respect to the ion source axis. With the use of a specially designed sample holder, which possesses sites with different tilt angles, variations of one degree can be introduced.

The determination of the ion beam properties is essential for a good control and understanding of the ion beam source performance. One way to estimate the ion beam properties and their dependence on different operational parameters is by simulations.

The effect of U_{acc} in the angular distribution of the ions within the beamlet determined by simulations [32] is presented in Fig. 3.3. The simulations were performed using the commercial computer IGUN code [102]. As input parameters, the geometrical dimensions, voltage settings, plasma density, and electron temperature were used. First, the shape of the plasma sheath boundary at the screen grid was determined. The ion trajectories were then calculated by solving the Poisson equation taking the space charge effects into account. The geometry data of a single beamlet formed from one screen and accelerator grid holes were used for the calculation, and the total beam profile was superimposed from these elementary objects [101]. According to the simulations, which were performed for the ion source used in this investigation for $E_{ion} = 2000$ eV, for $U_{acc} = -200$ V most ions leave the grid with an angle between 2° and
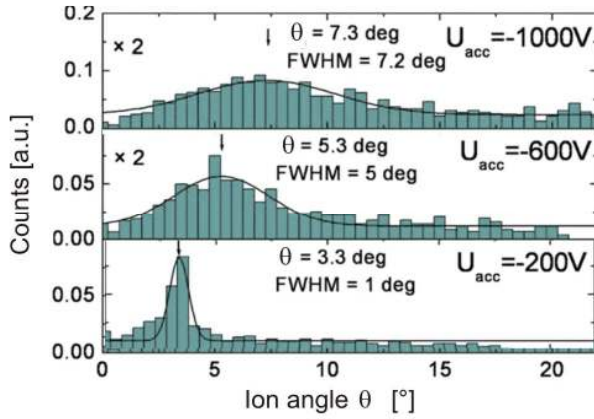
Figure 3.3. (a) Simulation of the angular distribution of the ions within a beamlet [32] for $-U_{acc}$ of 200 V, 600 V, and 1000 V and a plasma density of 2×10^{10} cm^{-3}. The solid curves represent a Gaussian fit of the histograms.

5° with respect to the source axis, with a maximum at ~ 3.3° with a full width at half maximum (FWHM) of 1°. With increasing $|-U_{acc}|$, the distribution broadens and the maximum shifts toward larger angles. For $U_{acc} = -1000$ V the maximum position changes to 7.3° and the FWHM to 7°.

The potentials applied at the extraction system are not the only parameters affecting the angular distribution of the ions within the beamlet. In fact, the angular distribution is determined by the shape and position of the plasma sheath near the screen grid. The plasma sheath is a transition region separating the discharge plasma (i.e., the ion production region where local ion and electron number densities are equal) from the ion acceleration region where only ions are present. It determines the starting point of the ion acceleration and influences the resulting ion beam properties. The plasma sheath is expected to vary in position and shape as result of variations in the accelerator system potentials, in the plasma density (i.e. beam current) and in the extraction system geometry.

With respect to the grid geometry, Fig. 3.4 shows simulated beamlets using the IGUN code [102] for a grid distance of 1 mm (left) and 2 mm (right) at various plasma densities. At lower plasma density (upper plots) the increase of the grid distance decreases the beamlet divergence due to the reduced focusing strength of the grid potential distribution. At larger plasma densities (bottom plots), however, the larger grid distance leads to a higher beamlet divergence. In regard to the grid geometry, it is also known that due to the grid erosion, the diameter of the grid apertures increases with the operation time. Tartz et al. presented a grid erosion code developed to predict the grid alteration and the validation of the results with experimental data [103]. In general, it is observed that the increase in the aperture diameter leads to a decrease of the beamlet
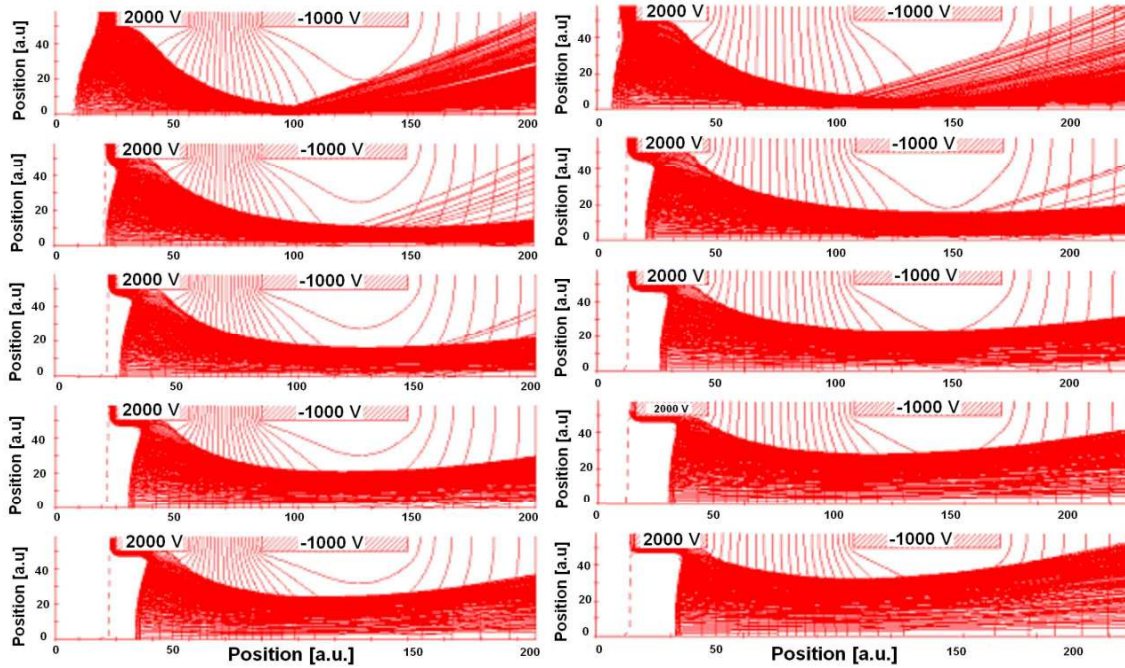
Figure 3.4. Simulated beamlets at various plasma densities and grid distances (left: 1 mm, right: 2 mm) for $E_{ion} = 2000$ eV, $U_{acc} = -1000$ V. The plasma density from top to bottom: 5.0×10^{10}, 7.5×10^{10}, 1.0×10^{11}, 2.5×10^{11}, and 5.0×10^{11} cm^{-3}

divergence. There are other reports with detailed analysis of the correlation between experimental parameters and beam properties [101, 103-107]. For this study, the ion current density of the beam was measured before and after each erosion experiment using a Faraday cup array. Five probes are placed between the extraction system and the sample holder covering an approximate surface area of 150 cm^2. One probe is in the centre of the beam and the other four at ~ 7 cm from it. Since the ion source used in this study produces a beam with a nearly Gaussian distribution of the ion current density, the current density at the centre is usually up to ~15 % higher than at the edges, depending on the operational parameters. The topography evolution is, in general, not affected by variations in the current density.

In addition to the measurements from the five Faraday probes, an indirect measurement method was used. Assuming that the ion current density is proportional to the erosion rate, etch depth profiles can be used to estimate the variation of the ion current density across the beam. 4 inches silicon wafers with a 800 nm SiO$_2$ layer were used. They were sputtered under different experimental conditions and then the thickness of the remaining SiO$_2$ layer was determined using Spectroscopic Reflectometry (Nanocalc 2000 [108]).
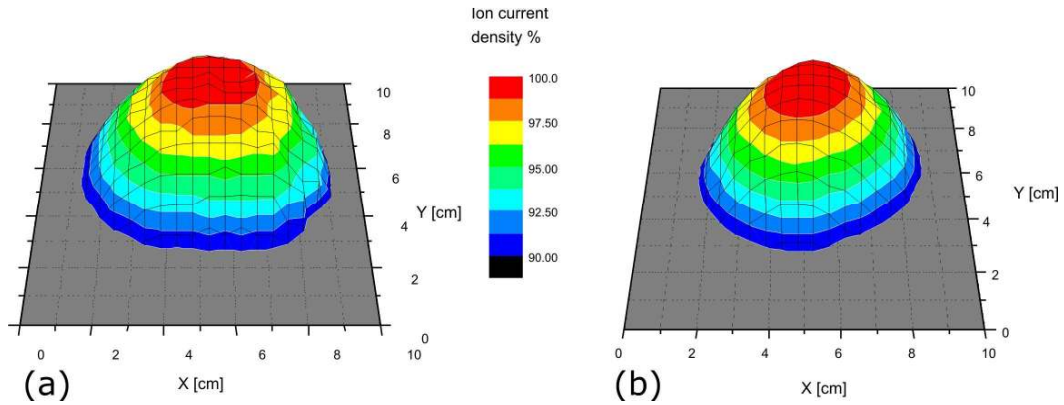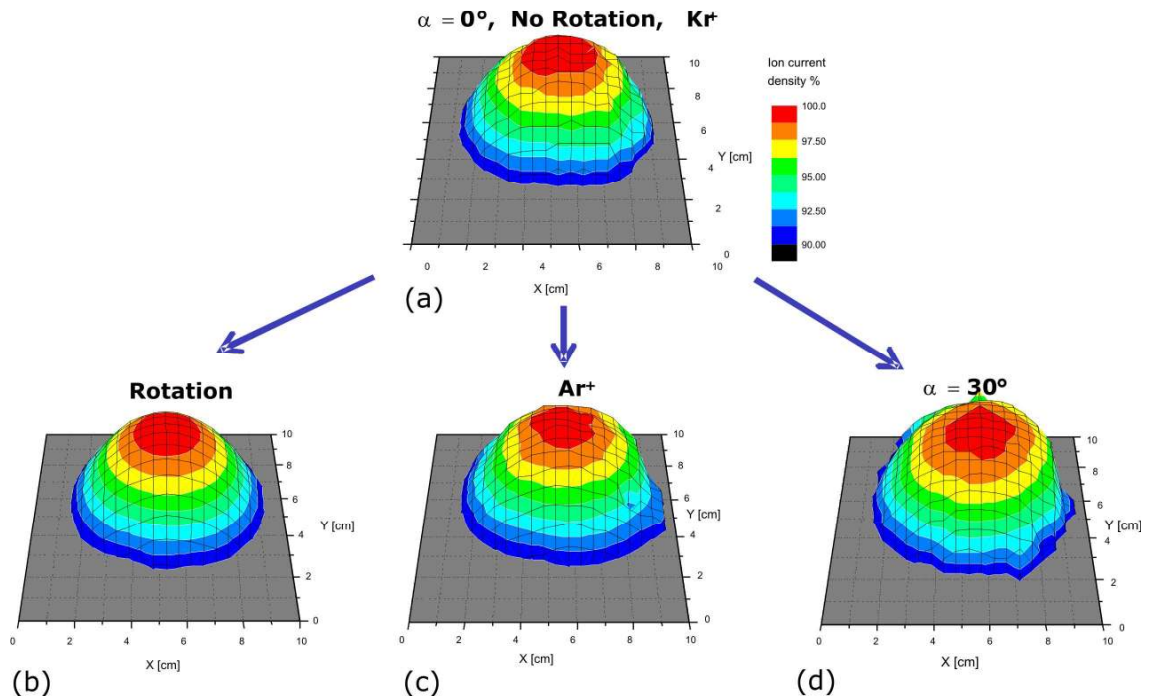
Figure 3.5. Effect of U_{acc} in current density profile. U_{acc} = -1000 V (a) and -200 V (b)

From the etch profiles, the distribution of the ion current density of the central part (100 mm diameter) of the beam was estimated.

In Fig. 3.5 the beam profile for 2000 eV Kr^+ without rotation of the sample and at normal incidence is represented. The ion current density at the centre of the beam was 300 µA cm^{-2}. The current density ranges from 300 µA cm^{-2} (represented as 100%) to ~ 270 µA cm^{-2} (90%) is plotted. The profiles in Fig. 3.5a and 3.5b correspond to U_{acc} = -1000 V and U_{acc} = -200 V, respectively. In the first case the beam seems to be more divergent, in agreement with the simulations results shown above

In Fig. 3.6 the profile corresponding to 2000 eV Kr^+ at normal incidence without

Figure 3.6. Effect of rotation, ion species, and incidence angle on current density profile.

rotation (Fig. 3.6a) is compared with the profiles under different experimental conditions to see the effect of the parameters on the profile. In Fig. 3.6b the effect of rotation of the sample during irradiation is shown. The sample was rotated at 12 rpm around the surface normal. The effect of using Ar^+ as the ion species instead of Kr^+ is shown in Fig. 3.6c. And in Fig. 3.6d the effect of tilting the sample holder from 0° to 30° is presented. The shape of the ion current density profile shows no pronounced changes with the three experimental parameters analyzed.

.

3.2. Surface characterization

Performing an accurate characterization of the surface is essential for the fabrication of nanostructures.

The main technique used in this study for the topography characterization after ion erosion was Atomic Force Microscopy (AFM), which allows a relatively accurate quantification of the surface topography. As complementary techniques, Scanning Electron Microscopy (SEM) and High Resolution Transmission Electron Microscopy (HRTEM) were applied. Additionally, two optical techniques were used: White Light Interferometry (WLI) for the characterization of the eroded craters resulting from the Secondary Ion Mass Spectrometry (SIMS) analysis and Spectroscopic Reflectometry (SR) for the measurement of the etch profiles as part of the ion beam characterization process.

As it was already mentioned, foreign atoms that are incorporated during ion bombardment seem to be involved in the pattern formation on silicon. Therefore, the chemical characterization of the samples is also required. For this work, Secondary Ion Mass Spectrometry (SIMS), Rutherford Backscattering Spectrometry (RBS), Particle Induced X-ray Emission (PIXE), and Electron Energy Loss Spectroscopy (EELS) were used.

In this subsection, the main techniques used for the physical and chemical characterization of the surfaces after ion erosion are described.

3.2.1. Atomic Force Microscopy (AFM)

Atomic Force Microscopy (AFM) [109-113] is a very useful high-resolution technique to study material surfaces and obtain a real three-dimensional profile. For the examination of the topography, the samples do not require special preparation,

conductive and insulator surfaces can be analyzed, and usually no vacuum system is required, as most AFM modes can work in ambient air or even liquid environments. A high-quality topographical characterization of the surface is achieved, even when features of small size (below 50 nm) and low aspect ratio (ratio height to length) are present. AFM is one type of Scanning Probe Microscopy (SPM). As in other SPM techniques, a sharp probe, scanned across the sample, is employed to detect changes in surface. A sharp force-sensing tip at the end of a cantilever interacts with the sample surface. As the interaction between the cantilever tip and the surfaces varies, the cantilever is deflected. The deflections are measured and used to compile a topographic image of the surface. Usually, a laser beam is used to measure the deflections; it is deflected from the backside of the cantilever and directed to a detector (see Fig. 3.7).

There are three main operation modes in AFM: contact mode, non-contact mode and tapping or intermittent contact mode. The latter was the mode used for this study. In tapping-mode AFM the cantilever vibrates at a fixed frequency near resonance with large vibration amplitude, so at the lower limit of the movement, the tip just touches the sample surface. The amplitude is held constant when the tip is far from the surface, and decreases due to cyclic repulsive contact between the tip and the surface. The surface structure is obtained by maintaining the vibration amplitude at the constant level using the feedback circuit [112]. The vertical position of the scanner at each data point varies in order to maintain a constant amplitude and the variations in height are stored (*height signal*) to form a topographic image of the sample. The term *setpoint* refers to the desired voltage at the position-sensitive detector (and, therefore the desired deflection of the cantilever). The setpoint voltage is constantly compared to the actual cantilever deflection voltage to calculate the desired change in the piezo position. The difference between them is known as the *amplitude error signal*. The error signal can be also used to generate images of the surface. The error signal images, which might be considered as maps of derivatives of height corrugations, emphasize large local gradients that are poorly resolved in the height images. If not otherwise specified, the AFM images presented in this work were obtained from the height signal.

The AFM measurements for this study were performed using Dimension 3000 with a Nanoscope IIIa controller, which can record up to 512 points per line, in TappingMode[TM] from Veeco Instruments [114]. Also MFP-3D AFM from Asylum Research with a high resolution (up to 4096 points per line) was used [115].
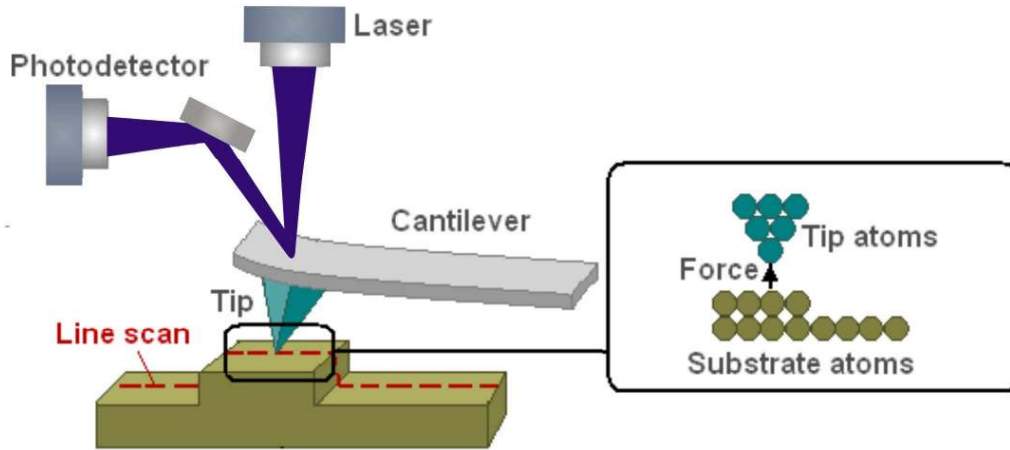
Figure 3.7. Schematic drawing of the basic operation principle of AFM.

For the AFM image processing, SPIP 4.8.0 [116] was used. The SPIP (Scanning Probe Image Processor) software package has specialized tools for correcting and analyzing SPM data. For the AFM measurements performed for this study Olympus [117] Si cantilevers with tetrahedral Si tips were used. The cantilevers are 160 μm long, 50 μm wide, and 4.6 μm thick and have an aluminium reflex coating on the backside. The Si tips have a height of ~ 11 μm, and radius smaller than 10 nm (typical value 6 nm). The resonant frequency of the cantilevers is in the range of 200 to 400 kHz (with a typical value of 300 kHz) and the spring constant is between 12 and 103 N/m (typical value of 42 N/m). Special attention was given to prevent artifacts in the measurements.

For the height fluctuations analysis of the resulting topography, the statistically most important parameter is the root mean square (RMS) roughness (also w), which can be calculated from the height profiles from the AFM images, and is given for a digitalized surface by [118]:

$$< w >_N = \left\{ \frac{1}{N} \sum_{i=1}^{N} [h_i - < h >_N]^2 \right\}^{1/2} \tag{3.1}$$

where $<h>$ is the average surface height, N the number of measured points.

For surface topographies with one dominant length scale, a correlation between the RMS roughness and the amplitude of the topographical features can be assumed.

The RMS roughness belongs to the first order statistical quantities used to describe rough surfaces. The first order statistics describe only the statistical properties of the individual points; they do not reflect the lateral dimension of the features. Two surfaces

with the same height distribution and RMS roughness may look totally different if the changes in height occur in different length scale along the surfaces, i.e. the height fluctuations frequencies are different.

Therefore, additional statistical quantities are necessary for an appropriate characterization. Second order statistics quantities consider relationship of two points on the surface. Here, the power spectral density (PSD) will be utilized.

In order to obtain the PSD function and to consider the frequency properties of the topography, the reciprocal (or Fourier) space is much more convenient than the real space. Performing the two dimensional Fast Fourier Transform (2D-FFT) of the height profiles from the AFM images, information about the presence of dominant frequencies can be obtained. Periodic elements in the topography and anisotropy can be detected.

As examples, in Fig. 3.8, three AFM images of Si surfaces after ion bombardment and their corresponding FFT diagrams are shown. Since the AFM images shown here are 2×2 μm^2 and their resolution 512×512 pixels, the spatial frequency of the FFT images goes from -127.5 μm^{-1} to +127.5 μm^{-1}. The spatial frequency has a minimum at the centre of the image and increases moving away from the centre. It ranges from $-(N/2-1)/L$ to $+(N/2-1)/L$, where N is the number of data points and L the length of the measured window. From the FFT images, the dominant spatial frequencies can be obtained (lighter spots, rings). The central spot, which is called DC term, represents an average intensity of the whole image and is not relevant for the topography analysis. The lack of preferred orientation is observed in the FFT diagrams of the samples with dots (Fig. 3.8d and 3.8e), and it is a sign of the isotropic distribution of the structures on the surface. On the other hand, the FFT corresponding to the ripples (Fig. 3.8f) shows some anisotropy. The spots are aligned in the direction of the ripples wave vector. The position of the first spot indicates the characteristic frequency of the ripples, i.e. the inverse of the separation of the features in the real space. In the case of the dots, it is indicated by the position of the first ring. Here, the separation of the features will be considered to be the wavelength, in the case of the ripples and the mean size, in the case of the dots. Additional spots (or rings) indicate a higher lateral ordering of the structures. The width of the spots (or rings) is related to the homogeneity and spatial correlation of the features. Narrow spots (or rings) correspond to narrow size distributions. Thus, the presence of a ring in the FFT in Fig. 3.8d indicates a higher homogeneity in the size of the dots, in comparison with the FFT in Fig. 3.8e, where a

disk is observed. To facilitate the quantification of the information present in the FFT diagrams, the Power Spectral Density (PSD) functions are used. They are obtained from the FFT spectra and provide quantitative information about height and lateral distributions.

Additionally, information about dominant relaxation mechanisms can be obtained from the decay of the PSD in the high frequency region [119]. The area- or 2D-PSD(f_x,f_y) is the average of the Fourier transform magnitude squared:

$$PSD(f_x, f_y) = \lim_{L\to\infty} \frac{1}{L^2} \left| \int_{-L/2}^{L/2} \int_{-L/2}^{L/2} h(x,y) \times exp\left[-2\pi i(f_x x + f_y y)\right] dxdy \right|^2 \qquad (3.2)$$

where the surface topography data are $h(x,y)$, f_x and f_y are the spatial frequencies of the surface roughness, and L is the length of the measured window.

For this study, however, the angular-averaged Power Spectral Density PSD(f) functions
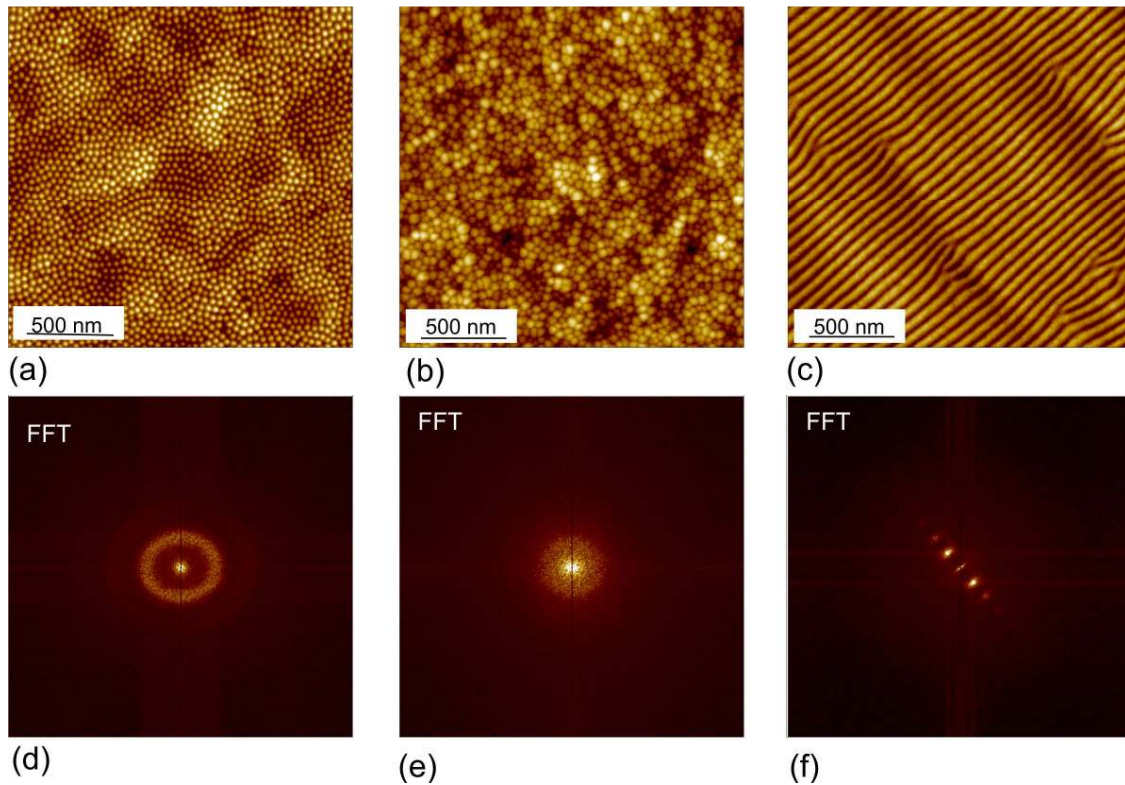
Figure 3.8. (a-c): AFM images of Si(001) after ion sputtering under different experimental conditions. The height scale is 20 nm (a, b) and 10 nm (c). The RMS roughness is 3.2 nm (a), 3.0 nm (b) and 1.6 nm (c). (d-f): FFT diagrams with frequency range of -127.5 µm^{-1} to +127.5 µm^{-1}. Each FFT diagram corresponds to the sample above.

were used to analyze the data. The angular-averaged PSD(f) is obtained performing angular averaging over all spatial frequencies with constant distance $f^2 = f_x^2 + f_y^2$.

Although the angular-averaged PSD(f) is in particular useful for isotropic structures, it can be also used for anisotropic features; e.g., in the case of the ripples presented in Fig. 3.8c, the main contribution to the PSD(f) will be given by the characteristic frequency, i.e. the spots. For the rest of the work the notation PSD will be used to indicate the angular-averaged PSD(f) function.

The PSD functions were obtained from the 2D-FFT diagrams using the software R-PSD [120] written in the Matlab programming language.

It is known that the RMS roughness (also w) can be obtained from the area under a band-limit part of the PSD function [121]:

$$< w > = 2\pi \int_{f_{min}}^{f_{max}} PSD_{2-D}(f) f df \tag{3.3}$$

In Fig. 3.9 PSD functions for three Si samples are shown. The surface topographies are different, one has a random roughness, one has ripples on it and the last one is relatively smooth. Useful information can be deduced from the diagrams. For example, the larger area under the PSD curve for the *random rough* sample shows its higher roughness in comparison with the *smooth* sample. When regular features are present on the surface, one or more characteristic peaks are observed in the PSD diagrams. This can be observed in Fig. 3.9 for the *ripples* sample. The peak with higher intensity is the first order peak and its position indicates the characteristic spatial frequency of the ripples in the real space, i.e. the separation between the ripples, which will be here considered the wavelength of the ripples λ. Additional peaks indicate high lateral ordering.
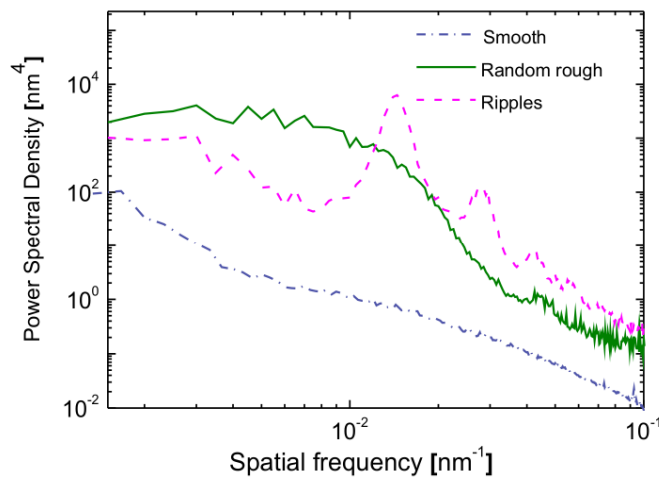
Figure 3.9. PSD functions of three silicon samples after ion bombardment under different experimental conditions. The samples present different topographies.

The PSD diagram of nanodots looks similar to the diagram corresponding to the ripples, and from the position of the first order peak, the lateral size of the dots can be estimated. Additionally, an important parameter that describes the lateral ordering can be deduced from the PSD functions, the system correlation length ζ. ζ gives the scale up to which spatial correlation is present, i.e. the mean domain size of nanostructures. It can be deduced from the full width at half maximum (FWHM) of the first order peak, since the system correlation length ζ is inversely proportional to the FWHM ($\zeta \sim 1/\text{FWHM}$) [118]. Next, an example will be given to show the AFM data treatment for the topography characterization. A Si(001) sample was irradiated with 750 eV Kr$^+$, at $\alpha = 20°$, with $U_{acc} = $ -1000 V, with $\Phi\ \square = 6.7 \times 10^{18}$ cm^{-2}. Visual inspection of the AFM height signal image (Fig. 3.10a) shows the presence of short wavelength ripples perpendicular to the ion beam projection, which is indicated with the white arrow, and long wavelength undulations parallel to it. From this image, the 2D-FFT image (Fig. 3.10b) was obtained. The 2D-FFT gives information about spatial frequencies (ranging from -68.15 µm^{-1} to +68.15 µm^{-1}). The spots indicate the existence of periodic components in the topography. By extracting the averaged line profiles in the X and Y direction (Fig. 3.10c and 3.10d), the peaks indicating the dominant frequencies can be observed. The vertical profile (Fig. 3.10d) shows clearly a peak at the centre and two
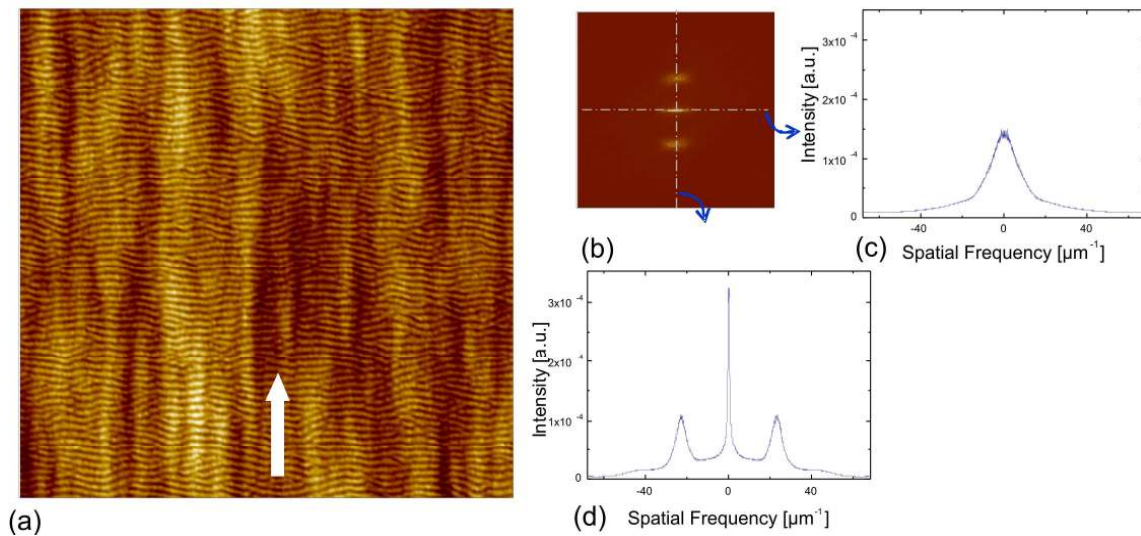
Figure 3.10. (a) Height signal AFM image of Si(001) irradiated with Kr$^+$ ($E_{ion} = 750$ eV, $U_{acc} = $ -1000 V, $\alpha\ \square = 20°$, $\Phi = 6.7 \times 10^{18}$ cm^{-2}). The white arrow indicates the projection of the ion beam on the surface. The size of the image is 10 x 10 µm^2 and the height scale 4 nm. (b) 2D-FFT image and corresponding X- (c) and Y- (d) profiles.

additional peaks at the left and the right of the central peak. The two peaks at the sides correspond to the short wavelength ripples. From the peak frequency, the wavelength of the ripples in the real space can be determined, which is ~ 45 nm in this case. However, the *X*-profile (Fig. 3.10c) shows no peak indicating periodic components; no information about the parallel undulations is provided. If the amplitude error signal image instead of the height signal image is used, additional information about the topography is obtained.

It was already mentioned in this subsection that the error signal is the difference between the oscillation amplitude of the cantilever and the set point amplitude. It represents approximately the first derivative of the surface in the scan direction. It sharpens the contrast of features and enhances the large surface gradients. In Fig. 3.11
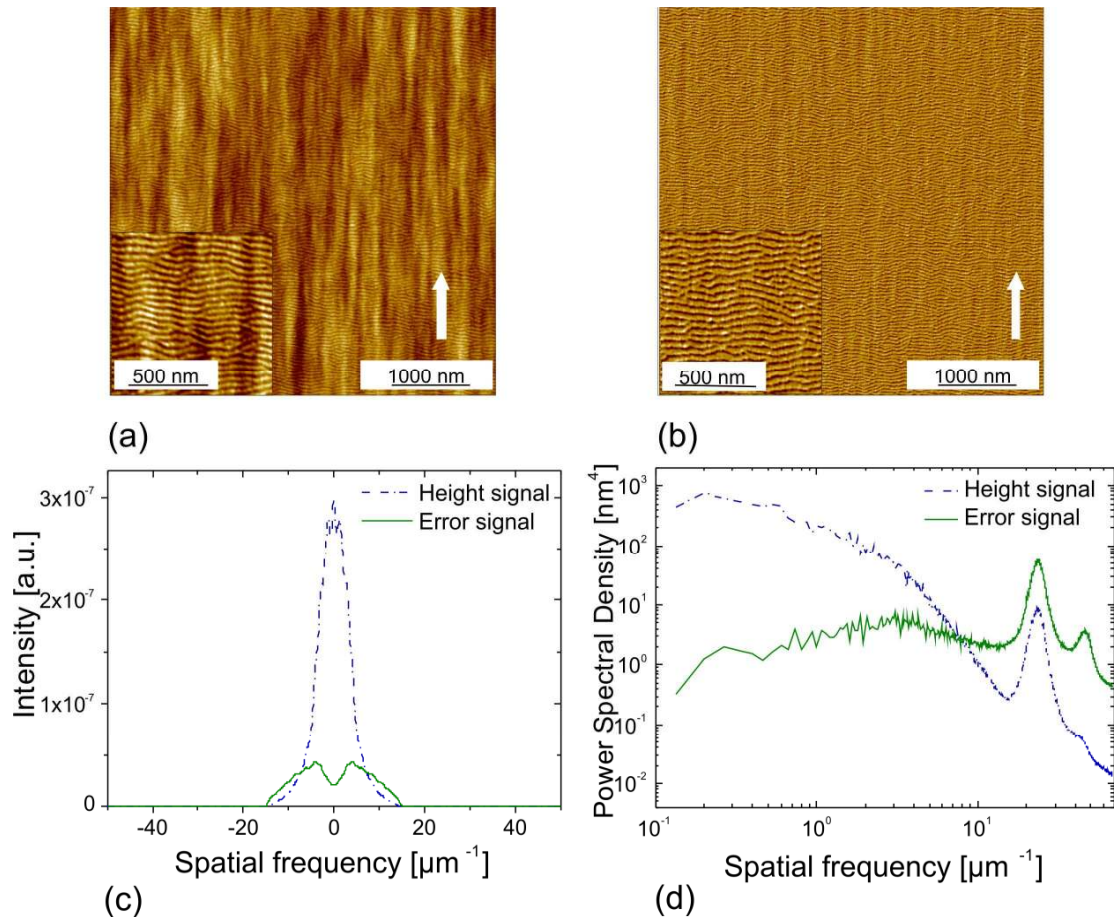
Figure 3.11. AFM images from height (a) and amplitude error (b) signal of Si(001) irradiated with Kr$^+$ (E_{ion} = 750 eV, U_{acc} = -1000 V, α = 20°, Φ = 6.7 × 10^{18} cm^{-2}). The size of the images are 5 × 5 μm^2 and the insets 1 × 1 μm^2. The Z scale of the height signal image (a) is 4 nm and of the amplitude error signal image (b) is given in V. (c): 2D-FFT averaged *X*-profiles obtained from both images. (d): corresponding PSD diagram.

height signal (Fig. 3.11a) and amplitude error signal (Fig. 3.11b) images of the same sample presented above are shown. The same procedure as in Fig. 3.10 was applied to the amplitude error signal image. The averaged *X*-profile from the amplitude error and height signal images are shown in Fig. 3.11c. The *X*-profile from the amplitude error signal presents two peaks that correspond to the undulations parallel to the ion beam, and thus their wavelength can be estimated.

The PSD diagrams from the height and amplitude error signal images are presented in Fig. 3.11d. While the PSD from the height signal image shows the peak at high frequencies representing the short wavelength perpendicular ripples, in the PSD from error signal, an additional weaker peak at lower frequencies is observed and it corresponds to the parallel undulations. This peak is broader, which indicates a higher dispersion in the undulations wavelength. By testing this methodology for different topographies, a difference of up to 20 % between the ripples wavelength calculated from the height signal and the error signal was found. However, in the presence of low regular features, the error signal images were used, as no better alternative procedure was found.

3.2.2. Scanning Electron Microscopy (SEM)

In Scanning Electron Microscopy (SEM) [122-125] a finely focused electron beam is rastered in vacuum over the sample surface. As the energetic electrons reach the solid surface, they undergo a series of elastic and inelastic scattering events in the material. Different signals result from these interactions. In the most standard imaging mode secondary electrons, which are generated by inelastic scattering, are used. Secondary electrons produce topographic contrast with high resolution and large depth of field. They are emitted with energies less than 50 eV. Due to their low energy, they escape from the material only from the top 100 Å region of the surface. The secondary electron coefficient depends strongly on the electron beam energy; at lower energies, they are generated closer to the surface, and thus they have higher escape possibility. At higher electron beam energies, the number of secondary electrons increases but they are excited deeper in the specimen, and thus their escape probability decreases. The secondary electron yield, which depends also on the surface gradient, increases with increasing tilt angle. Thus, more secondary electrons are produced from the tilted

regions of the specimen, and this provides an important mechanism for the surface topography imaging.

Also backscattered electrons can be used for imaging. They are emitted with energies close to that of the incident electron beam. Typically, 10 to 30 % of the primary electrons become backscattered electrons, which emerge from the upper one-half of the excitation volume. The spatial resolution is on the order of the diameter of the excitation volume. Backscattered electrons provide information on the topography, as well as atomic number contrast since regions of higher atomic number backscattered more primary electrons.

For this study, a Zeiss Ultra 55 with Gemini®-column was used [126]. The microscope works with a probe current up to 100 nA and acceleration voltages from 0.2 to 30 kV. It possesses two detectors for the secondary electrons. One is an annular in-lens detector located inside the electron column. The other is an out-lens, namely Everhart-Thornley detector, on the wall of the specimen chamber. It has also an energy and angle selective detector for the backscattered electrons (EsB®). This detector separates and detects the backscattered electrons with an efficiency of around 85 %. The magnification of the microscope can be varied from 12 to 1 000 000 × in the secondary electrons mode, and from 100 to 1 000 000 × with the EsB® detector. The samples were analyzed in the secondary electron mode, with acceleration voltage of 15 kV, for which a resolution of ~ 0.8 nm can be reached.

3.2.3. High Resolution Transmission Electron Microscopy (HRTEM)

Transmission Electron Microscopes (TEM) [124, 127, 128] work in the same way as scanning electron microscopes, except that the transmitted part of the electrons is analyzed. It is usually used to study the internal microstructure and crystal structure of samples which are thin enough to transmit electrons with relative small loss of energy. Therefore, the ideal thickness of the sample may be in some cases in order of 15 nm or even less [128]. It represents a good complementary technique to SEM, since it has a greater resolving power, it can provide surface sensitive diffraction data and images. Additionally, it can be combined with X-ray and electron energy loss spectroscopy [124].

In HRTEM the image formation is based on the phase contrast mode, which is the most difficult contrast mechanism to image in transmission electron microscopy, but it is also

the mode that provides images with higher resolution. It is related to the phase lag in the electron wavefront introduced by the passage of the electrons through the sample. The retarded phase will interfere with another wave, giving phase contrast.

For this study the HRTEM measurements were performed using a JEOL JEM 4010. This microscope has a LaB_6 emitter and can be operated from 100 to 400 kV. It has a point-to-point resolution of 0.16 nm. For the measurements presented here, it was operated at 400 kV acceleration voltage. Cross sectional samples were prepared by gluing samples face to face, wire saw cutting, plane-parallel grinding, polishing, and ion beam etching with 2.5 keV Ar^+.

3.2.4. Electron Energy Loss Spectroscopy (EELS)

Electron Energy Loss Spectroscopy (EELS) [129, 130] is a chemical analysis technique that is available in transmission electron microscopes. By this technique, the energy loss of inelastically scattered electrons is analyzed. The intensity of inelastically scattered electrons at given energy loss is measured by a spectrometer and a spectrum is obtained. The energy range of EEL spectra is typically from 0 to 3 keV. The region of high energy loss (~ 50 eV to several thousand electron volts) reflects the atomic character of the specimen. It corresponds to the excitation of electrons from localized orbitals on a single atomic site to extended, unoccupied electron energy levels just above the Fermi level of the material. As the energy loss increases, this region exhibits steps or edges superimposed on the monotonically decreasing background intensity. The edges correspond to excitation of inner-shell electrons and are known as ionization edges.

For this study the EELS measurements were performed using a VG HB501 (Vacuum Generators) dedicated Scanning Transmission Electron Microscope (STEM). The dedicated STEM is equipped with a cold field emission gun with energy width 0.4 eV. The beam energy can be varied from 5 to 100 keV. For the measurements performed for this study, a 100 keV beam with a diameter of ~ 1 nm was used. A Gatan parallel EELS spectrometer (Enfina 1000) was used to record the EEL spectra. Two entrance apertures with different sizes can be used to limit the collection angle and to control the exposure time. The electrons with different energy are dispersed in a magnetic prism and a YAG / CCD system (yttrium aluminium garnet / charged-coupled device) converts the energy of the electrons into a digital count.

3.2.5. Secondary Ion Mass Spectrometry (SIMS)

Secondary Ion Mass Spectrometry (SIMS) [131-135] is a highly sensitive technique for determining the surface and near-surface elemental composition of solid substrates. The basic principle of this technique is to analyze the charged particles that are ejected from a solid due to ion sputtering by mass spectrometry. The high sensitivity of SIMS makes it suitable for trace-element detection (in the ppm-ppb range).

SIMS provides different kind of analytical information depending on the mode used. Static SIMS identifies the elemental composition of the uppermost monolayers. Secondary ion mapping measures the lateral distribution of atoms and molecules on the substrate surface. The third approach of this technique is compositional depth profiling, which was the mode used for this study. Two separate beams were utilized. With an O_2^+ sputter ion beam material was removed from the surface and with a Ga^+ ion beam an area within the crater bottom was analyzed. The bombardment of the sample with these two beams was alternated until the desired depth was reached. The detection method was Time of Flight (ToF) mass spectrometry.

The raw data in a SIMS depth profile consists of the detected counts, or intensity, for some species at different sputtered times. The conversion of signal intensity to density can, in principle, be calculated knowing the primary ion beam current, the sputter yield, ionization efficiency, atomic fraction of the ion analyzed, and an instrumental factor. However, some of these factors are generally poorly known. The usual approach is one of using standards with composition and matrices identical or similar to the unknown. The matching of the standard and the unknown and the analysis conditions of both is usually complex.

From the standards, relative sensitivity factors (*RSF*) from the elements of interest are obtained. The *RSF* are conversion factors defined by:

$$\frac{I_R}{C_R} = RSF_E \frac{I_E}{C_E} \qquad (3.4)$$

where RSF_E is the relative sensitivity factor for element E, I_E secondary ion intensity for element E, I_R secondary ion intensity for reference element R, C_E concentration of E, C_R concentration of R. Usually, the matrix M element is used as the reference.

$$C_E = RSF_E \frac{I_E C_M}{I_M} \qquad (3.5)$$

If the concentration of the elemental matrix is assumed to be constant (valid for trace element analysis), a constant *RSF* can be obtained:

$$RSF = C_M \ RSF_E \tag{3.6}$$

And the concentration of the element analyzed results:

$$C_E = RSF \frac{I_E}{I_M} \tag{3.7}$$

For some applications, it is necessary to convert the sputtering time into depth. The depth scale is usually quantified by measuring the depth of the SIMS crater after analysis. For this study, the crater depth was measured using white light interferometry (WLI). For the SIMS measurements performed for this work, an area of 300×300 μm^2 was sputtered with 0.5 keV O$_2^+$ and a 15.0 keV Ga$^+$ beam was used to analyze a 40×40 μm^2 area.

The sensitivity factors *RSF* used were taken from [136] and they were measured from a silicon matrix using a 8.0 keV O$_2^+$ primary ion beam at 39° from the normal. As the measurement conditions used here were different, i.e. the quantification is not accurate, RBS was utilized as a complementary technique. The results about the total concentration of the elements obtained with RBS are more reliable and are considered to represent the area under the curve in the SIMS depth profiles. Ten samples were measured using both techniques and a correction factor was obtained and used to correct the SIMS results. The correction factor, i.e. the ratio between the concentrations obtained by SIMS and RBS (C_{RBS}/C_{SIMS}) was 0.69 with a standard deviation of 0.06. All the SIMS results presented in this study were already corrected by this factor. As an example, in Fig. 3.12 a depth profile measured by SIMS is shown.
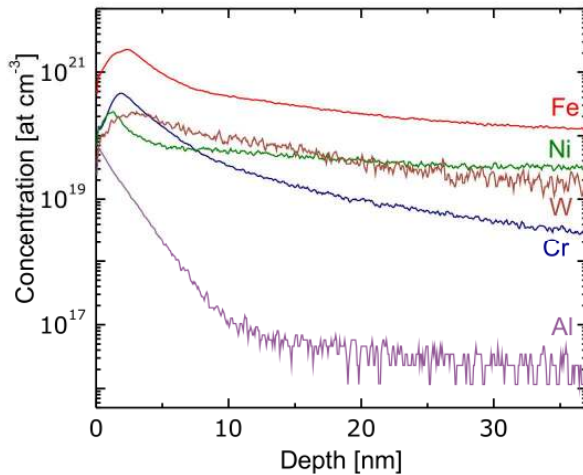
Figure 3.12. Depth profile (SIMS) of the concentration of metallic elements on Si(001) after sputtering with Kr$^+$ ($E_{ion} = 1000$ eV, $U_{acc} = -1000$ V, $\alpha = 15°$, $\Phi = 6.7 \times 10^{18}$ cm^{-2})

3.2.6. Rutherford Backscattered Spectrometry (RBS) and Particle-Induced X-ray Emission Spectrometry (PIXE)

Rutherford Backscattering Spectrometry (RBS) [137-140] involves the analysis of the energy of ions that backscatter after colliding with atoms in the near-surface region of a substrate, i.e. the ions that are elastically scattered backwards through an angle close to 180°. The ratio of the energy of the ions after the scattering process to the incident energy, the so-called kinematic factor, gives information on the mass of the encountered nuclei. Analyzing the energy spectra of the backscattered ions, detailed information about the atomic masses can be obtained. When light primary ions are used (e.g., H^+ or He^+), there is much greater separation between the energies of particles backscattered from light elements than from heavy elements because a significant amount of momentum is transferred from the incident particle to the light target atom. As the mass of the target increases, less momentum is transferred to the target atom and the energy of the backscattered particle approaches the incident particle energy. This means that RBS has good mass resolution for light elements but poor mass resolution for heavy elements. However, the elements lighter than the incident particle can not be detected as these elements will scatter at forward trajectories with significant energy [140].

RBS provides absolute quantitative analysis and it does not require the use of standards. However, RBS detectability depends on the matrix: elements lighter than the matrix are not readily detectable. Additionally, as most of the ion beam based techniques, RBS is not sensitive to the chemical state [137].

It is possible to apply other analytical techniques in the same facility; e.g., Particle-Induced X-ray Emission (PIXE). In PIXE [139, 141] a sample is irradiated by a beam of protons or heavier ions and the X-ray emitted by the deexcitation of the atoms in the sample are analyzed using a suitable spectrometer. The X-ray spectrum is determined by the energy levels of the electrons in the atom. In order to calculate the elemental concentrations in the irradiated specimen, the area of each X-ray peak has to be determined. Computer codes have been developed for this matter.

The element quantification in PIXE is often more unambiguous than in the case of RBS, which sometimes suffers from limited mass resolution [139]. For this study, PIXE measurements were performed only for some samples, to corroborate the RBS results.

RBS and PIXE measurements were performed at the ion nanoprobe LIPSION [142] (the ion beam facility of the University of Leipzig). The main component of the laboratory is a 3.5 MV Singletron[TM] [143] accelerator. Protons (H^+), H_2^+ molecules and $^4He^+$ ions are produced by an RF source. From the accelerator, the beam can be bent into five different beamlines by switching magnets. To direct it to the RBS / PIXE / channelling measurements chamber, the beam is deviated in 45°. An additional 90° analyzing magnet is used to direct the beam into the nanoprobe, designed for extremely high resolution work.

In the RBS / PIXE / channelling chamber, there is beam-guiding system with two apertures for the ion beam collimation, a CANBERRA Annular PIPS detector (for RBS) and a RÖNTEC Si(Li) detector (to detect X-rays for PIXE).

The RBS detector has an active surface area of 50 mm^2 and a resolution of $\Delta E = 11$ keV for He^{2+}. The arrangement of the detector corresponds to the Cornell geometry, which means that the incident ion beam, the exit beam and the rotation axis are in the same plane. The angle between the incident and exit beams is 9°, i.e. the scattering angle of the detected ions is 171°. A 2.0 MeV He^+ beam with a spot size of 800 μm was used.

For the data analysis RUMP code was applied [144]. The RUMP code is a computer simulation program which generates theoretical spectra for thick or thin targets bombarded by light projectiles with incident energies up to 4 MeV. Samples are considered to be made of up a finite number of layers, each with uniform composition. A hypothetical initial description of the sample is used, and then iterative simulations of the spectrum and correction of the sample description are performed, searching for the best simulation.

As an example, in Fig. 3.13 a RBS spectrum of Si(001) after low-energy Kr^+ bombardment is shown.

For PIXE a 2.0 MeV H^+ beam with an 800 μm spot size was used. The RÖNTEC Si(Li) detector has active area of 9.6 mm^2, with an energy resolution $\Delta E = 138$ eV at 5.9 keV. The data was analyzed using the computer simulation program GeoPIXE II [145], which uses the Dynamic Analysis method [146] for real-time PIXE spectra interpretation. Dynamic Analysis is a method to separate pure elemental spectral components in a PIXE spectrum to project pure elemental quantitative images.
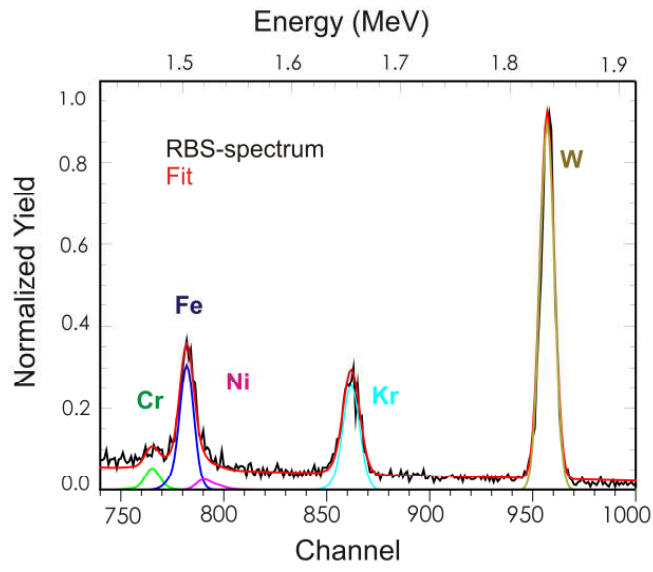
**Figure 3.13.** RBS spectrum of Si(001) after sputtering with 2000 eV Kr^+.

Chapter 4
Topography evolution under different erosion parameters

As it was mentioned in chapter 1, the aim of this work was to investigate the pattern formation on silicon surfaces by low-energy ion beam erosion; in particular, to study the effect of different experimental parameters in the topography evolution. A better knowledge about the role of the many parameters involved in the pattern formation would facilitate the control and tuning of the nanostructures produced by ion erosion. Among all the experimental parameters involved, the incidence angle of the ions is critical and it will be first addressed. It will be shown that the incident angle determines the type of pattern that evolves on the substrate. The low angle region (incidence angle up to ~ 45°) and the high angle region (~ 65° to 85°) will be discussed separately. In addition, the dependence on different operational parameters (fluence, acceleration voltage, discharge voltage, grid distance, and operation time) will be analyzed.

The results presented in this chapter and chapter 5 correspond to Si(001) samples irradiated with Kr^+. Commercially available epi-polished p-type Si(001) pieces were used. The resistivity was in the range of 0.01-0.02 Ω cm and the root-mean-square (RMS) roughness was lower than 0.2 nm. If not otherwise specified, the current density j_{ion} was 300 μA cm^{-2}, corresponding to an ion flux J of 1.87×10^{15} cm^{-2}s^{-1}, the discharge voltage U_{dis} was 100 V and the samples were irradiated without rotation.

4.1. Overview of the effect of ion beam incidence angle

The angle of incidence at which the ions collide with the substrate is a critical parameter that affects the topography evolution. Its influence is related to the fact that it has a strong impact in the sputtering yield, the distribution of the deposited energy, and in the occurrence of preferential sputtering of certain regions, e.g. shadowing effect at grazing angles. As it was already mentioned in section 3.1, the ions within the broad beam do not have perfectly parallel trajectories, but they show a certain angular distribution that depends on different operational parameters. Here, instead of the ion incidence angle, the *ion beam incidence angle α* is considered, which is defined as the angle between the source axis and the substrate normal. It should be always kept in mind, however, that the beam presents a certain divergence, which can be higher than 7°, as it was also shown in section 3.1. In Fig. 4.1 an overview of the different topographies formed on
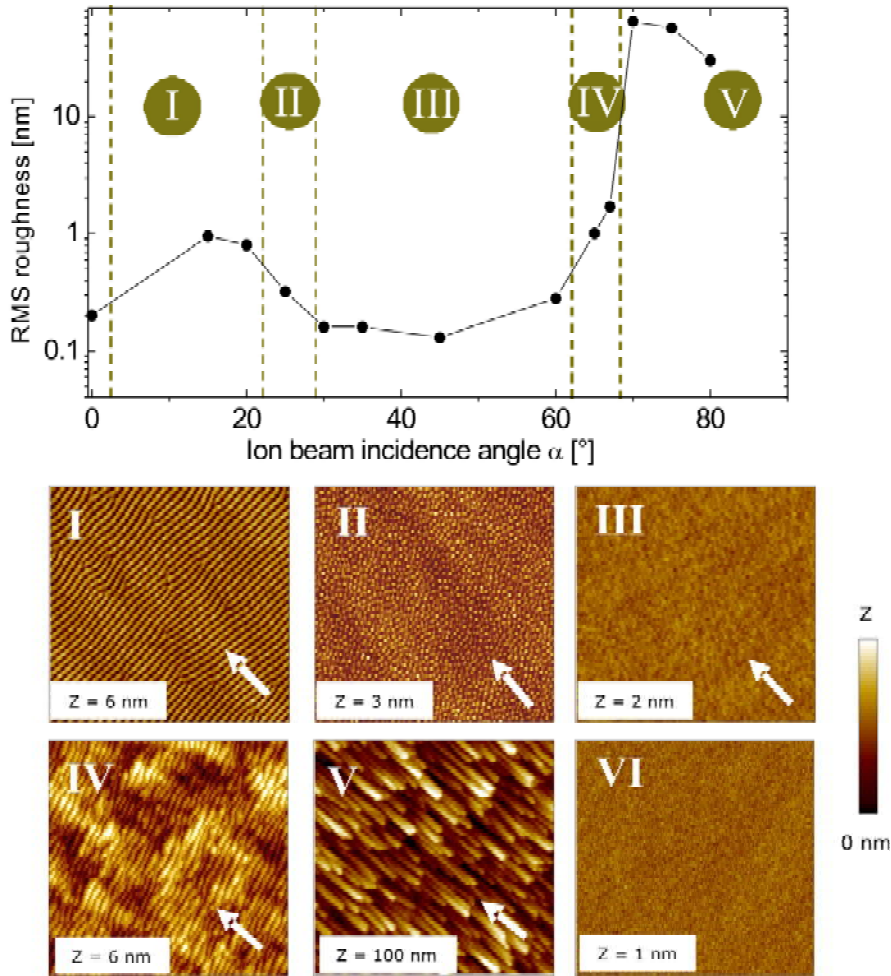
Figure 4.1. Surface roughness vs. ion beam incidence angle for silicon bombarded with Kr$^+$ ions, E_{ion} = 2000 eV, U_{acc} = - 1000 V, Φ = 6.7 × 10^{18} cm^{-2}. AFM images of the different topographies (examples): I: ripples at near normal incidence, II: dots, III: smooth surface, IV: ripples at high incidence angles, V: columnar structures, and VI: non-irradiated sample. The size of the images is 2 μm × 2 μm and the resolution 512 × 512 pixels. The white arrows indicate the projection of the ion beam on the surface.

silicon by erosion with 2000 eV Kr$^+$, with U_{acc} = -1000 V, and a fluence Φ = 6.7 × 10^{18} cm^{-2} is presented. As it can be observed from Fig. 4.1, different topographies evolved on silicon under the given conditions depending on the ion beam incidence angle. At normal incidence low-amplitude hillocks without regular distribution were formed (not shown here). At near normal incidence, i.e. $\alpha \sim 5° - 22°$, ripples were generated (Fig. 4.1 I). These ripples show a high regularity and by variation of the ion energy E_{ion} from ~ 750 eV to 2000 eV the wavelength and the amplitude can, in general, be tuned between ~ 30 to 70 nm and up to ~ 8 nm, respectively.

At $\alpha \sim 45°$ the surface smoothened (Fig. 4.1 III); the RMS roughness decreased to 0.15 nm. For comparison, the AFM image of a sample before irradiation is shown in Fig. 4.1 VI; the RMS roughness is 0.06 nm. The smoothing between $\alpha \sim 35°$ - $60°$ was observed to be nearly independent of E_{ion} and ion species and it has been also intensively studied [47, 67]. The dot-like structures shown in Fig. 4.1.II usually evolve only in a narrow window of operating conditions and in some cases a mixture of dots and ripples is observed. At higher angles ripples and columnar structures were formed (Fig. 4.1 IV and V). The direction of the anisotropic nanostructures is determined by the direction of the ion beam. The ripples (Fig. 4.1 I and IV) are perpendicular to the projection of the beam on the surface while the columnar structures formed at grazing angles (Fig. 4.1 V) are parallel.

4.2. Low incidence angles

In this sub-section the topographies that evolve on silicon at ion beam incidence angles $\alpha < 45°$ are analyzed.

4.2.1. Transition from ripples to smooth surface

The different topographies that evolved on silicon after ion erosion at different ion beam incidence angles under the given conditions were shown in Fig. 4.1. The lines that separate the regions of the different topographies in the plot represent only a guide to the eye, but they do not indicate abrupt changes in the topography. The topography changes gradually, i.e. the transitions between the different types of features are continuous. In Fig. 4.2 the transition from ripples to smooth surface (from structure I to III in Fig. 4.1) due to irradiation with Kr$^+$, E_{ion} = 2000 eV, U_{acc} = -1000 V, when α was increased from 20° to 30° is presented. At ion beam incidence angles up to 22° ripples were formed (Fig. 4.2a and 4.2b). When α increased, the amplitude of the features on the surface, and therefore the RMS roughness, decreased continuously. The ripples turned discontinuous, and at $\alpha = 25°$ dots together with ripples are observed (Fig. 4.2c). Dots with very low amplitude evolved at $\alpha = 26°$ (Fig. 4.2d) and finally at higher α the surface remained smooth (Fig. 4.2e and 4.2f). The ripples are oriented perpendicular to the ion beam, and when they turned into dots, the orientation, up to some degree, remained. It was already observed that this transition is highly sensitive to the acceleration voltage U_{acc} [32, 50], which affects mainly the divergence of the beam.
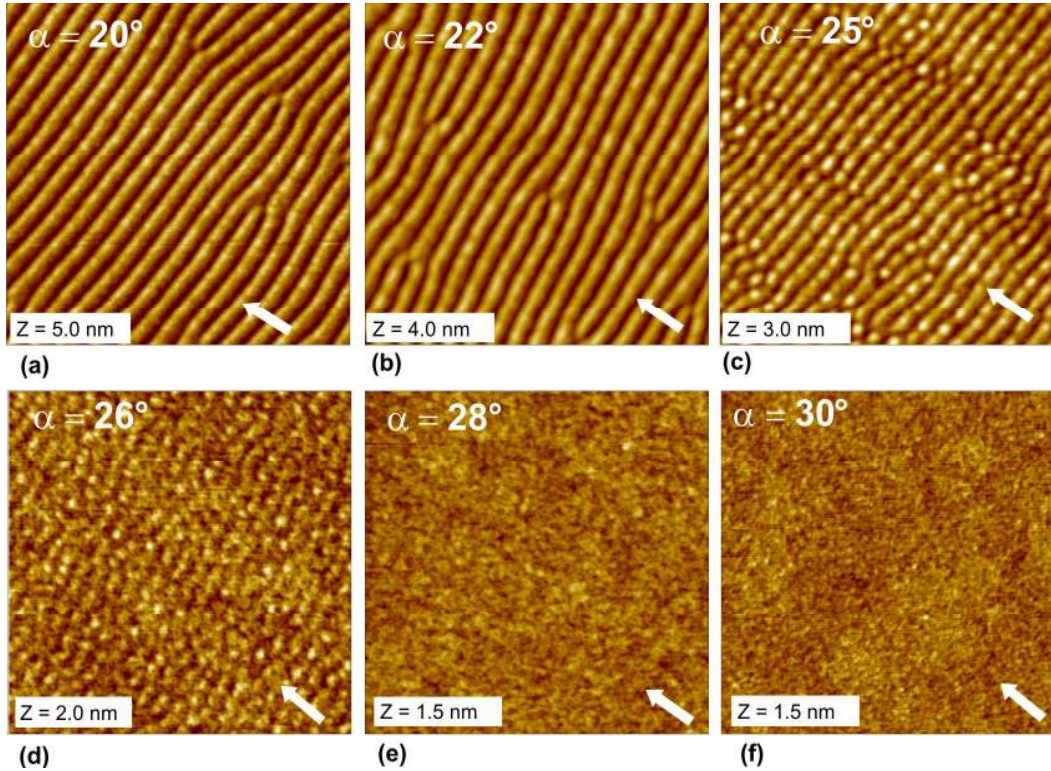
Figure 4.2. AFM images of Si samples bombarded with Kr$^+$ ions, E_{ion} = 2000 eV, U_{acc} = -1000 V, Φ = 6.7 × 10^{18} cm^{-2}, at α = 20° - 30°. The images are 1 μm × 1 μm and the resolution 512 × 512 pixels. The RMS roughness is (a): 0.9 nm, (b): 0.7 nm, (c): 0.5 nm, (d): 0.2 nm, (e): ≤ 0.2 nm, and (f): ≤ 0.2 nm. The white arrows indicate the projection of the ion beam on the surface.

From the hypothesis that the divergence of the ion beam plays an important role in the pattern formation, the effects of parameters that determine the angular distribution of the ions within the beam were studied. Next, the influence of some of these operational parameters in the transition is shown.

4.2.1.1. Acceleration voltage

In section 3.1, it was shown that the acceleration voltage U_{acc} is an additional important operational parameter. The acceleration voltage is the potential applied at the second extraction grid and it determines the angular distribution of the ions within the beam. U_{acc} can vary from -10 V to -1000 V. U_{acc} = -1000 V, which was used for the results presented in Fig. 4.1, corresponds to the highest divergence (see section 3.1). The influence of U_{acc}, and therefore the beam divergence, in the topography evolution due to ion irradiation in the range of ion beam incidence angles where the transition (ripples to smooth surface) occurs was analyzed. The results are summarized in Fig. 4.3, and
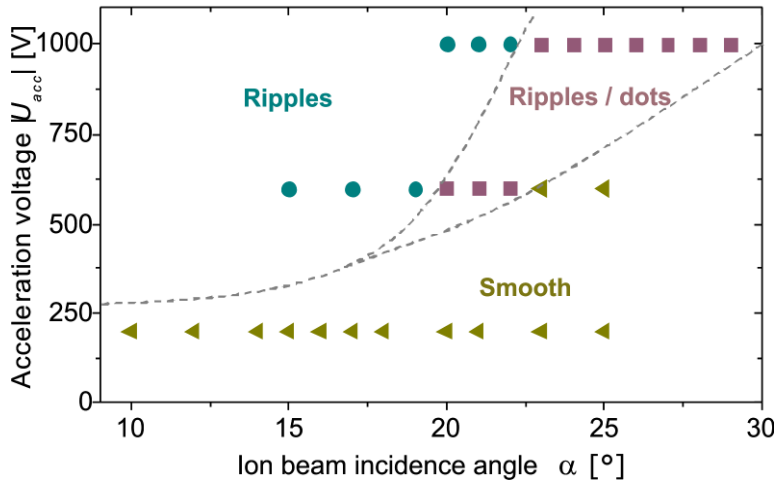
Figure 4.3. Topography diagram for different U_{acc} and the α range where the transition ripples to smooth surface takes place. The samples were irradiated with 2000 eV Kr$^+$ and $\Phi = 6.7 \times 10^{18}$ cm^{-2}.

correspond to samples irradiated with 2000 eV Kr$^+$, with $\Phi = 6.7 \times 10^{18}$ cm^{-2}. The ion beam incidence angle at which the transition takes place was shifted for different U_{acc}. With $U_{acc} = -1000$ V ripples were formed at $\alpha \leq 23°$, with $U_{acc} = -600$ V only at $\alpha \leq 19°$, and with $U_{acc} = -200$ V the surface remained smooth. These results seem to corroborate the importance of the divergence of the beam on the topography evolution.

4.2.1.2. Discharge voltage

The discharge voltage U_{dis} controls the acceleration of the emitted electrons in the filament sheath [101], which in turn affects the plasma sheath and position and plasma density. A further effect of the increasing discharge voltage is the increasing content of double charged ions in the plasma and the beam. As the plasma properties are affected by U_{dis}, also the divergence of the beam is expected to be modified.

The topography diagram presented in Fig. 4.4 for silicon surfaces bombarded with 2000 eV Kr$^+$, $U_{acc} = -1000$ V at different α and U_{dis}, shows that the ion beam incidence angle at which the transition begins was shifted to higher angles as U_{dis} decreased. With $U_{dis} = 140$ V, ripples were stable at $\alpha \leq 33°$ and smoothing took place at $\alpha \geq 38°$, while with $U_{dis} = 50$ V the ripples were formed in a wider range of incidence angles ($\alpha \leq 38°$) and smoothing was observed at $\alpha \geq 43°$.

4.2.1.3. Grid distance

In relation to the geometry of the extraction system, samples were irradiated using two different distances between the grids. It was observed that the change of the grid distance also led to a shift on the angle at which the transition from ripple to smooth
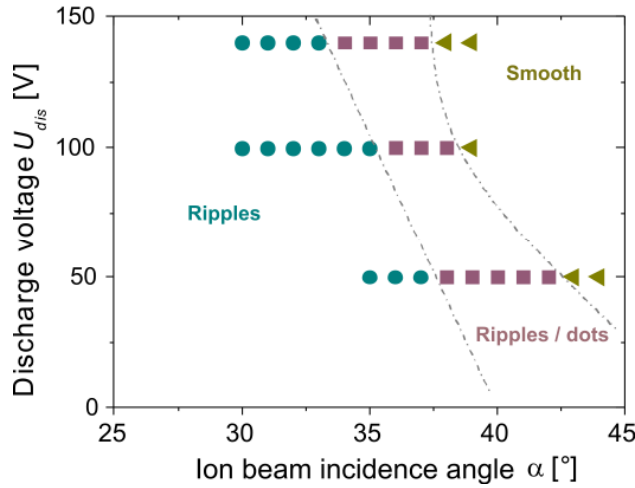
Figure 4.4. Topography diagram for different U_{dis} and the α range where the transition ripples to smooth surface takes place. The samples were irradiated with 2000 eV Kr$^+$, with U_{acc} = -1000 V and Φ = 6.7 × 10^{18} cm^{-2}.
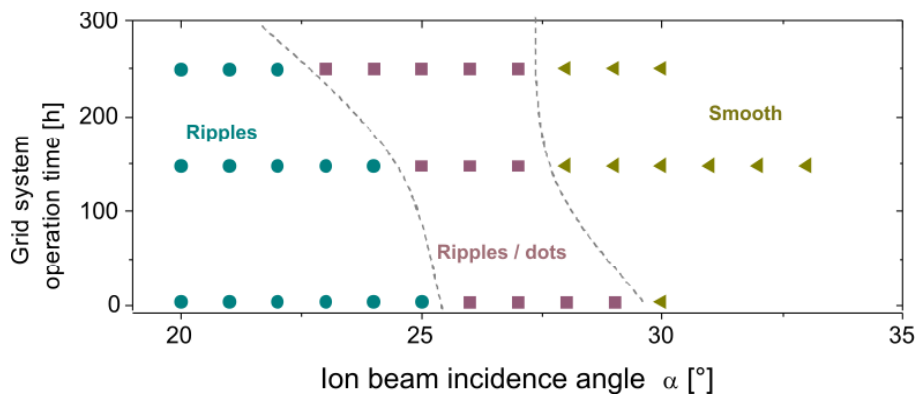
surface takes place. The samples were irradiated with 2000 eV Kr$^+$, U_{acc} = -1000 V, and Φ = 6.7 × 10^{18} cm^{-2}. For distances of 1 mm and 2 mm the ripples were stable up to an ion beam incidence angle α of 36° and 26°, respectively.

4.2.1.4. Operation time

In addition, an effect of the ion source operation time on the topography evolution was observed. It is known that some changes in the geometry of the extraction system occur with the time. The collisions of the ions with the acceleration grid result in the erosion of the grid. In regard to the pattern transition, the evolving topography using a new grid system and after 250 hours of use was compared. The ion beam incidence angle at which the transition takes place was shifted in four degrees (Fig. 4.5). It was observed that with the operation time the range of incidence angles at which the ripples are stable was reduced. After irradiation with 2000 eV Kr$^+$, with U_{acc} = -1000 V, and Φ = 6.7 × 10^{18} cm^{-2}, ripples were formed at $\alpha \leq 26°$ for the new grid system and at $\alpha \leq 22°$ after 250 h operation.

4.2.1.5. Correlation between operational parameters and beam divergence

As it was already mentioned in section 3.1, the angular distribution of the ions leaving the extraction system is determined by the shape and position of the plasma sheath near the screen grid holes. The plasma sheath properties are in turn controlled by the plasma properties, the extraction potentials and the grid geometry [105]. The parameters analyzed in subsections 4.2.1.1 to 4.2.1.4 are related to the extraction system potentials (U_{acc}), the plasma properties (U_{dis}) and the grid system geometry (operation time and

Figure 4.5. Topography diagram for different grid operation times and the α range where the transition ripples to smooth surface takes place. The samples were irradiated with 2000 eV Kr$^+$, with $U_{acc} = -1000$ V and $\Phi = 6.7 \times 10^{18}$ cm^{-2}.

grid distance). Therefore, they affect the angular distribution of the ions within the beam. As it was shown, and in agreement to the hypothesis of the importance of the beam divergence, these parameters affect also the angle at which the transition ripples-smooth surface takes place. The way the grid distance and U_{dis} affect the divergence of the beam is complex and not easily predicted. However, it is known that when $|U_{acc}|$ increases, the ion beam divergence also increases and when the operation time increases the divergence angle becomes smaller due to the enlargement of the grid apertures.

According to the experimental observations presented here, the formation of ripples and the smoothening are associated with a larger and lower divergence, respectively. In chapter 5 the topography evolution dependence on the divergence angle will be further investigated.

4.2.2. Temporal evolution of ripples at near normal incidence

In Fig. 4.6 AFM images and PSD diagrams of silicon surfaces irradiated with Kr$^+$, at $\alpha = 35°$, $E_{ion} = 2000$ eV, $U_{acc} = -1000$ V with different fluences are presented. By visual observation of the AFM topography images, it is possible to recognize that with the fluence the regularity of the ripples increased. Also the PSD diagrams show the increase of the regularity; i.e. the peak corresponding to the ripples becomes narrower for higher fluences, which indicates that the correlation length increases with the fluence (see subsection 3.2.1). The roughness increased in the first minutes and then it saturated. The position of the peak in the PSD diagrams does not change for the different fluences, which indicates that the wavelength of the ripples remained approximately constant.
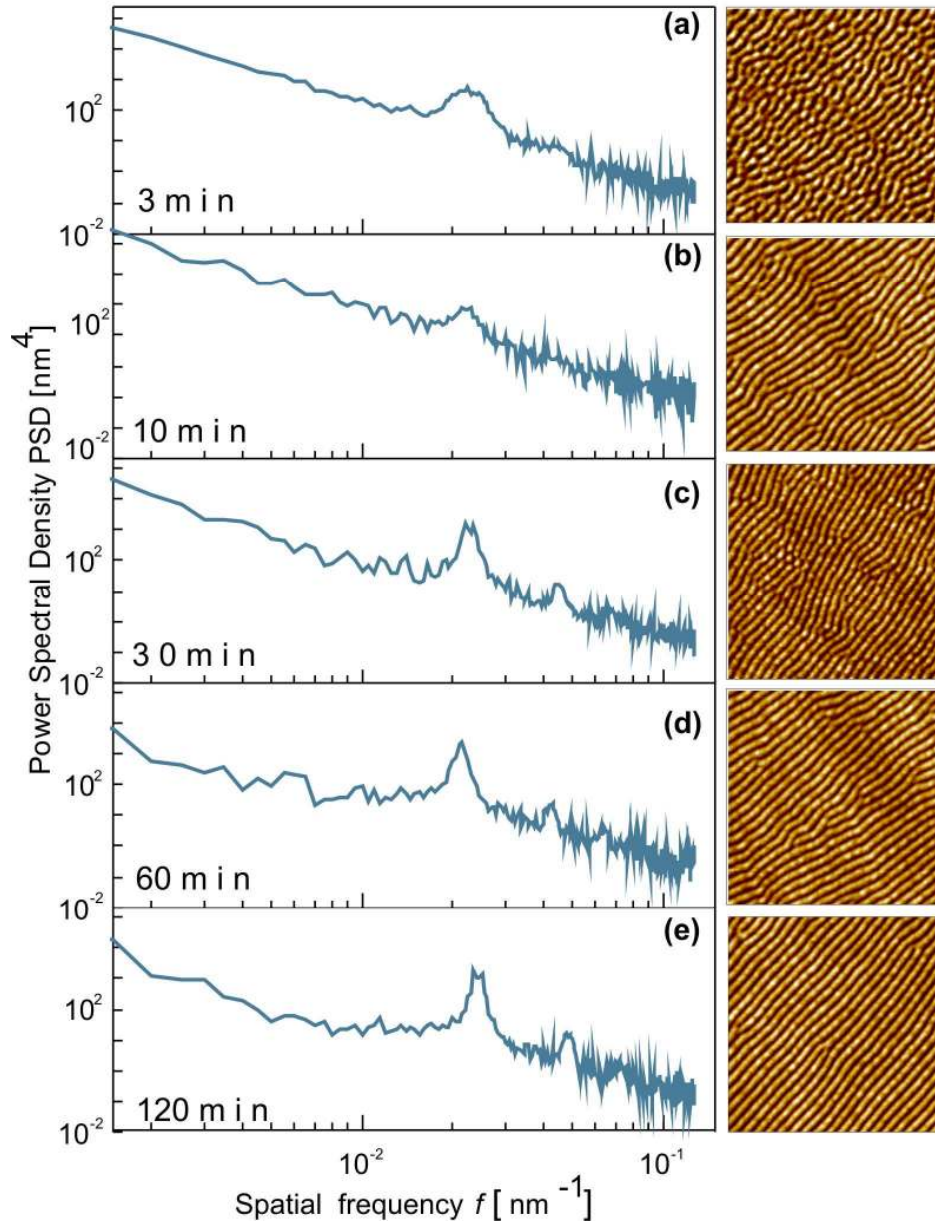
Fig. 4.6. Temporal evolution of ripples at $\alpha = 35°$. Power spectral density diagrams and AFM images of Si surfaces after irradiation with Kr^+, $E_{ion} = 2000$ eV, $U_{acc} = -1000$ V, $\alpha = 35°$, with fluence $\Phi =$ (a): 3.4×10^{17} cm^2 (3 min), (b): 1.1×10^{18} cm^2 (10 min), (c): 3.4×10^{18} cm^2 (30 min), (d): 6.7×10^{18} cm^2 (60 min), and (e): 1.3×10^{19} cm^2 (120 min). The AFM images are 2 μm × 2 μm. The vertical scale is (a): 2.5 nm, (b): 3.0 nm, (c): 3.5 nm, (d): 4.0 nm, and (e): 4.0 nm. The RMS roughness is (a): 0.5 nm, (b): 0.6 nm, (c): 0.7 nm, (d): 0.7 nm, and (e): 0.8 nm. The noise observed at high frequencies reflects unfavorable ambient conditions during measurement.

The temporal evolution was analyzed at different incidence angles ($\alpha = 5°$, $10°$, $20°$-$40°$) and the effect was found to be the same presented in this example.

4.2.3. Ion energy vs. ripples orientation

The topography that evolved on silicon after irradiation with Kr$^+$, at $\alpha = 20°$, $U_{acc} = $ -1000 V, and different E_{ion} (300 eV to 2000 eV) is presented in Fig. 4.7. With $E_{ion} = 2000$ eV (Fig. 4.7a) perpendicular-mode ripples are the dominant features observed on the surface. Scanning a larger surface area (not shown here), it is possible to see that waves parallel to the ion beam direction with large period and small amplitude are also present. With decreasing E_{ion} these parallel-mode waves or ripples are more clearly observed and they coexist with the perpendicular-mode ripples. With $E_{ion} = 300$ eV the parallel-mode ripples dominate the surface topography (Fig. 4.7e). For the entire ion energy range analyzed, it is possible to see from the AFM images that the wavelength λ and amplitude of the perpendicular-mode ripples are smaller than that of the parallel-mode undulations.

In Fig. 4.8a the corresponding power spectral density (PSD) diagrams are shown. The peak corresponding to the perpendicular-mode ripples, indicated with open arrow in Fig. 4.8a, is easily identified for most topographies. Its frequency provides the wavelength of the ripples. However, the parallel-mode ripples peak, which is pointed out with close arrow, is broader since the parallel-mode ripples are not so regular. Thus, to quantify the dimensions of the parallel-ripples the method described in subsection 3.2.1 was utilized, using the AFM images from the amplitude error signal (see subsection 3.2.1 for definitions and methodology description). In Fig. 4.8b the evolution of the wavelength with ion energy for both types of ripples is shown. The wavelength of the perpendicular-mode ripples increased with E_{ion}. The same effect is observed for the parallel-mode ripples. However, it should be mentioned here that the wavelength is difficult to be determined for $E_{ion} > 1000$ eV because of the decreasing amplitude. According to the BH model [37], described in section 2.3, the orientation of the ripples is determined by the direction of the beam, and at incidence angles below the critical angle α_c (see subsection 2.3.1) the ripples are perpendicular to the ion beam projection on the surface. The results presented here seem to disagree with the orientation prediction. However, the requirements of the BH model are not entirely fulfilled, thus leading to different results. This issue will be further discussed in chapter 5.
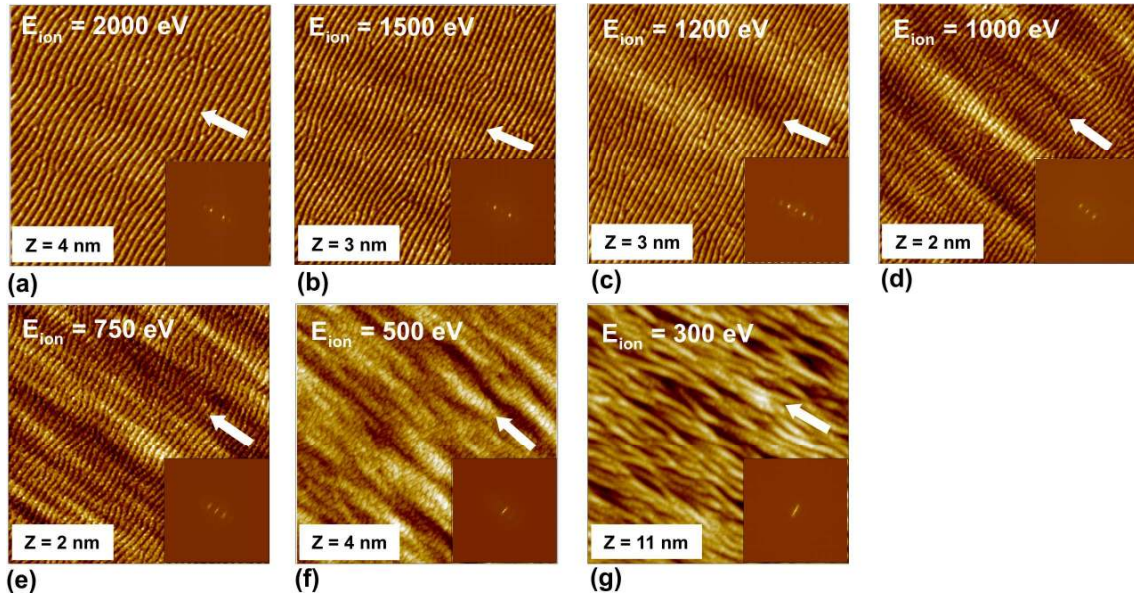
Figure 4.7. AFM images of samples after irradiation with Kr^+, $\Phi = 6.7 \times 10^{18}\,cm^{-2}$, $U_{acc} = -1000$ V, $\alpha = 20°$ and E_{ion} from 300 eV to 2000 eV. All the images are 2 µm × 2 µm and have a resolution of 512 × 512 pixels. The RMS roughness is (a): 0.8 nm, (b): 0.6 nm, (c): 0.7 nm, (d): 0.4 nm, (e): 0.4 nm, (f): 0.5 nm, and (g): 1.9 nm. The white arrows indicate the projection of the ion beam on the surface.
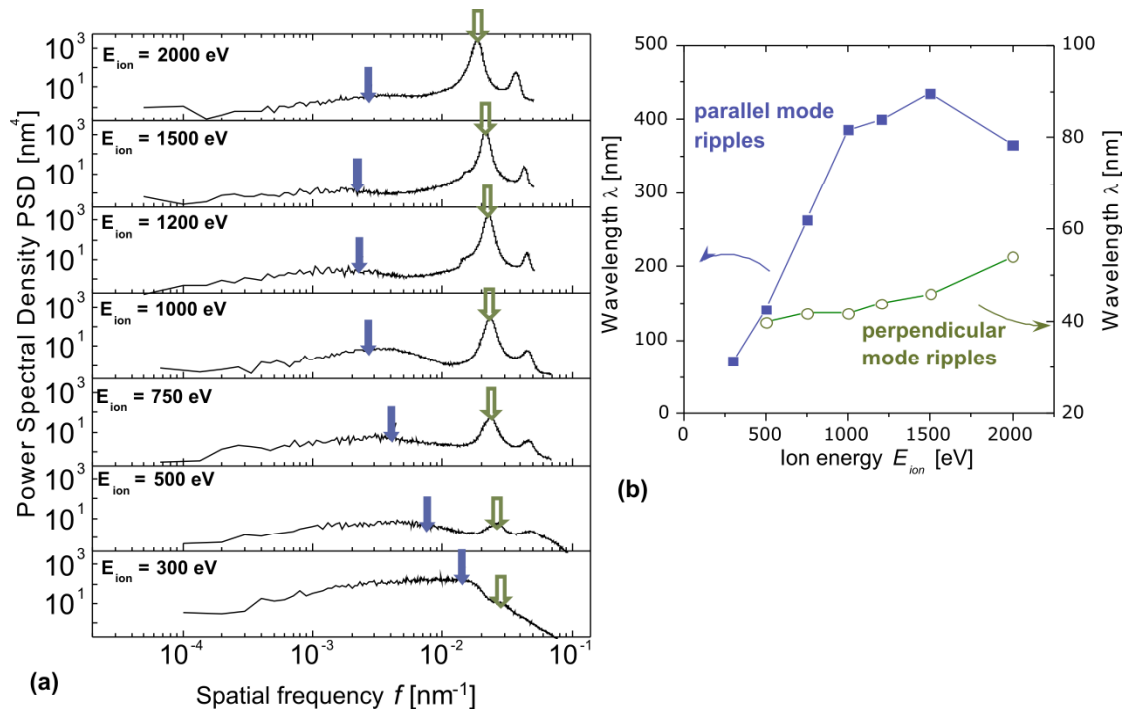
Figure 4.8. (a): Power spectral density diagrams of silicon surfaces after irradiation with Kr^+, $\Phi = 6.7 \times 10^{18}\,cm^{-2}$, $U_{acc} = -1000$ V, $\alpha = 20°$ for different E_{ion}. The close and open arrows indicate the position of the peaks of the parallel- and perpendicular-mode ripples, respectively. (b): Ion energy dependence of the ripples wavelength.

4.3. High incidence angles

In this subsection the topography evolution by ion erosion at $\alpha \geq 65°$ will be analyzed.

4.3.1. Overview of the effect of α and E_{ion} at high incidence angles

As it was shown in section 4.1, at ion beam incidence angles $\alpha \geq 65°$ perpendicular-mode ripples are formed and they turn into columnar structures oriented parallel to the ion beam when α increases. In Fig. 4.9 a topography diagram and AFM images of the different topographies that evolved due to bombardment with Kr^+ at $\alpha = 65°$ - $85°$ with different E_{ion} (300 eV – 2000 eV) are presented. It is observed that perpendicular-mode ripples evolved at $\alpha = 65°$ with high E_{ion} and that increasing α and decreasing E_{ion} features parallel to the ion beam projection on the surface were formed. The presence of vertical or undercut edges on the surface, which may be the case in columnar-type topographies, could lead to AFM images with artifacts, since the images are the result of the tip-surface convolution. Thus, additionally to AFM, SEM was used to characterize the topography after ion erosion.

Top view and tilted SEM images of the different parallel-type structures are shown in Fig. 4.10. The images correspond to the type of features presented in the topography diagram in Fig. 4.9 as II (Fig. 4.10a and 4.10b), III (Fig. 4.10c and 4.10d), IV (Fig. 4.10e and 4.10f), and V (Fig. 4.10g and 4.10h). The images on the left side (Fig. 4.10a, 4.10c, 4.10e, and 4.10g) were performed with a sample tilt angle of 55°, and the images on the right (Fig. 4.10b, 4.10d, 4.10f, and 4.10h) show top views of the samples.

As it is observed, the columnar structures formed at high E_{ion} and at α near 70° (Fig. 4.10a and 4.10b) are separated from each other; they do not cover completely the surface. In the SEM images it is possible to see that they present two different facets, i.e. the upstream and downstream sides. The upstream side is that facing the ion source, i.e. against the direction of the ions, while the downstream side faces the direction of the ion beam. On the downstream side, smaller features elongated in the direction of the ion beam direction are observed. The columnar features resemble the structures reported by Carter et al. [5] after bombardment of Si(001) with 40 keV Ar^+. They described these features as *stacked and tilted cylindrical segments,* whose tilt angle matched the ion beam incidence angle.
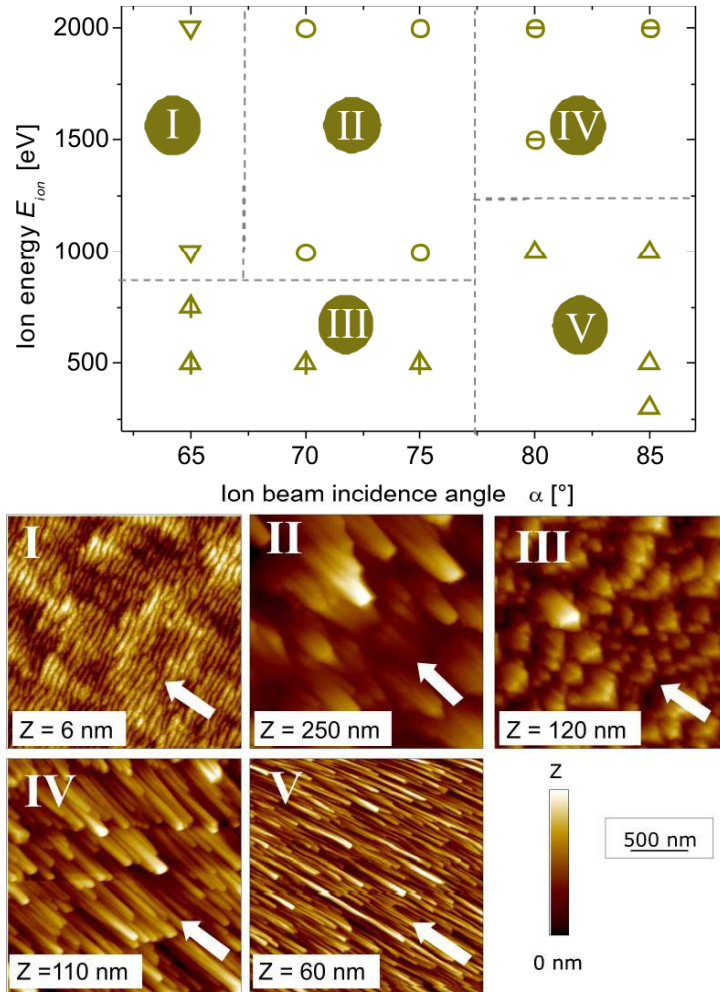
Figure 4.9. Topography diagram for different E_{ion} and α for silicon bombarded with Kr$^+$, with U_{acc} = -1000 V, Φ = 6.7×10^{18} cm^{-2}. The lines in the plot represent only a guide to the eye. AFM images of the different topographies (examples): I: perpendicular mode ripples, II, III, IV, V: columnar structures parallel to the ion beam projection on the surface with different dimensions. The RMS roughness is (I): 1 nm, (II): 75 nm, (III): 25 nm, (IV): 19 nm, and (V): 11 nm. The white arrows indicate the projection of the ion beam on the surface.

At different α and $E_{ion,}$ the columnar structures show different density on the surface, length to width ratio and amplitude. It seems that at higher α, the density and the length to width ratio increased. For example, the features formed with high E_{ion} and at α near 70° (Fig. 4.10a and 4.10b) have a width between 200 nm - 500 nm and a length between ~ 600 nm - 800 nm, while the width and length of those formed at lower E_{ion} and α between 80° and 85° (Fig. 4.10g and 4.10h) range between ~ 50 nm – 70 nm and ~ 1000 nm – 1200 nm, respectively. This behaviour is consistent with the results from Carter et al. [5], who observed that the length to radius ratio of the cylindrical segments increased with α.
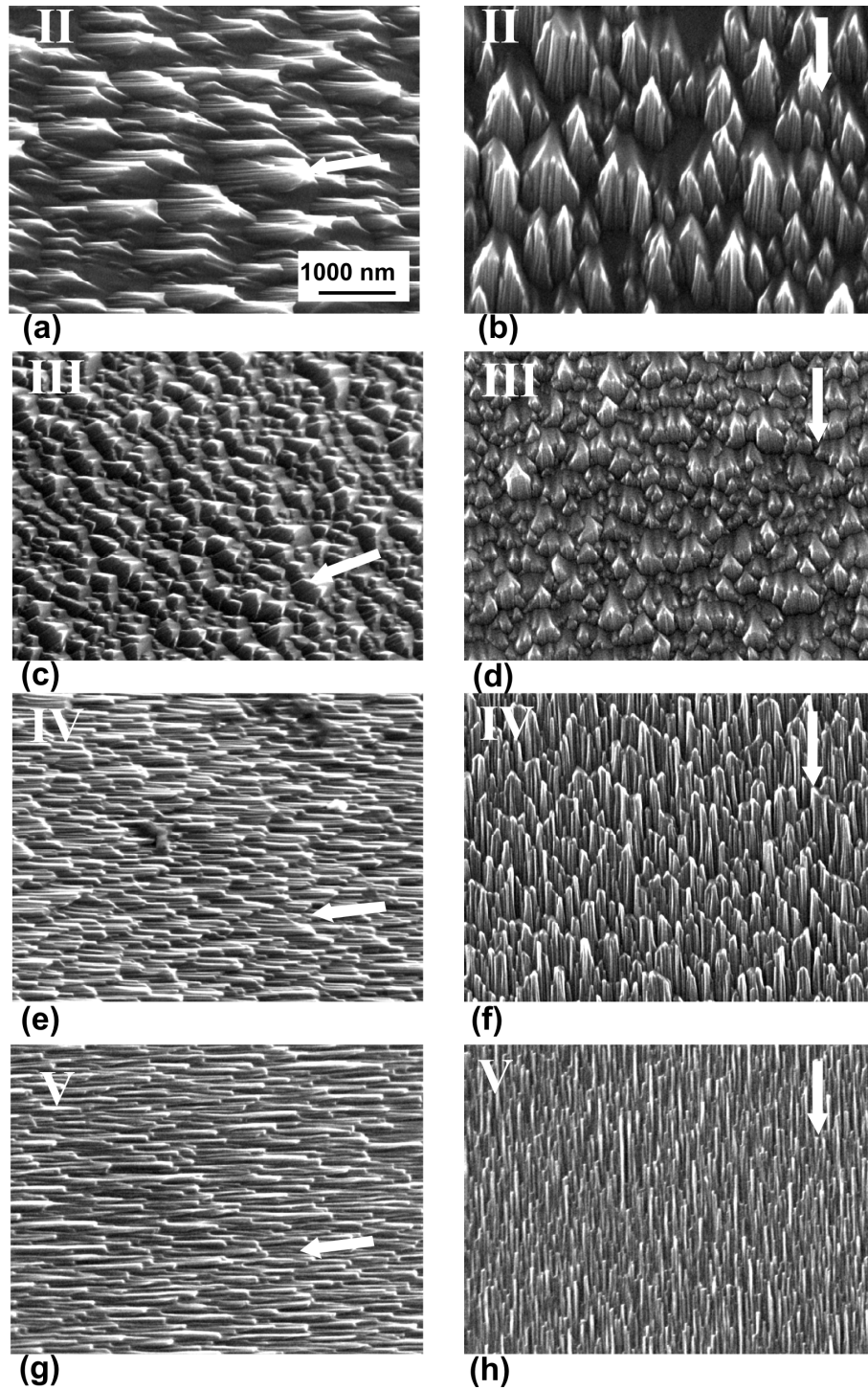
Figure 4.10. SEM images from the samples presented in Fig. 4.9 and indicated as II, III, IV and V. The white arrows indicate the ion beam direction. The images on the left side (a, c, e, and g) were measured with a tilt angle of 55°. The images on the right (b, d, f, and h) correspond to top view.

The same tendency is observed here as E_{ion} decreased. With respect to the amplitude, it is maximal at high E_{ion} and α near 70°.

4.3.2. Transition at $\alpha = 65°$ - $70°$

As well as the transition from ripples to smooth surface at near normal incidence, the transition between topographies at high angle is not abrupt, but continuous. The AFM images presented in Fig. 4.11 show the topography of samples after bombardment with Kr^+, $E_{ion} = 2000$ eV, $U_{acc} = -1000$ V when α is varied in one degree steps from $65°$ to $70°$. At ion beam incidence angles from $65°$ to $68°$, ripples perpendicular to the ion beam were formed, together with some undulations or waves that are parallel to the ion beam. A decrease of the wavelength λ of the perpendicular-mode ripples for increasing α is observed. This can be seen in the AFM images and was also determined from the PSD functions of the samples (not shown here). Also the perpendicular-mode ripples seem to be more regular when the samples were bombarded at higher α. At $\alpha = 69°$, isolated large amplitude protuberances, i.e. the columnar structures evolved (Fig. 4.11e). When α was increased by one degree, i.e. $\alpha = 70°$, the density of the columnar structures on the surface increased (Fig. 4.11 f).

In Fig. 4.12 SEM images of four of these topographies are presented. For structures with low amplitude, SEM is not the most appropriate imaging technique. Thus, the waves parallel to the ion beam formed at $\alpha = 65°$ are not distinguished (Fig. 4.12a). AFM, in this case, due to the type of features and their relatively low amplitude provides more reliable images of the topographies. At $\alpha = 66°$ the parallel-mode waves are already visible with SEM (Fig. 4.12b).

The columnar structures formed at $\alpha = 69°$ and $\alpha = 70°$ are clearly seen (Fig. 4.12c and 4.12d). As it was observed in Fig. 4.10a, they show specific facets, at the downstream and upstream sides and present features elongated in the beam direction on the downstream side. It is observed also how the density of these features on the surface increased when the ion beam incidence angle was increased from $69°$ to $70°$. To examine more in detail both faceted sides, height profiles in the direction of the ion beam were taken from the AFM images and are shown in Fig. 4.13. The corresponding sample was irradiated at $\alpha = 70°$, with 1000 eV Kr^+, $U_{acc} = -1000$ V, $\Phi = 6.7 \times 10^{18}$ cm^{-2}. According to the height profiles (Fig. 4.13b and 4.13c), the angles formed by the ion beam and the local surface normal at both sides are in the ranges of $\sim 84°$- $89°$ and $\sim 2°$- $10°$ for the downstream and upstream side, respectively.
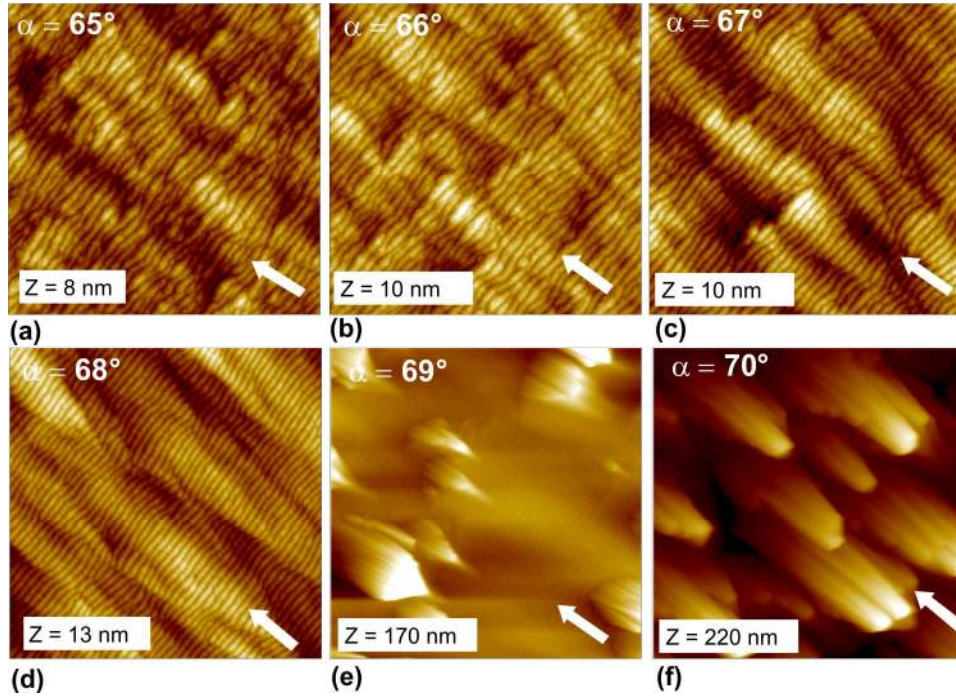
Figure 4.11. AFM images of samples after irradiation with Kr$^+$, $\Phi = 6.7 \times 10^{18}$ cm^{-2}, $E_{ion} = 2000$ eV, U$_{acc}$ = -1000 V, α = 65°-70°. All the images are 2 μm × 2 μm and have a resolution of 512 × 512 pixels. The RMS roughness is (a): 1.1 nm, (b): 1.3 nm, (c): 1.7 nm, (d): 2.0 nm , (e): 23 nm, and (f): 75 nm. The white arrows indicate the projection of the ion beam on the surface.
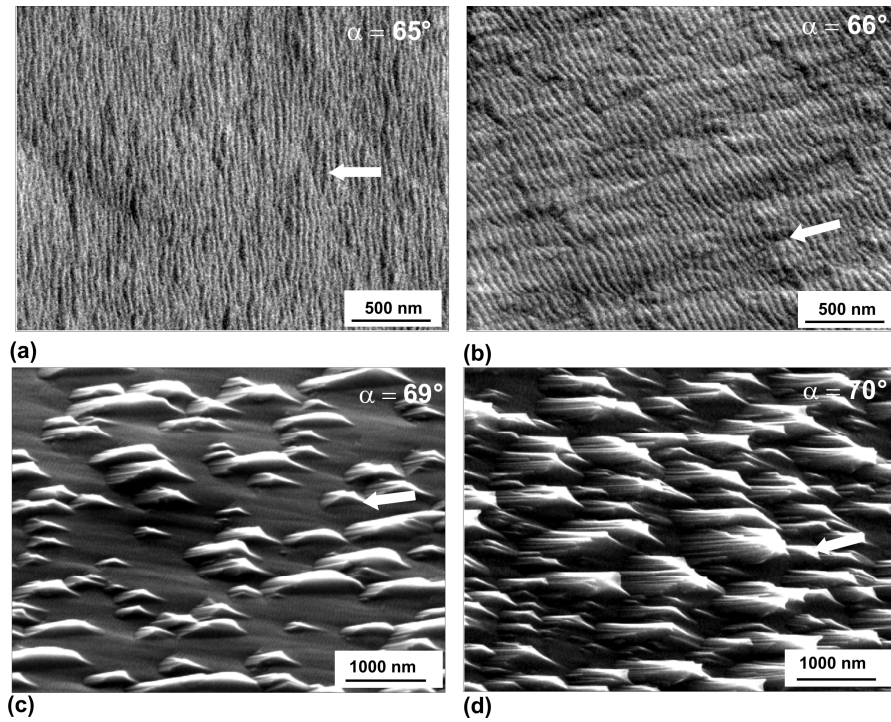
**Figure 4.12.** Secondary electron microscopy SEM images (tilt angle = 55°) of Si(001) surfaces after irradiation with Kr$^+$, $\Phi = 6.7 \times 10^{18}$ cm^{-2}, $E_{ion} = 2000$ eV, U_{acc} = -1000 V, α = 65° (a), 66° (b), 69° (c) and 70° (d). The white arrows indicate ion beam direction.

67

Since AFM may not be the most appropriate technique to characterize the topography in the presence of vertical or undercut edges, additionally, SEM and Focused Ion Beam (FIB) were combined to obtain a cross-sectional view of the same sample shown in Fig. 4.13. FIB was used to make a crater in the sample, preceded by deposition of a Pt layer. The crater was enlarged several times and each time SEM imaging was performed. Two SEM images with different magnification are shown in Fig. 4.14. The dark and light regions represent the silicon substrate and the Pt layer, respectively. The faceted features are clearly seen; however it was observed that the facets angles changed even for a single feature after enlarging slightly the crater by FIB.
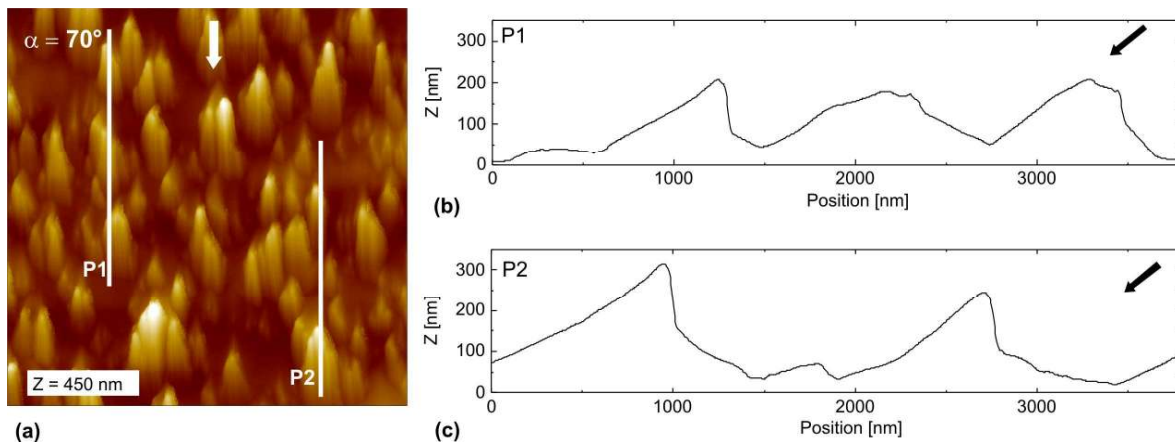
Figure 4.13. (a) AFM image of silicon after irradiation with Kr$^+$, $\Phi = 6.7 \times 10^{18}$ cm^{-2}, $E_{ion} = 1000$ eV, $U_{acc} = -1000$ V, $\alpha = 70°$. The image is 5 µm × 5 µm and it has a resolution of 1024 × 1024 pixels. The RMS roughness is 56 nm. (b), (c): Height profiles, corresponding to the white lines in (a). The arrows indicate the ion beam direction.
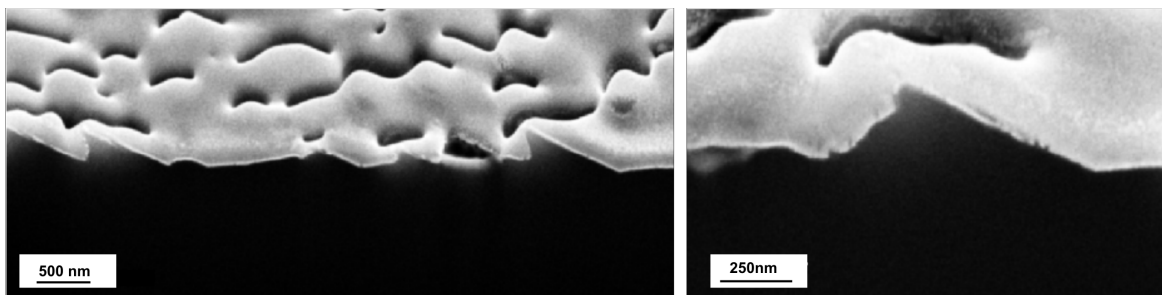
Figure 4.14. SEM cross sectional view (tilt angle = 54°) of silicon after irradiation with Kr$^+$, $\Phi = 6.7 \times 10^{18}$ cm^{-2}, $E_{ion} = 1000$ eV, $U_{acc} = -1000$ V, $\alpha = 70°$.

68
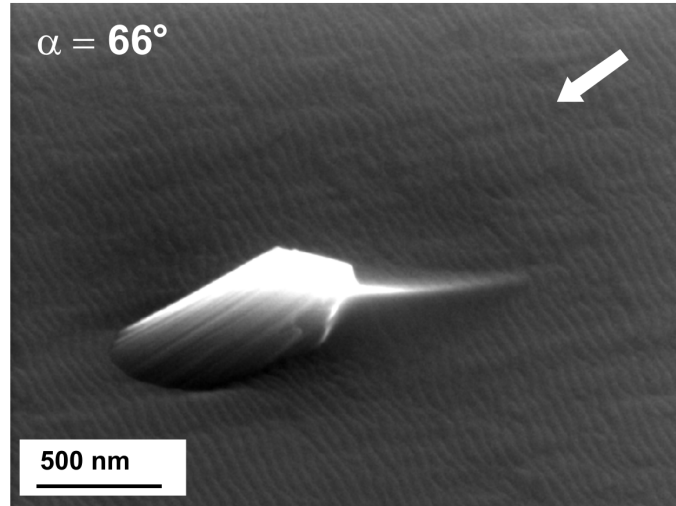
Figure 4.15. SEM image (tilt angle = 55°) of silicon after irradiation with Kr$^+$, $\Phi = 6.7 \times 10^{18}\,\text{cm}^{-2}$, $E_{ion} = 2000$ eV, $U_{acc} = -1000$ V, $\alpha = 66°$. The white arrow indicates the projection of the ion beam on the surface.

In order to have a better insight of the morphology of these features, in Fig. 4.15 a SEM image of one of the isolated protuberances formed at $\alpha = 66°$ is shown. It is possible to distinguish more in detail the different sides of the feature. The features oriented parallel to the beam direction on the downstream side are clearly observed. The side facing upstream looks different; it appears as a narrow elevation parallel to the ion beam whose height decreases continuously to left and right. The whole side is covered by the perpendicular-mode ripples that are present in the plane substrate. Due to the shape of the upstream facet, the height profiles extracted from the AFM images and the profiles observed in the cross sectional view of the sample are going to change depending on the exact position at which the cut is done. This is shown in Fig. 4.16; here five height profiles from a single feature of the sample from Fig. 4.13 and 4.14 are presented. These profiles were extracted from the AFM image (Fig. 4.16a) at positions very close to each other. It is possible to see how the height profile of a single protuberance changes from the centre to one of its sides. The angle formed by the ion beam and the downstream surface normal does not change significantly with the position; for this feature it ranges between ~ 85° - 87°. However, the angle from the upstream side goes from ~ 0° at the centre of the feature to ~ 40° at ~ 150 nm from the centre.

Taking into consideration only the angle formed by the ion beam and the faces at the center of the features, i.e. ~ 0° and ~ 90° for downstream and upstream sides, respectively, the facets angles would agree with the most stable facets predicted by

Nobes et al. [147]. They studied the ion erosion of amorphous materials and developed a theory for the topography evolution with the angle or gradient dependent sputtering as dominating mechanism. According to their model, the temporal evolution of the surface slope is given by:

$$\frac{\partial}{\partial t}\left(\frac{\partial y}{\partial x}\right) = -\frac{J}{N}\frac{dY(\theta)}{dx} = -\frac{J}{N}\frac{dY(\theta)}{d\theta}\frac{d\theta}{dx} \qquad (4.1)$$

where J is the ion flux, N the number of substrate atoms per volume unit, Y the sputtering yield, θ the local ion incidence angle.

With respect to the ion incidence angle dependence of the sputtering yield, it is observed that Y increases with increasing ion incidence angle due to the increase of the deposited energy, up to a certain angle, θ_p for which the sputter yield is maximal an it is usually between 65°-85°. At higher angles it decreases due to the increase of the amount of reflected ions and the decrease of the depth travelled by recoil atoms, and it is close to 0 at 90°. The ion incidence angle dependence of Y is characteristic of the ion – substrate combination and ion energy. The ion incidence angle dependence of the sputtering yield of silicon bombarded with 2000 eV Kr$^+$ is shown in Fig. 4.17. The sputtering yield values were calculated using TRIM.SP code [148].

(a)   (b)
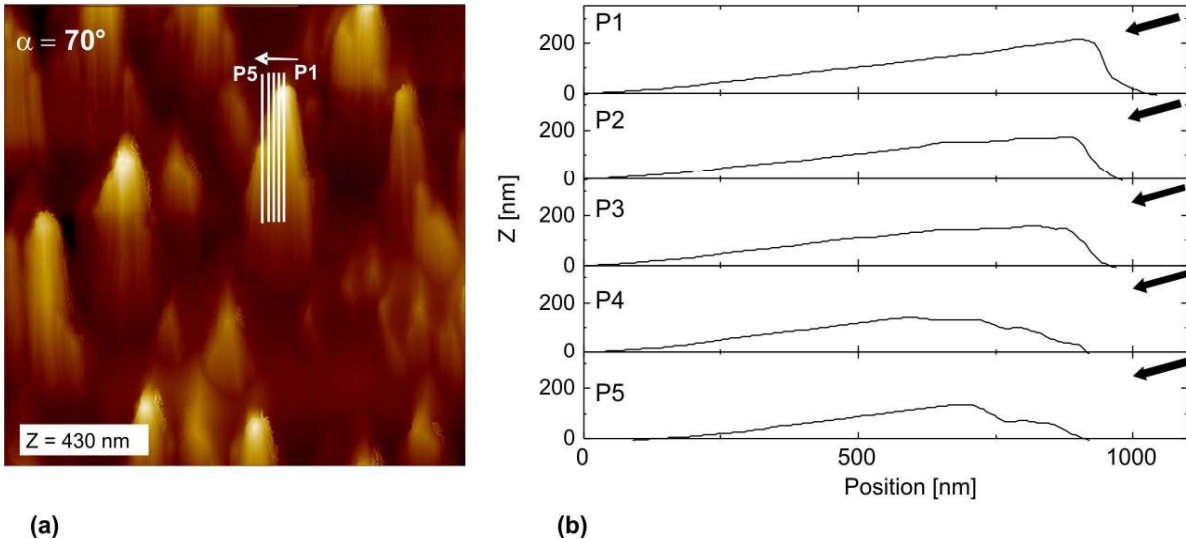
Figure 4.16. (a) AFM image of silicon after irradiation with Kr$^+$, $\Phi = 6.7 \times 10^{18}$ cm^{-2}, $E_{ion} = 1000$ eV, $U_{acc} = -1000$ V, $\alpha = 70°$. The image is 2.5 μm × 2.5 μm and it has a resolution of 512 × 512 pixels. (b): Height profiles, corresponding to the white lines in (a). The arrows indicate the ion beam direction.
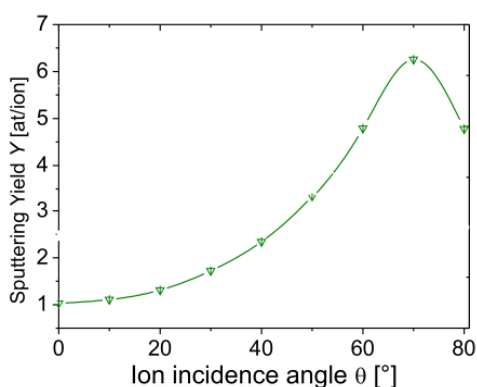
Figure 4.17. Ion incidence angle dependence of Si sputtering yields, for 2000 eV Kr$^+$.

In the steady state, Eq. 4.1 should be zero, thus the stable slopes are $\theta = 0°$, $\theta = 90°$, and $\theta = \theta_p$. Regions of the substrate with local angles different from these three incident angles, will be eroded until one of the angles of the stable slopes is reached. If the signs of $dY(\theta)/d\theta$ and $d\theta/dx$ are known, it can be determined if the slope increases or decreases under ion erosion. The term $dY(\theta)/d\theta$ will be positive if the incidence angle is lower than θ_p, while it will be negative when $\theta > \theta_p$. On the other hand, $d\theta/dx$ will be positive and negative for convex and concave surfaces, respectively. The resulting sign for Eq. 4.1 will show if the angle of the surface increases or decreases with the time. For convex surfaces, when $\theta > \theta_p$ the surface will be eroded until $\theta = 90°$ and when $\theta < \theta_p$, θ will tend to reach 0°.

4.3.3. Effect of the acceleration voltage at $\alpha = 65°$, 70°

It was already shown in subsection 4.2.1 that the acceleration voltage U_{acc} affects the divergence of the ion beam and the type of topography that evolves on silicon at near normal incidence. Here, its effect on the topography after irradiation at high angles ($\alpha = 65°$, 70°) is presented. In Fig. 4.18 AFM images of samples after bombardment with Kr$^+$, $E_{ion} = 2000$ eV, at $\alpha = 65°$, 70° with different U_{acc} are shown. At $\alpha = 65°$ perpendicular-mode ripples were formed (Fig. 4.18a-c). Additionally, features that resemble the parallel columnar structures in the first stages of formation are present on the surface. They are more clearly observed for $U_{acc} = $ -200 V (Fig. 4.18a) and the higher RMS roughness in comparison with acceleration voltage of -600 V and -1000 V is probably related to their presence. Thus, although the wavelength and amplitude of the perpendicular-mode ripples remained relatively constant as $|U_{acc}|$ increased, the

71
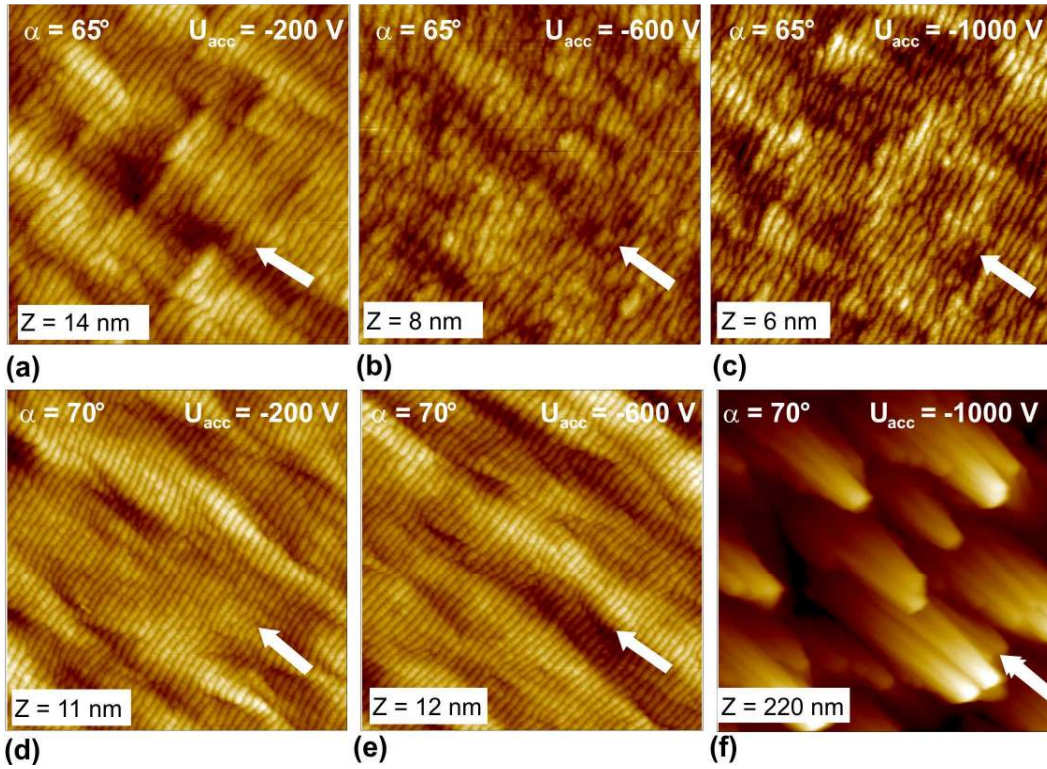
Figure 4.18. AFM images of samples after irradiation with Kr^+, $\Phi = 6.7 \times 10^{18}\,cm^{-2}$, $E_{ion} = 2000$ eV, $\alpha = 65°$ (a-c) and $\alpha = 70°$ (d-f), with $U_{acc} = -200$ V (a,d), -600 V (b,e) and -1000 V (c,f). The white arrows indicate the projection of the ion beam on the surface. The images are 2 µm × 2µm. The RMS roughness is (a): 1.9 nm, (b): 1.0 nm, (c): 0.9 nm, (d): 1.4 nm, (e): 1.7 nm, and (f): 75 nm.

RMS roughness decreased. Additionally, the regularity of the perpendicular-mode ripples seems to decrease for samples irradiated with increasing $|U_{acc}|$.

At $\alpha = 70°$ with $U_{acc} = -200$ V and $U_{acc} = -600$ V perpendicular-mode ripples were formed (Fig. 4.18d and 4.18e) together with some waves parallel to the ion beam projection on the surface. In agreement with the results presented in Fig. 4.11, the wavelength of the perpendicular-mode ripples is lower in comparison with the ripples formed at $\alpha = 65°$. With $U_{acc} = -1000$ V, high-amplitude columnar structures parallel to the ion beam dominate the topography (Fig. 4.18f).

4.3.4. Temporal evolution of perpendicular-mode ripples at high ion beam incidence angles

In Fig. 4.19 AFM images and PSD functions showing the evolution of the topography with the time for Si samples irradiated with 2000 eV Kr^+ at $\alpha = 65°$ are presented. It is observed that after 3 minutes sputtering ($\Phi = 3.4 \times 10^{17}\,cm^{-2}$) the ripples are already
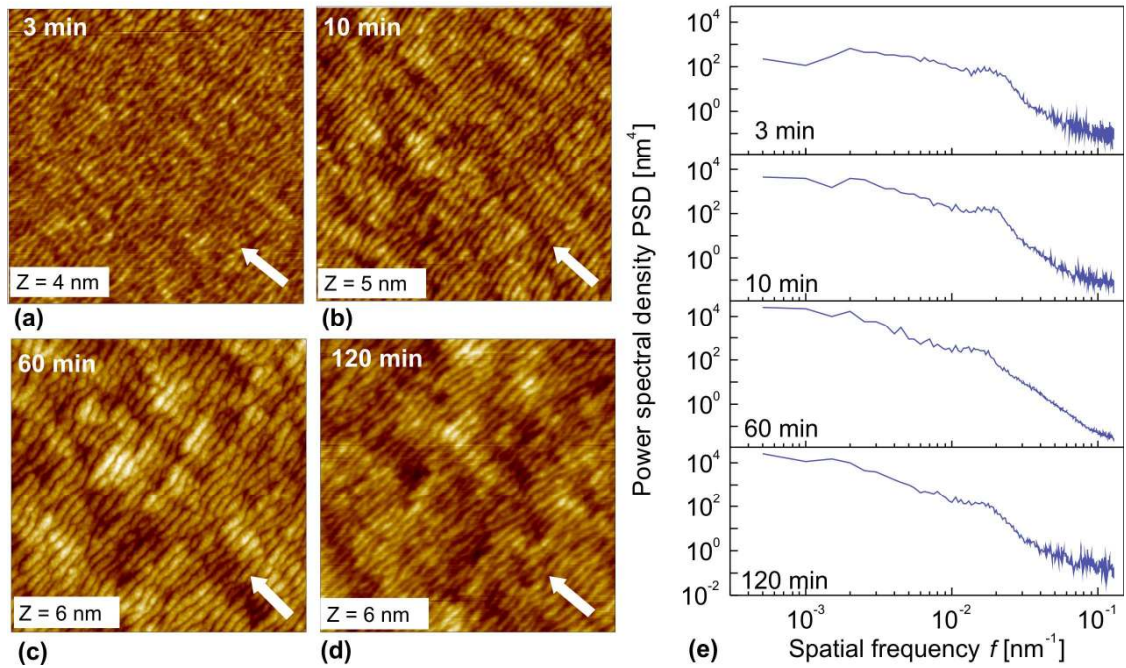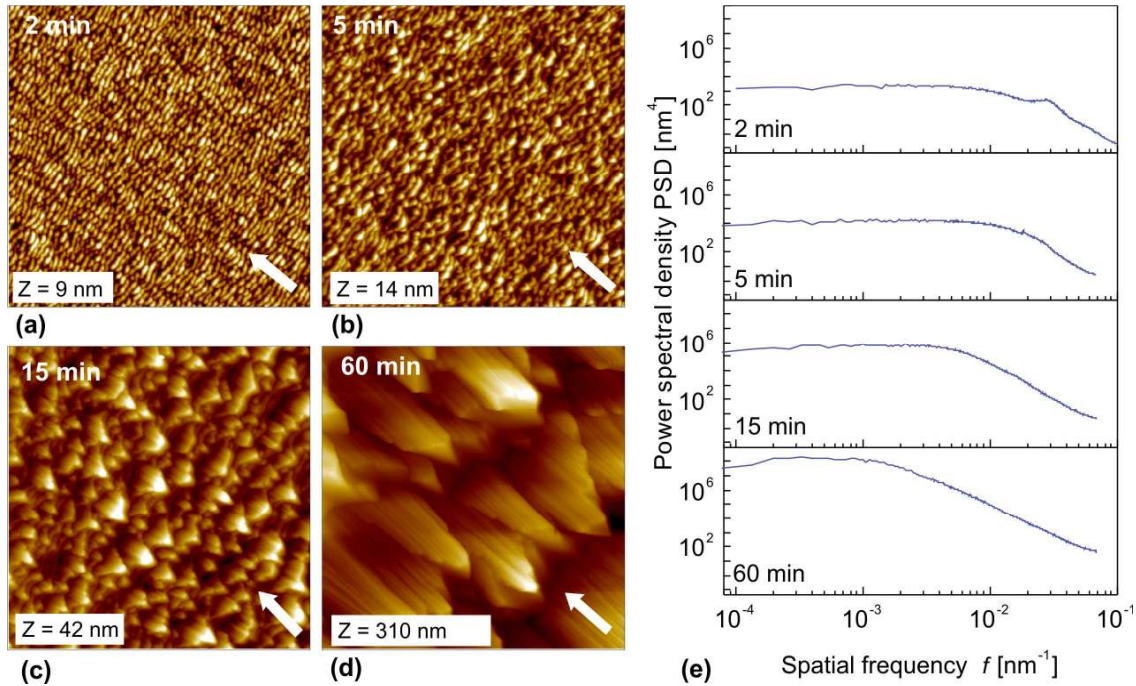
Figure 4.19. (a-d): AFM images of samples after irradiation with 2000 eV Kr$^+$, U_{acc} = -1000 V, α = 65° with different fluences Φ: (a): 3.4 × 10^{17} cm^{-2} (3 min), (b): 1.1 × 10^{18} cm^{-2} (10 min), (c): 6.7 × 10^{18} cm^{-2} (60 min) and (d): 1.3 × 10^{19} cm^{-2} (120 min). The images are 2 µm × 2 µm. The RMS roughness is (a): 0.4 nm, (b): 0.7 nm, (c): 0.9 nm, and (d): 0.8 nm. The arrows indicate the projection of the ion beam on the surface. (e): Corresponding power spectral density diagrams.

formed. A broad peak is observed in the PSD diagram (Fig. 4.19a), which indicates that the structures formed have already a dominant spatial frequency. The frequency of the peak is almost the same for the different fluences, which indicates that the wavelength of the ripples did not change with the time. According to the RMS roughness values, the amplitude of the ripples increased in the first minutes and then saturated. It can be seen in the PSD diagrams that the peak corresponding to the ripples does not seem to become narrower. This shows that there was no increase of the regularity of the features with the time, as it was the case for the ripples formed near normal incidence (analyzed in subsection 4.2.2).

4.3.5. Temporal evolution of parallel columnar structures at high ion beam incidence angles

In the previous subsection, the evolution of the perpendicular-mode ripples formed at high incidence angle with the time was shown. Here, the focus is set on the columnar structures.

Figure 4.20. (a-d): AFM images of samples after irradiation with 1000 eV Kr$^+$, U_{acc} = -1000 V, α = 75° for different fluences Φ: (a): 2.2×10^{17} cm^{-2} (2 min), (b): 5.6×10^{17} cm^{-2} (5 min), (c): 1.7×10^{18} cm^{-2} (15 min), and (d): 6.7×10^{18} cm^{-2} (60 min). The images are 2 μm × 2 μm. The RMS roughness is (a): 2 nm, (b): 3 nm, (c): 8 nm, and (d): 38 nm. The arrows indicate the projection of the ion beam on the surface. (e): Corresponding power spectral density diagrams.

In Fig. 4.20 AFM images and PSD functions of samples irradiated at α = 75° with 1000 eV Kr$^+$ and U_{acc} = -1000 V with different fluences are presented. The fluences Φ were 2.2×10^{17} cm^{-2} (2 min), 5.6×10^{17} cm^{-2} (5 min), 1.7×10^{18} cm^{-2} (15 min) and 6.7×10^{18} cm^{-2} (60 min). During the first minutes ripples that are perpendicular to the ion beam projection evolved (Fig. 4.20a). They resemble the starting phase of the ripples formed at α = 65° (Fig. 4.19a). A weak peak corresponding to the preferential frequency is observed in the PSD diagram (Fig. 4.20e). At larger fluences, columnar structures parallel to the ion beam evolved. The first columnar features formed between $\Phi = 5.6 \times 10^{17}$ cm^{-2} - 1.7×10^{18} cm^{-2} (5 min to 15 min) and their size increased with the time. They have a wide size distribution, thus no defined peak is observed in the PSD diagrams.

The temporal evolution of the topography was also analyzed for samples irradiated with Kr$^+$ at α = 80°, E_{ion} = 1000 eV, and U_{acc} = -1000 V. The fluences Φ were 2.2×10^{17} cm^{-2} (2 min), 5.6×10^{17} cm^{-2} (5 min), 1.7×10^{18} cm^{-2} (15 min), and 6.7×10^{18} cm^{-2} (60 min).

74
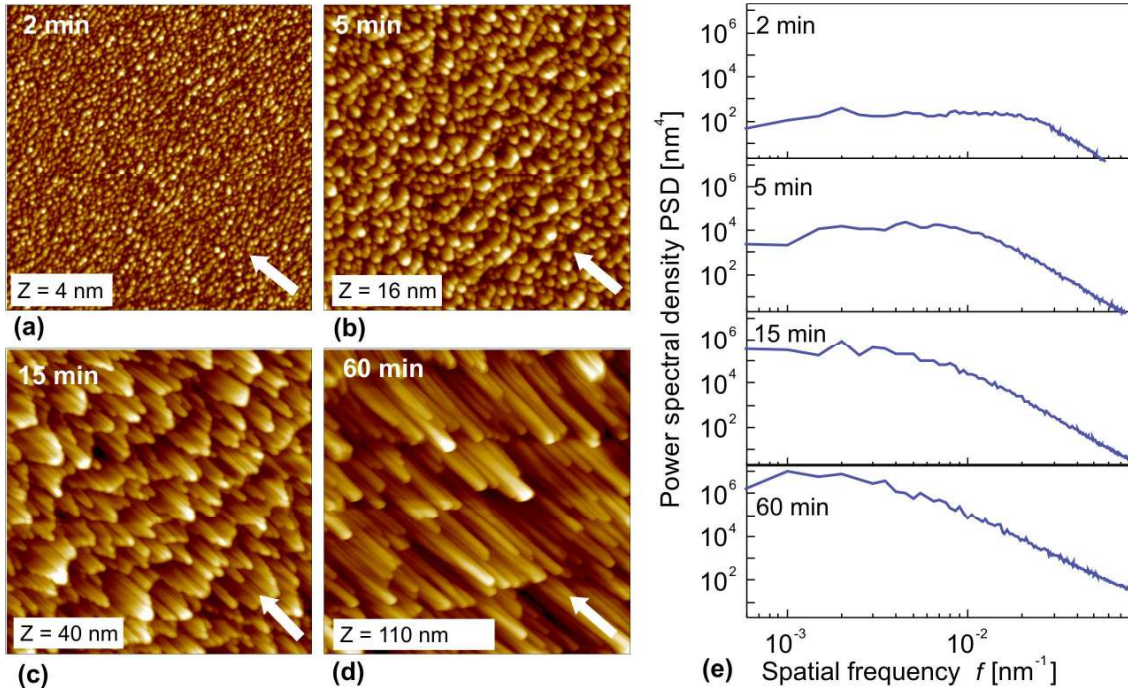
Figure 4.21. (a-d): AFM images of Si surfaces after irradiation with 1000 eV Kr^+, U_{acc} = -1000 V, $\alpha = 80°$ for different fluences. Φ = (a): $2.2 \times 10^{17}\,cm^{-2}$ (2 min), (b): $5.6 \times 10^{17}\,cm^{-2}$ (5 min), (c): $1.7 \times 10^{18}\,cm^{-2}$ (15 min), and (e): $6.7 \times 10^{18}\,cm^{-2}$ (60 min). The images are 2 μm × 2 μm. The RMS roughness is (a): 1 nm, (b): 3 nm, (c): 7 nm, and (d): 16 nm. The arrows indicate the projection of the ion beam on the surface. (e): Power spectral density diagrams.

In Fig, 4.21 AFM images and PSD functions are presented. The evolution of the topography is similar to that at $\alpha = 75°$. First, perpendicular-mode ripples evolved and at larger fluences the topography is dominated by columnar structures parallel to the ion beam. The first columnar features were formed at lower fluences in comparison with the features at $\alpha = 75°$ shown in Fig. 4.20; they are already present on the surface irradiated with $\Phi = 5.6 \times 10^{17}\,cm^{-2}$ (5 min). In comparison with the features formed at $\alpha = 75°$, the features formed here are lower in amplitude, and have a larger length to width ratio. According to the temporal evolution results presented in this subsection it seems that under ion erosion at $\alpha \geq 65°$ first ripples perpendicular to the ion beam are formed. After a certain erosion time, which depends on the bombardment conditions, and due to local variations of the ion beam incidence angle, columnar structures are formed. The incidence angle dependent sputtering is the dominant process giving the columnar structures facets with specific orientation and slopes. It was observed that at higher ion beam incidence angle, the columnar structures need lower fluences to evolve, they present a larger density on the surface and their length to width ratio is larger.

Chapter 5
Simultaneous Fe incorporation

In section 2.1 a short review of experimental observations about self-organization by ion beam erosion was given where the main experimental parameters affecting the topography evolution were addressed. It was mentioned that in the last years, the role of foreign atoms in the pattern formation has been studied [20, 21, 23, 25, 60, 62, 63] (see subsection 2.1.2.6). Inherently to the experimental setup used for this study, metallic atoms (mainly Fe) are incorporated simultaneously with ion bombardment under certain operational conditions. In this chapter, ion beam erosion with simultaneous Fe incorporation will be analyzed. First, in section 5.1, the origin of the metallic atoms and the regulation of the flux by the ion beam divergence will be described. In section 5.2 and 5.3 the correlation of the ion beam parameters, metals concentration, and resulting topography will be investigated.

5.1. Connection between divergence and Fe incorporation

In previous reports [32, 50], it was shown that for the ion beam facility used in this study the ion beam divergence, affects considerably the topography evolution on Si(001). A certain beam divergence was found to be necessary for the formation of ripples at near normal incidence. For the given experimental setup this fact is related with the incorporation of metals during the erosion, in particular Fe. To make clear the connection between the divergence and Fe incorporation, some details about the experimental setup should be given. In the ion beam facility used here, approximately 14 cm downstream from the grid extraction system there is cylindrical-shape stainless steel plate lining of 21.5 cm diameter. Some material from this plate may be sputtered by the ions and reach the substrate, in particular when the divergence of the beam is large. In section 3.1 the effect of the acceleration voltage U_{acc} in the angular distribution of the ions within the beam was shown. According to simulations (see subsection 3.1), the beamlets (ions leaving one aperture of the accelerator grid) present a higher divergence with U_{acc} = -1000 V in comparison with U_{acc} = -200 V. With U_{acc} = -1000 V most ions leave the extraction system with an angle of 7° (see Fig. 3.3). The effect of this difference in the divergence of the beam is schematically represented in Fig. 5.1. It
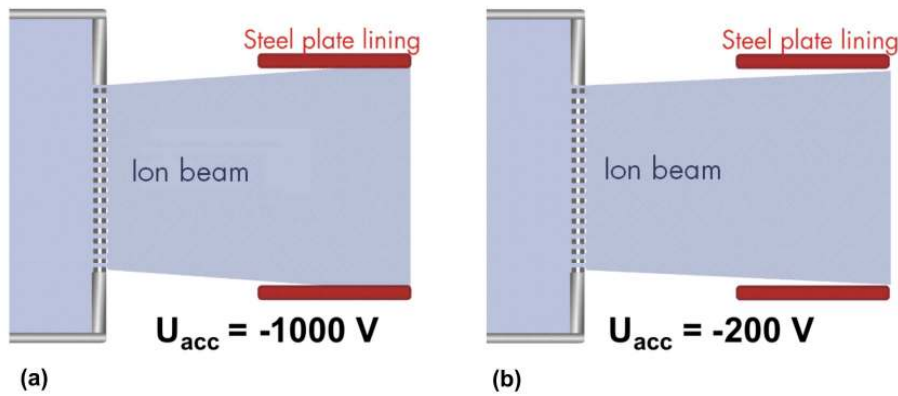
**Figure 5.1.** Schematic drawing of the ion beam shape for different acceleration voltages U_{acc}.

is observed that with the higher divergence corresponding to U_{acc} = -1000 V, some of the ions reach the stainless steel plate lining. This will result in sputtering of material from the lining and incorporation of metallic atoms, primarily Fe, from the lining onto the sample surface. With U_{acc} = -200 V, considering the angular distribution determined by simulations and presented in section 3.1, most ions will not reach the steel lining. This will lead to a significantly lower Fe flux. U_{acc} is not the only operational parameter that affects the divergence and in consequence the Fe flux that reaches the sample. As it was already mentioned in section 3.1, the plasma sheath position and shape determine the ion trajectory, which in turn are affected by the plasma properties, and the extraction system characteristics (voltages and geometry). Thus, E_{ion}, which is determined by the potential applied at the screen grid, also affects the divergence of the beam. Additionally, E_{ion} affects the sputtering rate of Fe from the lining. With respect to the geometry of the grid system, in section 3.1 the effect of the grid distance and aperture diameter in the angular distribution was briefly described.

5.2. Correlation between erosion conditions, Fe concentration and topography

Next, the correlation of the concentration of Fe and other metallic atoms on the Si samples after erosion, the operational parameters and the resulting topography will be analyzed.

5.2.1. Acceleration voltage

Samples were bombarded with 2000 eV Kr^+ at α = 15° with Φ = 3.4 × 10^{18} cm^{-2}, with U_{acc} = -1000 V and U_{acc} = -200 V. The AFM images in Fig. 5.2a and 5.2b show the
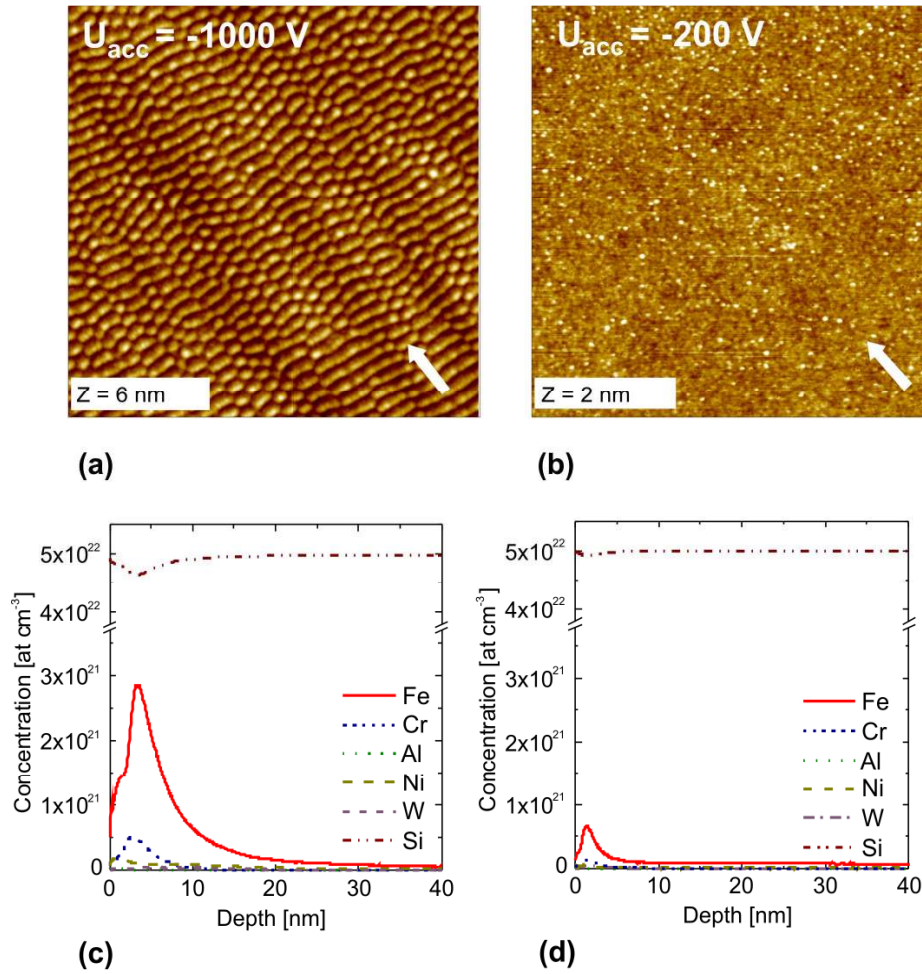
Figure 5.2. (a, b) AFM images of silicon surfaces after irradiation with 2000 eV Kr$^+$, with $\Phi = 3.4 \times 10^{18}$ cm^{-2}, at $\alpha = 15°$, with $U_{acc} = -1000$ V (a) and $U_{acc} = -200$ V (b). The images are 2 µm × 2 µm and have a resolution of 512 × 512 pixels. The RMS roughness is (a): 1.1 nm, (b): 0.2 nm. The white arrows indicate the projection of the ion beam on the surface. (c, d): Corresponding SIMS depth profiles.

resulting topography. Discontinuous ripples oriented perpendicular to the ion beam evolved when $U_{acc} = -1000$ V (Fig. 5.2a) while with $U_{acc} = -200$ V, the surface remained smooth (Fig. 5.2b). The samples were measured with RBS after erosion and as it was expected, the concentration of Fe was higher (more than three times) for $U_{acc} = -1000$ V than for $U_{acc} = -200$ V (1.92 × 10^{15} at cm^{-2} and 0.55 × 10^{15} at cm^{-2}, respectively). Additionally, depth profiling measurements were performed with SIMS. As a remainder, it should be mentioned that the SIMS results presented in this chapter were already calibrated using the RBS-SIMS correction factor. Details about the calibration and correction factor were given in subsection 3.2.5. The corresponding SIMS depth profiles are shown in Fig. 5.2c ($U_{acc} = -1000$ V) and 5.2d ($U_{acc} = -200$ V). It is observed
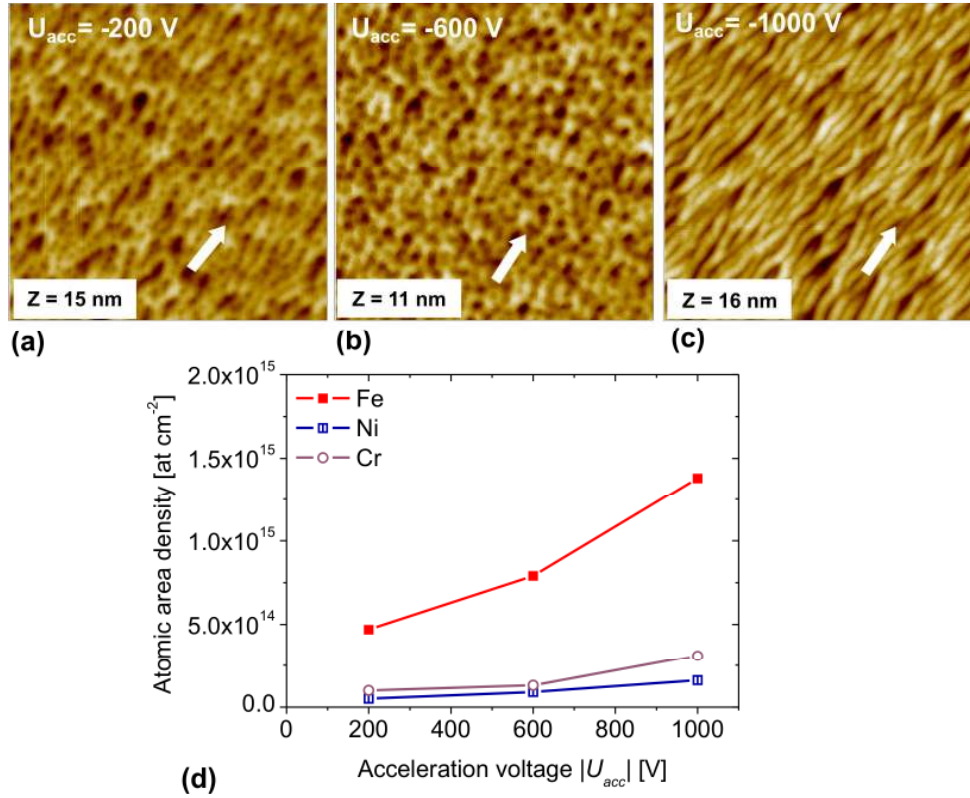
Figure 5.3. (a - c) AFM images of Si(001) surfaces after irradiation with 500 eV Kr$^+$, at $\alpha = 20°$, with $\Phi = 3.4 \times 10^{18}$ cm^{-2}, with $U_{acc} = -200$ V (a), $U_{acc} = -600$ V (b), and $U_{acc} = -1000$ V (c). The images are 2 μm × 2 μm and have a resolution of 512 × 512 pixels. The RMS roughness is (a): 1.5 nm, (b): 1.4 nm, and (c): 1.8 nm. The white arrows indicate the projection of the ion beam on the surface. (d): Plot showing the corresponding concentration of Fe, Cr, and Ni measured with RBS.

that for $U_{acc} = -1000$ V the concentration of Fe is significantly higher than for $U_{acc} = -200$ V and that the Fe atoms are present mostly in the first 3 to 4 nm and at larger depths the concentration decreases. Fe, which is the main component of the stainless steel lining, is the element with the highest concentration detected by SIMS and RBS, besides Si. Additionally, Cr, Ni (also from the steel lining) and Al from the sample holder (detected only with SIMS) are present in lower concentrations. Traces of W coming from the source cathode and neutralizer and Kr, the working gas, were also detected.

According to these results, the necessity of a certain divergence for the formation of ripples at near normal incidence that was previously observed [32, 50] may be related actually with a higher content of metallic atoms, in particular Fe.

The effect of U_{acc} in the topography evolution and Fe concentration at near normal incidence was also analyzed for lower E_{ion}. Samples were irradiated with 500 eV Kr$^+$

80

with different U_{acc}. As it can be seen from the AFM images presented in Fig. 5.3, structures elongated in the direction of the ion beam were formed with $U_{acc} = $ -200 V (Fig. 5.3a). They evolved also with $U_{acc} = $ -600 V (Fig. 5.3b) and with $U_{acc} = $ -1000 V, the structures are even more elongated in the beam direction, forming ripples parallel to the ion beam (Fig. 5.3c). According to the plot in Fig. 5.3d that shows the concentration of Fe, Cr, and Ni measured with RBS, the concentration of the three elements increases with increasing $|U_{acc}|$. As it was already mentioned, this may be explained by the increase of the divergence angle, which leads to higher Fe flux coming from the stainless steel plate lining.

By comparison of the results for low and high ion energy, it is observed that when $E_{ion} = 2000$ eV, the concentration of metals on the samples after erosion is higher than when $E_{ion} = 500$ eV keeping the other parameters constant. With respect to E_{ion}, it has to be considered that it affects the plasma sheath shape and position, and in turn the divergence of the beam. Additionally, E_{ion} controls the sputtering rate of the stainless steel plate lining, affecting the metallic flux that reaches the samples, and also the rate of the re-sputtering of metallic atoms from the silicon substrate. More about the effect of E_{ion} will be addressed in the next subsection.

5.2.2. Ion energy

In subsection 4.2.3 it was shown that although ripples perpendicular to the ion beam direction dominated the topography with $E_{ion} = 2000$ eV at near normal incidence, low amplitude waves parallel to the ion beam were also formed on the surface. The amplitude of these parallel-type waves increased when E_{ion} decreased and dominated the topography with $E_{ion} = 300$ eV. Here the correlation with the concentration of metallic atoms is analyzed. In Fig. 5.4 the topographies of Si surfaces after irradiation with Kr$^+$, at $\alpha = 20°$ with $\Phi = 3.4 \times 10^{18}$ cm^{-2}, and $U_{acc} = $ -1000 V with different E_{ion} are presented. The AFM images show similar topographies as those presented in subsection 4.2.3. With E_{ion} of 300 eV and 500 eV, the features dominating the surface topography are parallel to the ion beam direction (Fig. 5.4a, 5.4b). With $E_{ion} = 800$ eV together with the parallel-mode waves, ripples perpendicular to the ion beam are also observed on the surface (Fig. 5.4c). With higher E_{ion} the parallel-mode ripples are weaker and the topography is dominated by the perpendicular-mode ripples (Fig. 5.4d, 5.4e). In the plot
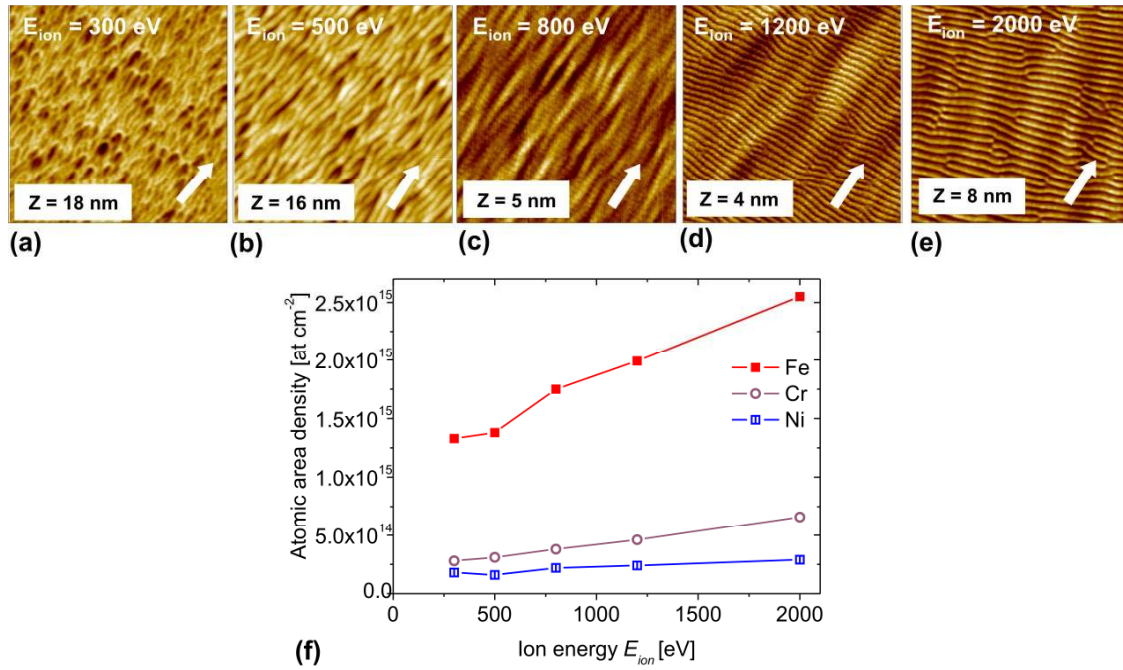
Figure 5.4. (a - e) AFM images of samples after irradiation with Kr$^+$, at $\alpha = 20°$, with $\Phi = 3.4 \times 10^{18}$ cm^{-2}, $U_{acc} = -1000$ V and $E_{ion} = 300 - 2000$ eV. The images are 2 μm × 2 μm and have a resolution of 512 × 512 pixels. The RMS roughness is (a): 2.0 nm, (b): 1.8 nm, (c): 0.7 nm, (d): 0.6 nm, and (e): 1.4 nm. The white arrows indicate the projection of the ion beam on the surface. (f): Plot showing the corresponding concentration of Fe, Cr, and Ni measured with RBS.

in Fig. 5.4f the concentrations of the metallic atoms determined by RBS are shown. It is observed that the concentrations of Fe, Cr and Ni increase with higher E_{ion}.

If the addition of metals is not considered, these results would represent a contradiction to the BH model [37]. However, here it is demonstrated that metals are incorporated simultaneously with the ion erosion and that the content of metals on the samples, in particular Fe, is strongly affected by the changes of E_{ion}. Thus, the change in the type of ripples that dominates the topography with E_{ion} may be also related with the metal incorporation.

Next, the effect of the ion energy will be analyzed, but with acceleration voltage $U_{acc} = -200$ V. In Fig. 5.5 AFM images of samples after irradiation with Kr$^+$, at $\alpha = 20°$ with $\Phi = 3.4 \times 10^{18}$ cm^{-2}, and $U_{acc} = -200$ V with different E_{ion} are shown. In this case, no ripples perpendicular to the ion beam projection evolved. Structures elongated in the direction of the ion beam were formed with low E_{ion} (300 and 500 eV). With $E_{ion} = 800$ eV and $E_{ion} = 1200$ eV, the surface became smoother; low amplitude
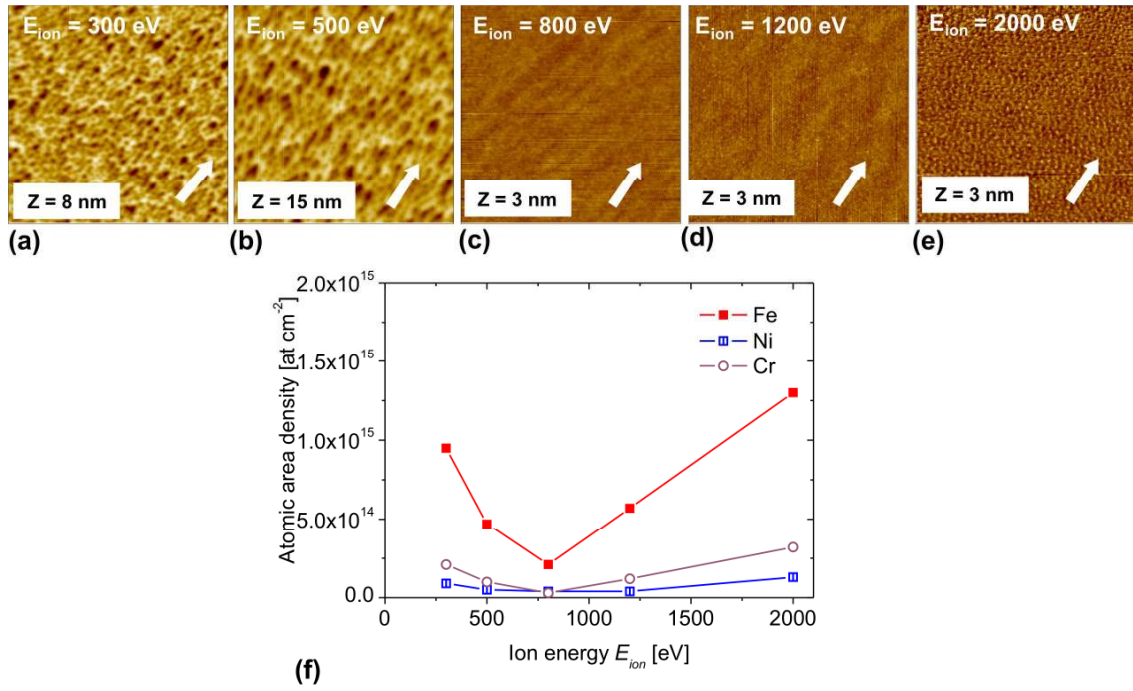
Figure 5.5. (a - e) AFM images of samples irradiated with Kr^+ at $\alpha = 20°$, with $\Phi = 3.4 \times 10^{18}\,cm^{-2}$, $U_{acc} = -200$ V and $E_{ion} = 300 - 2000$ eV. The images are 2 μm × 2 μm and have a resolution of 512 × 512 pixels. The RMS roughness is (a): 1.0 nm, (b): 1.5 nm, (c): 0.2 nm, (d): 0.2 nm, and (e): 0.4 nm. The white arrows indicate the projection of the ion beam on the surface. (f): Plot showing the corresponding concentration of Fe, Cr, and Ni measured with RBS.

undulations parallel to the ion beam are seen. Finally, with $E_{ion} = 2000$ eV dots with low amplitude evolved. In Fig. 5.5f, the metal concentrations measured with RBS are shown. It is observed that with low ion energy (300 eV and 500 eV), the Fe concentration is close to that corresponding to $U_{acc} = -1000$ V, and similar structures evolved (see Fig. 5.4a, 5.4b, 5.5a, and 5.5b).

At higher ion energies, the concentration of Fe is significantly higher with $U_{acc} = -1000$ V, than with $U_{acc} = -200$ V. and the topography looks different. From the energy range analyzed, the highest difference in Fe concentration with $U_{acc} = -1000$ V and $U_{acc} = -200$ V is for $E_{ion} = 800$ eV. In the first case the concentration is approximately 1.7×10^{15} at cm^{-2} and in the second one it is close to 2.5×10^{14} at cm^{-2}. The difference in the topography is also significant: in the first case ripples parallel and perpendicular to the ion beam direction were formed (Fig. 5.4c) and with $U_{acc} = -200$ V the surface is almost smooth (Fig. 5.5c). In the case of $U_{acc} = -200$ V, it is observed that with increasing E_{ion} the concentration of Fe decreases up to $E_{ion} = 750$ eV before

83

increasing. The increase rate of Fe concentration from $E_{ion} > 750$ eV is similar for both U_{acc} values (-200 V and -1000 V).

The explanation for this behavior may be related to the complex correlation between the extraction system potentials, the plasma properties and the plasma sheath. The higher Fe concentration for $U_{acc} = -200$ V at low ion energies may be connected with the findings reported by Tartz et al. in [106]. By simulations, they determined that if the extraction voltage is lowered below a critical value, part of the primary ions starts to impinge on the accelerator grid, which increases the divergence of the beam, leading in turn to a higher Fe flux.

According to the results presented in this subsection, when the concentration of Fe is higher than $\sim 1 \times 10^{15}$ at cm^{-2}, structure formation is observed, while for Fe concentration lower than $\sim 5 \times 10^{14}$ at cm^{-2}, the surface remains smooth. It was additionally observed that the concentration of Fe (or the other metals) alone does not determinate the resulting topography. For example, according to the RBS measurements, after irradiation at $\alpha = 20°$ with $E_{ion} = 2000$ eV and $U_{acc} = -200$ V, the remaining Fe concentration was almost the same as when it was irradiated at the same incidence angle but with $E_{ion} = 300$ eV and $U_{acc} = -1000$ V, on the other hand, the topography that evolved was completely different. Dots with low amplitude that slightly show an ordering perpendicular to the ion beam were formed in the first case, and ripples parallel to the ion beam projection on the surface were observed in the last one (Fig. 5.5e and 5.4a, respectively).

5.2.3. Ion beam incidence angle

In sections 4.1 and 4.2 the transition from ripples to smooth surface at low ion beam incidence angles was analyzed. It was observed that it is highly sensitive to those ion beam parameters controlling the divergence of the beam and Fe concentration. To analyze the correlation with the concentration of metals in this transition regime, samples irradiated at α from 0° to 30° with 2000 eV Kr$^+$, $U_{acc} = -1000$ V were examined. In Fig. 5.6 AFM images of samples after irradiation are presented. Under normal incidence irregular hole structures were formed, at $\alpha = 10°$ perpendicular-ripples evolved. The ripples amplitude decreased at higher ion beam incidence angle ($\alpha = 20°$) and at $\alpha = 30°$, the surface remained smooth. In the plot in Fig. 5.6e it is shown that the concentration of the metals decreased when the ion beam incidence angle increased,
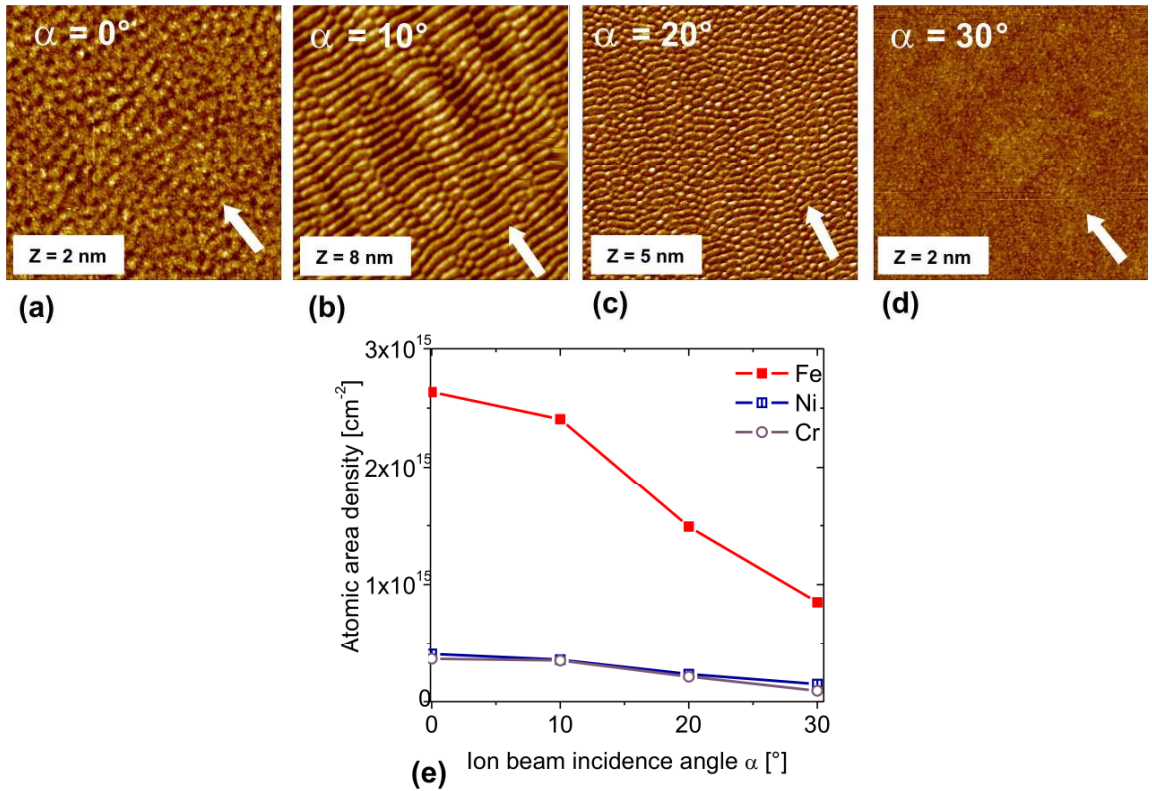
Figure 5.6. (a - d) AFM images of Si surfaces after irradiation with 2000 eV Kr^+, with $\Phi = 3.4 \times 10^{18}$ cm^{-2}, U_{acc} = -1000 V, at $\alpha = 0 - 30°$. The images are 2 µm × 2 µm and have a resolution of 512 × 512 pixels. The RMS roughness is (a): 0.3 nm, (b): 1.4 nm, (c): 0.9 nm, and (d): 0.2 nm. The white arrows indicate the projection of the ion beam on the surface. (e): Plot showing the corresponding concentration of Fe, Cr, and Ni measured with SIMS.

even though the ratio Fe to Kr^+ arriving at the sample surface remained constant for the different ion beam incidence angles.

In order to cover the complete range of ion beam incidence angles, Fe concentration on samples irradiated with 1000 eV Kr^+, with $\Phi = 7.8 \times 10^{17}$ cm^{-2}, with U_{acc} = -1000 V and U_{acc} = -200 V at α from 0° to 75° was analyzed. The fluence here was lower than the corresponding to the results presented in Fig. 5.6, in order to avoid losing depth resolution; i.e. with higher fluences large-amplitude structures evolve at large incidence angles, which would lead to a decrease in SIMS resolution. The concentration results are summarized in Fig. 5.7. As it was already shown in previous examples, the concentrations of Fe and the other metallic elements are significantly higher for U_{acc} = -1000 V in comparison with U_{acc} = -200 V. It is observed also that the
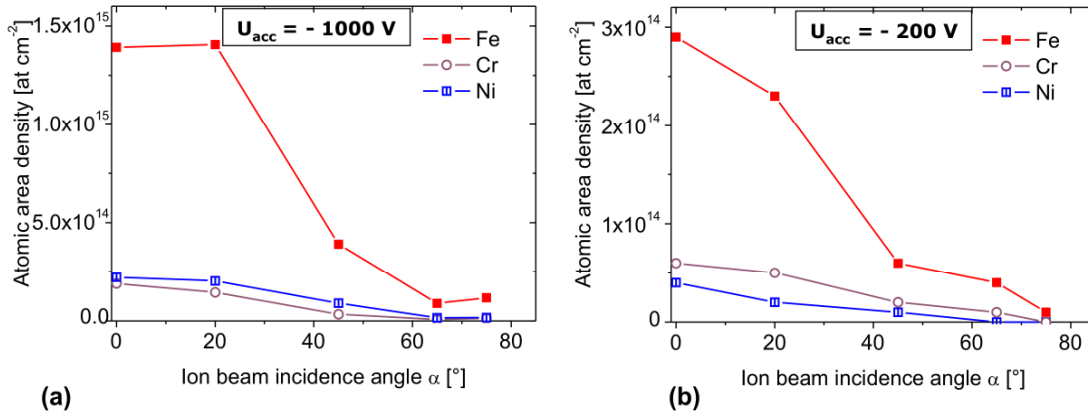
Figure 5.7. (a, b) Ion beam incidence angle vs. Fe, Cr, and Ni area density (determined by SIMS) for Si(001) after bombardment with 1000 eV Kr$^+$, $\Phi = 7.8 \times 10^{17}$ cm^{-2}, $\alpha = 0°$ - 75°, with $U_{acc} = $ -1000 V (a) and $U_{acc} = $ -200 V (b).

concentrations decreased with increasing ion beam incidence angles. In the case of $U_{acc} = $ -1000 V, Fe concentration increased slightly at grazing angles.

As in the case of the ion beam incidence angle range of 0°-30°, for $\alpha = 0°$-75° it is observed that the concentrations of Fe and the other metals decreased with increasing incidence angle, even though the ratio Fe to Kr$^+$ did not change. This fact is related to the sputtering yield dependence on the incidence angle. In Fig. 5.8 the dependence of the sputtering yield of Fe (Y_{Fe}) and Si (Y_{Si}) on the incidence angle (the local incidence angle θ is considered) for 2000 eV Kr$^+$ is shown. The sputter yield values were calculated using TRIM.SP code [148]. Both Y_{Fe} and Y_{Si} increase when θ increases, reaching a maximum and then decreasing again at grazing angles. For Fe θ_p is ~ 65° and for Si ~70°. The dashed line indicates the ratio of the Y_{Fe} to Y_{Si}. The plot shows that Y_{Fe} is higher than Y_{Si} from 0° up to ~ 70° and that the ratio Y_{Fe}/Y_{Si} decreases continuously in this incidence angle range. At $\theta > 70°$ Y_{Fe} is lower than Y_{Si}. These calculations would explain the decrease of Fe concentration on the sample when the ion beam incidence angle increases.

The results of the variation of Fe concentration with the incidence angle were additionally compared with the predictions from the model for surfactant sputtering developed by Hofsäss and Zhang [62, 63]. They studied ion irradiation with simultaneous atom deposition. They called the deposited atoms *surfactant atoms* (surface active agents) and they investigated different surfactant-substrate combinations.
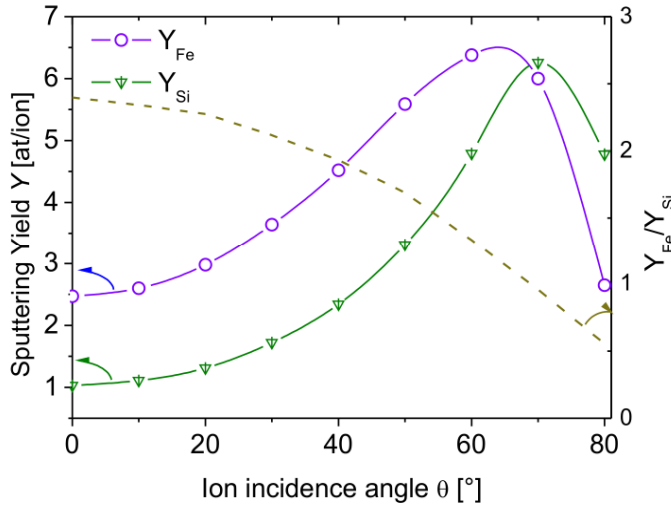
Figure 5.8. Incidence angle dependence of Fe and Si sputter yields, for 2000 eV Kr$^+$. The dashed line indicates the ratio Y_{Fe}/Y_{Si}.

Their model describes the effect of surfactants for non-miscible systems. It predicts a decrease of the substrate sputter yield as the surfactant concentration increases. If the deposition rate is low, i.e. $J_D < J Y_S$, where J_D is the deposition flux, J the ion flux, and Y_S the sputter yield of the surfactant in bulk, net erosion occurs. The system is in the sputtering regime. In that case the atomic area density of the surfactant on the substrate saturates and the saturation concentration is given by [62, 63]:

$$\sigma_{sat} = \sigma_0 \, ln\left(\frac{1}{1-(J_D \, / \, JY_S)}\right) \tag{5.1}$$

where σ_{sat} is the surfactant atomic area density on the substrate once the steady state is reached, σ_0 a characteristic surfactant concentration. This would imply that with constant deposition and ion fluxes, the variation of the surfactant concentration in the steady state with the ion incidence angle would be:

$$\frac{\sigma_{sat}(\theta)}{\sigma_{sat}(\theta = 0°)} = ln\left(\frac{1}{1-(J_D \, / \, JY_S(\theta))}\right) / c \tag{5.2}$$

where c is a constant. According to the ion incidence angle dependence of Fe sputter yield calculated using TRIM.SP [148] for 2000 eV Kr$^+$, the concentration of Fe in the steady state on Si at different incidence angles would vary as shown in the plot in Fig. 5.9. These calculations agree with the observations presented in Fig. 5.7 that show how the concentration changes at the different ion beam incidence angles.
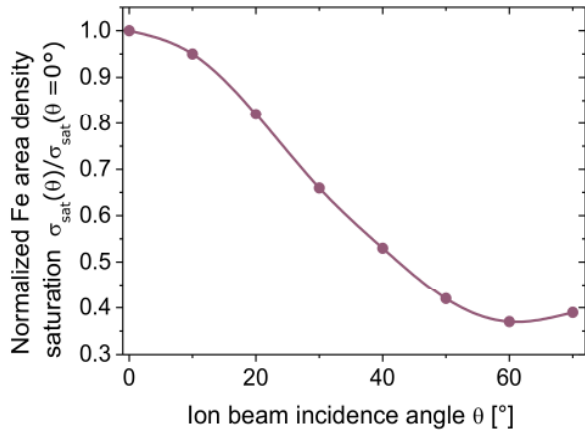
Figure 5.9. Incidence angle dependence of the concentration of Fe (normalized to that at normal incidence) on Si at the steady state for 2000 eV Kr^+ calculated using the model from Hofsäss and Zhang [62, 63]
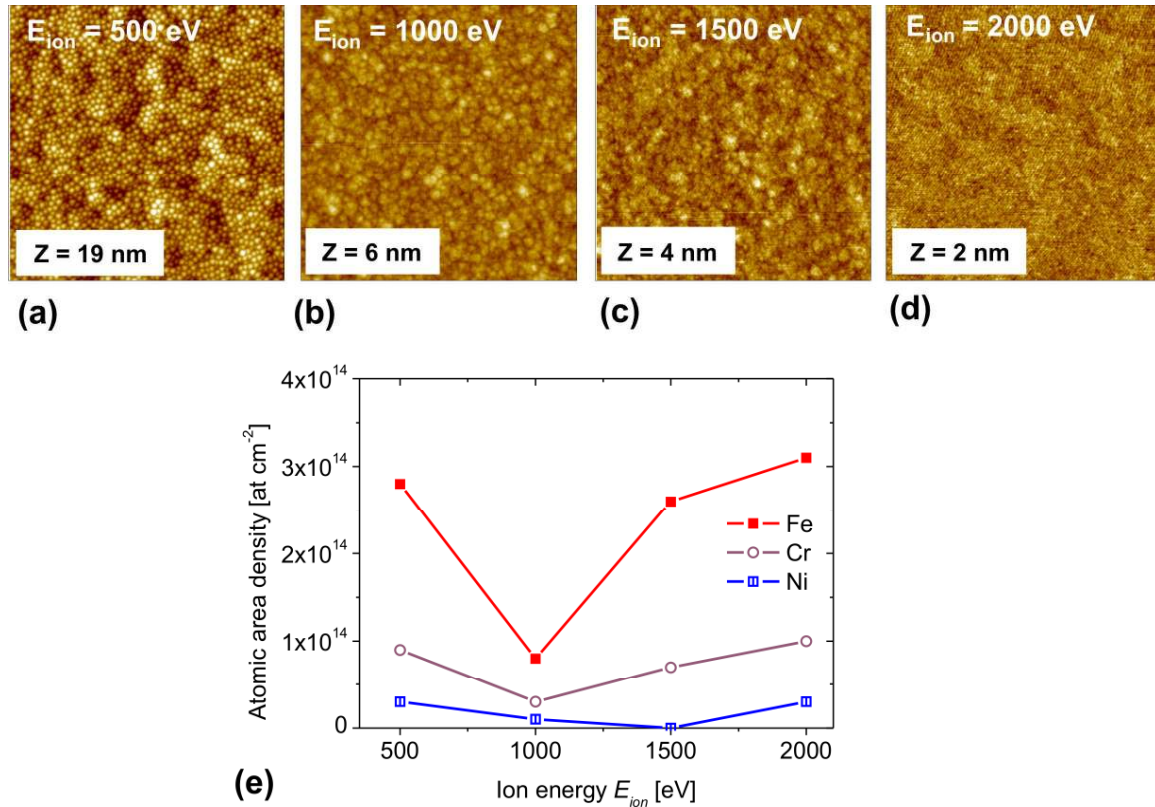
Figure 5.10. (a – d) AFM images of Si(001) surfaces after irradiation with Kr^+, at $\alpha = 75°$, with simultaneous rotation ($\sim$ 10 rpm), with $\Phi = 3.4 \times 10^{18}$ cm^{-2}, U_{acc} = -1000 V and E_{ion} = 500 – 2000 eV. The images are 2 µm $\times$ 2 µm and have a resolution of 512 $\times$ 512 pixels. The RMS roughness is (a): 2.7 nm, (b): 0.5 nm, (c): 0.4 nm, and (d): 0.2 nm. The white arrows indicate the projection of the ion beam on the surface. (e): Plot showing the corresponding concentration of Fe, Cr, and Ni measured with RBS.

As it was mentioned in subsection 2.1.2, when Si is irradiated at high incidence angles with simultaneous rotation of the sample around its normal, hexagonally arranged dots can be formed. Here, the correlation of Fe concentration with the topography evolution and different ion energies (E_{ion} = 500 eV – 2000 eV) for samples irradiated with Kr$^+$ at α = 75° with Φ = 3.4 × 10^{18} cm^{-2}, U_{acc} = -1000 V, and simultaneous rotation (12 rpm) is presented. The AFM images presented in Fig. 5.10 show that dots are formed with E_{ion} = 500 eV. With increasing ion energy, the amplitude of the dots decreased and the surface smoothened.

With respect to the concentration of metallic atoms, it is observed in the plot in Fig. 5.10e, which shows the RBS results, that Fe concentration ranges between 0.8×10^{14} at cm^{-2} and 3.0×10^{14} at cm^{-2}. Such results are in agreement with the previous results comparing low and high incidence angles (Fig. 5.6 and 5.7). Here, Fe does not seem to play an important role in the pattern formation; i.e. for E_{ion} of 500 eV, 1500 eV, and 2000 eV Fe concentration is almost the same, however, different topography evolution was observed (Fig. 5.10a, 5.10c, and 5.10d).

5.2.4. Fluence

It was shown in subsection 4.2.2 that the ordering of the structures formed at near normal incidence increased with erosion time. Here, results about the variation of the concentration of metallic atoms with the time are shown. The AFM images of samples irradiated with 2000 eV Kr$^+$, with U_{acc} = -1000 V, at α = 20°, with fluences of 2.2×10^{17} cm^{-2}, 5.6×10^{17} cm^{-2}, 1.7×10^{18} cm^{-2}, 3.4×10^{18} cm^{-2}, and 7.8×10^{18} cm^{-2} (corresponding to 2 min, 5 min, 15 min, 30 min, and 70 min, respectively) are presented in Fig. 5.11. In agreement with the results in subsection 4.2.2, it is observed that the ordering of the ripples increased with the erosion time. The plot in Fig. 5.11f shows the RBS results. The concentration of the metals seems to remain relatively constant with the fluence. It is also observed that for a fluence of 2.2×10^{17} cm^{-2}, i.e. 2 minutes erosion, the concentration corresponding to the steady state is already reached. After this time, the native SiO$_2$ layer on Si is completely removed, the thickness of the amorphized region is stabilized, and a balance between the arrival and resputtering of the metallic atoms is achieved.

The experiments were repeated and the samples analyzed with SIMS, and the results agree with these presented here.

Figure 5.11. (a-e) AFM images of Si surfaces after bombardment with 2000 eV Kr$^+$ with U_{acc} = -1000 V, at α = 20°, with fluence Φ of (a): 2.2×10^{17} cm^{-2}, (b): 5.6×10^{17} cm^{-2}, (c): 1.7×10^{18} cm^{-2}, (d): 3.4×10^{18} cm^{-2}, and (c): 7.8×10^{18} cm^{-2}. The images are 2×2 μm^2. The white arrows indicate the projection of the ion beam on the surface. (f) Plot showing the corresponding concentration of Fe, Cr, and Ni measured with RBS.
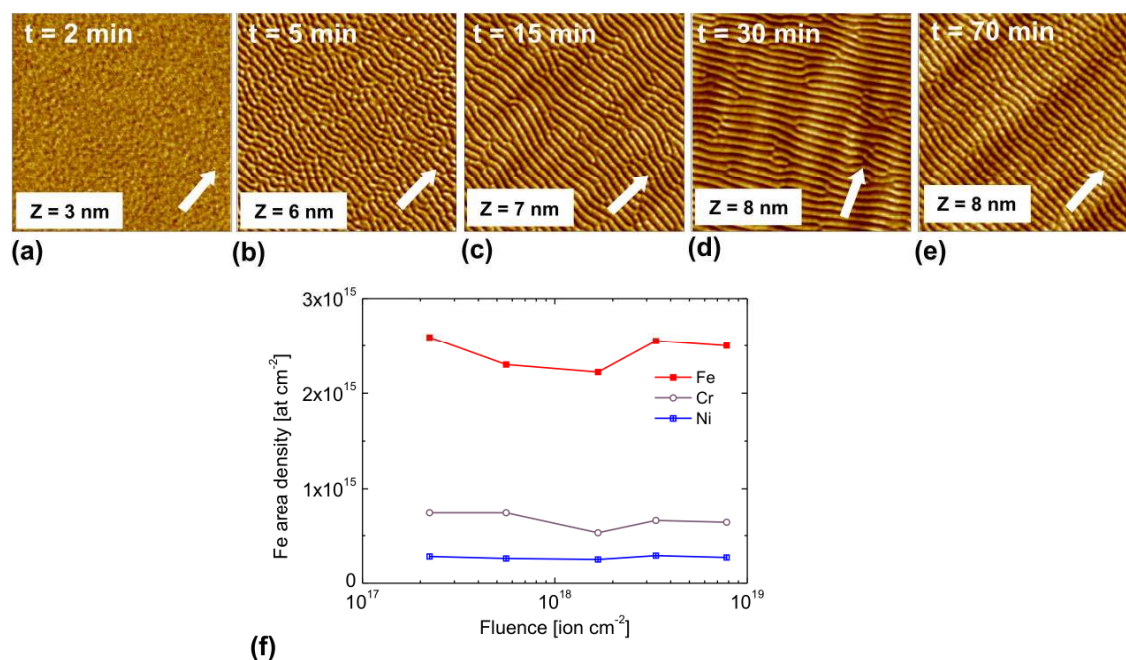
5.3. Lateral distribution of Fe in cross-section of near-surface region

By the analytical methods used here to detect the presence of Fe in the samples after erosion, i.e. SIMS and RBS, the position of the metallic atoms on the surface and near-surface region is not possible to determine. Therefore, High Resolution Transmission Electron Microscopy (HRTEM) was used. The HRTEM cross-sectional view of the surface together with AFM images of Si(001) after the irradiation with Kr$^+$ at two different incidence angles, α = 20° and α = 65°, are presented in Fig. 5.12. In both cases ripples perpendicular to the ion beam evolved. The wavelength and amplitude of the ripples at α = 65° are ~ 55 – 60 nm and ~ 2 – 3 nm, respectively, while the ripples at α = 20° have a wavelength ~ 45 nm and an amplitude ~ 2 nm. Those formed at α = 20° have a higher regularity (Fig. 5.12c and 5.12d). As it was shown above, the Fe concentration in the steady state is highly affected by the ion beam incidence angle. According to previous results, the Fe concentration is about 7 times higher for α = 20°. In the HRTEM micrographs the crystalline Si substrate is observed for both samples; i.e. the dark region at the bottom. The light top area represents the glue employed for
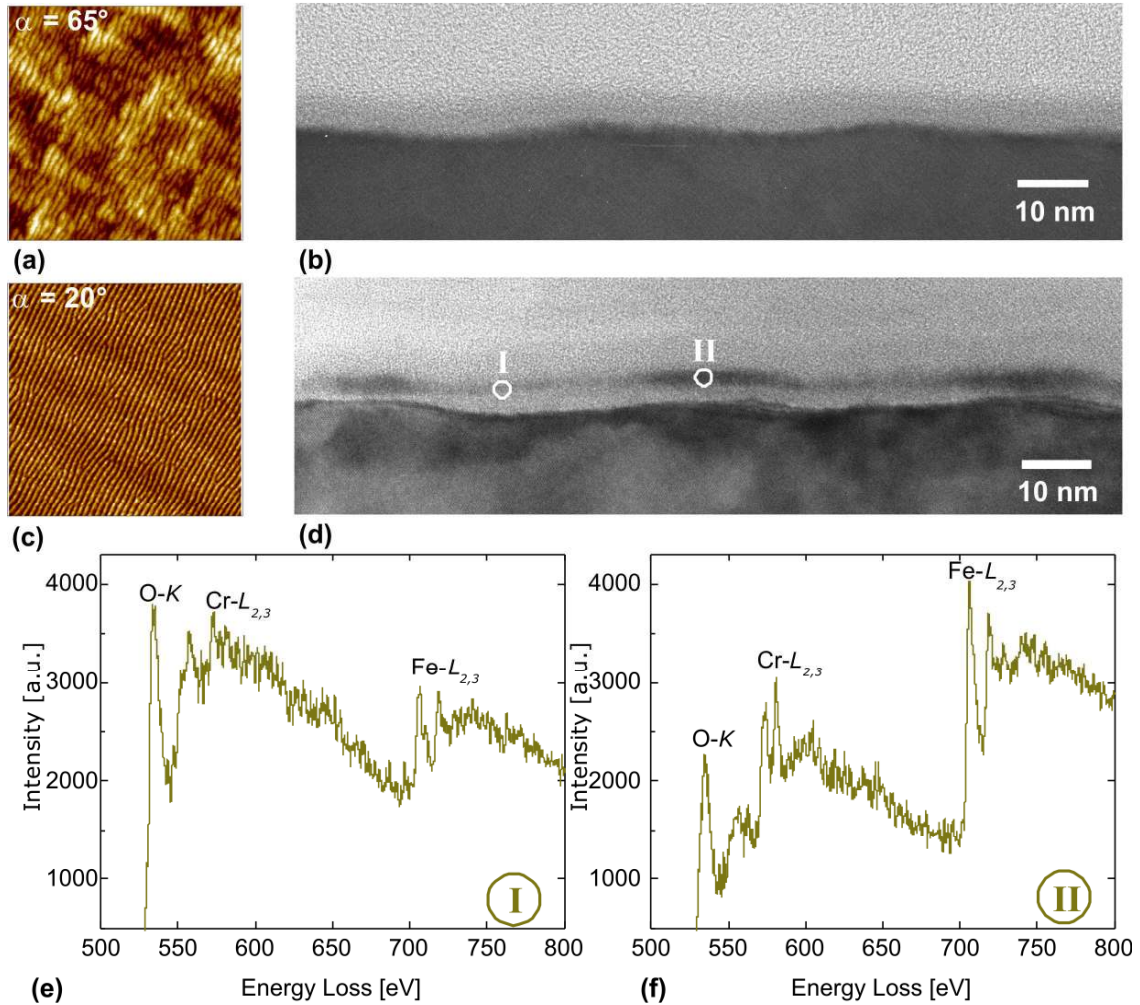
Figure 5.12. (a - d) AFM images and HRTEM cross-sections of Kr^+-sputtered silicon surfaces ($\Phi = 8.7 \times 10^{18}$ cm^{-2}, $U_{acc} = -1000$ V, $E_{ion} = $ (a, b) 2000 eV, (c, d) 1500 eV, $\alpha = $ (a, b): 65°, (c, d): 20°). The AFM images are 2 x 2 μm^2 with a resolution of 512 × 512 pixels and the height scale is (a): 6 nm, (c): 3 nm. (e, f) EELS spectra corresponding to the positions I and II indicated in (d)

the sample preparation. Between them, a layer of some nm is distinguished. This layer corresponds to amorphous Si, which is formed due to the ion irradiation, together with SiO_2 formed after the exposure to air. Also most contaminants are found in this layer. It is clearly observed that the layers of both samples look different. For the sample sputtered at $\alpha = 65°$ (Fig. 5.12b) the layer appears homogenous while the layer of the sample corresponding to $\alpha = 20°$ (Fig. 5.12d) has some dark regions at the crests of the ripples. The composition of the dark regions was analyzed using Electron Energy Loss Spectroscopy (EELS) and compared with the composition at the valleys. In Fig. 5.12e and 5.12f the EELS spectra for the positions I and II indicated in Fig. 5.12d are shown.

It is clearly seen that the concentration of Fe and Cr is higher at the crest of the ripple (dark region) than at the valley.

.

Chapter 6
Discussion

In chapter 4 and 5 experimental observations of Si surfaces bombarded with Kr^+ with energies up to 2000 eV under different erosion conditions were shown. The results corroborate the complex correlation between the erosion parameters and topography evolution.

In addition to some of the typical parameters that are considered to be involved in the pattern formation, i.e. ion energy, incidence angle, and fluence, here specific parameters of the Kaufman-type source utilized were studied. Additionally, the incorporation of metallic atoms, in particular Fe, was analyzed. The incorporation of Fe is inherent to the ion erosion facility used for this work and it seems to be important for the formation of certain patterns.

According to the results presented in the previous chapters two different situations can be distinguished. For negliglible Fe concentration, no pattern seems to evolve when the incidence angle is below ~ 60°. At higher angles ripples that are perpendicular to the ion beam projection on the surface are formed at low fluence. They may correspond to the ripples predicted by Bradley and Harper [37] as a result of the interplay between curvature dependent sputtering and relaxations mechanisms. With larger fluence columnar-like features that are parallel to the beam direction evolve. If Fe atoms are additionally incorporated during ion erosion, the situation changes. The behavior of the topography at high angles, i.e. above ~ 60°, does not seem to be affected significantly by the metallic atoms. However, at near normal incidence dots and ripples showing a relatively high regularity may evolve at incidence angles near ~ 5° - 35°. At intermediate angles, i.e. ~ 35° - 60° the surfaces smoothens.

In the following sections, the results presented in chapter 4 and 5 will be further discussed. Firstly, the focus will be set on the incorporation of Fe, analyzing the correlation of Fe flux with different erosion parameters. Sections 6.2 and 6.3 will address the pattern formation at low and high ion beam incidence angles, respectively.

6.1. Fe incorporation

Fe atoms (together with lower amounts of Cr and Ni) come from the sputtering of a stainless steel plate lining situated between the ion source and the sample. The

cylindrical-shape lining has a diameter slightly larger than the ion beam; therefore, a divergent beam leads to sputtering of metallic atoms, in particular Fe, from the lining. As the divergence of the beam becomes larger, the Fe flux is expected to increase as well. The divergence of the beam is determined by the position and shape of the plasma sheath near the extraction system and the extraction system itself. The properties of the plasma sheath are, in turn, controlled by the potentials applied to the extraction grids, the geometry of the grids, and the plasma properties.

The potentials applied at the screen and extraction grids are the beam voltage U_b (which determines the ion energy E_{ion}) and the acceleration voltage U_{acc}, respectively. It was shown by simulations that U_{acc} affects strongly the angular distribution of the ions, and in consequence, the divergence of the beam. For constant ion energy E_{ion}, an increase of $|U_{acc}|$ increases the divergence of the beam (see section 3.1 and Fig. 3.3). Considering the divergence predicted by the simulations and the geometry of the erosion facility, it was shown that the bombardment of the samples can be performed with or (almost) without co-sputtering of the stainless steel plate lining; i.e. with high and low ion beam divergence, respectively. This was corroborated by RBS and SIMS measurements, which showed a higher concentration of Fe on the samples when the divergence of the beam was increased, changing U_{acc} and keeping the other parameters constant. The area density of Fe on the samples after bombardment with a high divergent beam, i.e. with high $|U_{acc}|$, was in some cases higher than 1×10^{15} at cm^{-2}, while it was observed to be about 10 times lower in the case of low divergence, i.e. low $|U_{acc}|$. (subsection 5.2.1).

The incorporation of metals, in particular Fe, by bombardment with a high divergent beam could be the explanation for previous results [32, 50] which showed that, for the erosion facility used here, the divergence of the beam affected the surface evolution. It was observed that the formation of ripples at near normal incidence requires a relatively divergent ion beam. In particular, the effect of the acceleration voltage U_{acc} was considered. These observations were corroborated in this study. It was shown that the ripples are stable at a larger range of angles when the divergence is larger (see subsection 4.2.1), which corresponds with a higher Fe flux (see subsection 5.2.1).

The potential applied at the screen grid U_b, which determines the ion energy E_{ion}, was also shown to affect the concentration of Fe on the samples after erosion (subsection 5.2.2). On the one hand, an effect on the beam divergence is expected, since the potentials applied at the grids affect the angular distribution of the ions within the beam.

On the other hand, since E_{ion} affects the sputter yield, a change in the Fe sputter rate should occur.

The plasma properties and their correlation with the beam divergence are difficult to estimate. Here it was shown that the discharge voltage, i.e. the voltage applied between the cathode and the anode, affects also the stability of the features formed at near normal incidence (subsection 4.2.1). This may be also related to a change in the divergence of the beam and Fe flux.

With respect to the geometry of the extraction system, which determines also the beam divergence, the grid distance was observed to affect also the pattern evolution. Additionally, the operation time of the extraction system, which is expected to increase the size of the grid apertures, was demonstrated to affect as well the formation of features at near normal incidence.

Besides Fe arrival, its re-sputtering from the sample should be also considered. Under the given erosion conditions, Fe atoms reach continuously the silicon substrate and some of them are also continuously re-sputtered. It was demonstrated here that a steady state is reached shortly after the beginning of the irradiation where the pattern does not change and the concentration of Fe is constant (subsection 4.2.2 and 5.2.4). It was also shown that the concentration of Fe in the steady state decreased with increasing angles, although the ratio Kr^+ to Fe was kept constant. This is related with the sputtering yield dependence on the incidence angle. In subsection 5.2.3 (Fig. 5.8) the curves for the variation of Y_{Fe} and Y_{Si} with the incidence angle for Kr^+ were shown. Y_{Fe} increases up to an incidence angle near 65°; this increase would explain the decrease of Fe concentration on the sample with increasing ion beam incidence angle. These observations agree also with the model for surfactant sputtering developed by Hofsäss and Zhang [62, 63](subsection 5.2.3).

6.2. Near normal incidence

Several studies published in the last years [29, 31, 32, 38] show the formation of different nanostructures at near normal incidence, i.e. α from 0° to ∼ 35°. Of special interest due to their relatively high regularity are the ripples, which are perpendicular to the ion beam projection on the surface, formed with ion energy E_{ion} between 1000 eV and 2000 eV. The wavelength of the ripples can be tuned in the range of 40 nm to 70 nm and their amplitude up to ∼ 10 nm by choosing the appropriate E_{ion} and ion beam

incidence angle α. However, their formation seemed to be, up to recently, limited to the experimental setup used for this work. The generation of this type of nanopattern using other ion sources and the (apparently) same erosion conditions did not seem to be possible. In this study, it was demonstrated that this fact was related to the formerly inadvertent metallic atoms incorporation, in particular Fe, inherent to the given ion erosion facility. Fe incorporation seems to be necessary for pattern formation; otherwise, the surface remains smooth. This suggested explanation seems to agree with the results from Macko et al [21]. They reported the formation of ripples and dots at near normal incidence on Si(001) with 2000 eV Kr^+ with simultaneous co-sputtering of stainless steel. Without co-sputtering the surface remained smooth. The ripples and dots generated showed the size and appearance of the nanostructures obtained here.

In this study Si surfaces were irradiated at near normal incidence with different Fe fluxes; i.e. controlling the ion beam divergence by E_{ion} and U_{acc}. The concentration of Fe on the sample in the steady stage was measured after the erosion. It was observed that when the concentration of Fe was larger than $\sim 1.5 \times 10^{15}$ at cm^{-2} there was pattern formation, while when it was lower than $\sim 0.5 \times 10^{15}$ at cm^{-2} the surface remained smooth. In the former case, holes or dots were formed at normal incidence, i.e. $\alpha = 0°$, ripples evolved at $\alpha \sim 5° - 25°$, at higher angles in some cases dots or ripples-dots were observed, and at α larger than $\sim 35°$ (up to $\sim 60°$), the surface smoothened. Together with this transition from ripples to smooth surface when α increases, it was observed that the concentration of Fe decreased.

Further observations that may be also related to the incorporation of metals were those presented in subsections 4.2.3 and 5.2.2. It was shown that both perpendicular- and parallel-mode ripples were formed but the perpendicular-mode dominated the topography when E_{ion} was 2000 eV and when E_{ion} was 300 eV the parallel-mode ripples were the only type of features observed. The decrease of E_{ion} is accompanied by a decrease of the Fe concentration on the sample.

By SIMS measurements the depth distribution of Fe was determined. It was shown that most Fe atoms are in the first 3 to 4 nm (subsection 5.2.1). Additionally, the lateral distribution was evaluated by EELS measurements, which showed that Fe atoms are mainly situated on the crest of the ripples (section 5.3). The temporal evolution of the ripples (subsection 4.2.2 and 5.2.4) and these observations suggest that there might be a migration of the metallic atoms on the surface.

The mechanisms behind pattern formation are not completely understood. According to most theoretical models, based on Bradley and Harper model [37] (subsection 2.3), the pattern formation is considered to be the result of the interplay between curvature dependent sputtering and different relaxation mechanisms. However, none of these models consider the presence of foreign atoms.

The role of Fe in the pattern formation has not been determined yet.

The formation of cones or pyramids during the ion sputtering in presence of a *seed material* has been first observed several decades ago [55]. The foreign atoms create regions with different sputter rates. The seed material should have lower sputtering yield or higher melting point [149]. With respect to the system studied here, only the second requirement is fulfilled, since Fe has a higher sputtering yield than Si, but also a higher melting point; the melting points are 1808 K for Fe and 1683 K for Si. However, these cones and pyramids formed by seeding are in the micrometer scale [55, 56, 58, 59].

Pattern formation could be also be related to the stresses introduced by the metallic atoms. The stress relieve could lead to protuberance formation. However, no stress was detected by grazing incidence X-ray techniques in samples irradiated for this studied [150]. These findings do not agree with the results from Ozaydin et al. [60], who studied the surface stress evolution during ion sputtering of pure Si and Mo-seeded Si. In the latter case they observed a continuous increase of tensile stresses with the time.

It is not known for certain if the formation of iron silicides occurs. Measurements with X-Ray Photoelectron Spectroscopy XPS did not provide reliable results about the presence of silicides. Sánchez-García et al. [24, 25] found some evidence of the formation of silicides on Si samples irradiated with 1000 eV Ar^+ at normal incidence.

If iron silicides were formed, they might lead to inhomogeneities in the sputtering and diffusion processes. However, the presence of inhomogeities is not sufficient to explain the formation of regular structures. The continous ion bombardment could induce the self-organization of the silicides leading to the formation of the nanostructures [151]. It was shown that Ar^+ bombardment of metal silicide nanowires on silicon changed their ordering on the surface. Irradiating a silicon substrate with randomly oriented $TiSi_2$ nanowires at α near 15° with 5 keV Ar^+ resulted in the aligment of the nanowires perfectly parallel to each other [152].

Another process that could take place is spinodal decomposition. This kind of decomposition was reported to occur, under certain conditions, due to ion erosion [153-155] and could be responsible for the lateral distribution of Fe. The presence of regions with different Fe concentrations, in turn, may lead to differences in the local sputter rate, in similar way as in the cone and pyramid formation by seed materials [55, 56, 58, 59].

6.3. High incidence angles

At ion beam incidence angles α larger than 65°, different types of features evolve on the surface by ion erosion. As it was shown in section 5.2.3, at high incidence angles the re-sputtering rate of Fe from the sample is higher, thus leading to a lower concentration of Fe on the sample in the steady state.

At ion beam incidence angles between 65° to 85°, ripples perpendicular to the beam direction were formed at low fluences. These ripples are similar to the ripples formed at near normal incidence, i.e. they are similar in size, but their regularity is lower. They seem to be the ripples predicted by the models based on the BH model, which result from the interplay of curvature dependent sputtering and different relaxation mechanisms. However, after a certain erosion time, isolated protuberances oriented parallel to the beam direction and with higher amplitude were formed. It was shown that the amplitude, density on the surface, and length to width ratio of these protuberances increased with the time until they covered the entire surface. The amplitude of these protuberances, or columnar structures increased continuously in the fluence range analyzed, i.e. up to 6.7×10^{18} cm^{-2}. The observations are in agreement with the findings of Carter et al [5]. Although their experiments on silicon correspond to a different energy range (40 keV Ar$^+$), the topography at high incidence angles look very similar to that observed in this work. As the incidence angle was varied from 45° to 85°, they observed a transition from perpendicular-mode ripples to faceted parallel-oriented features. The parallel-type structures evolved first as isolated features; they compared them to stacked and tilted cylindrical segments. Like the features observed in this work, at higher angles their density on the surface and length to width ratio increased. The transition from perpendicular-mode ripples to parallel-mode features with the fluence has also been reported. For example, it was observed on silicon surfaces bombarded with Ar$^+$ by Brown and Erlebacher [4] (with low ion energy and high temperature), by

Keller et al. [45] (with low ion energy and relatively low temperature), and by Chini et al. [46] (with high ion energy).

It was demonstrated in this work that the columnar structures have specific facets upstream and downstream. Combining AFM and SEM measurements, it was shown that the angles between the ion beam and the facets were ~ 0° and ~ 90° for the upstream and downstream side, respectively. These observations suggest that the mechanism responsible for the formation of these columnar structures is the gradient dependent sputtering. Carter et al. [5] stated that the origin of the formation of the protuberances at large incidence angles was related to the presence of irregularities on the surface. In the results presented here, the ripples formed at low fluences would be the initiators. Local variations in the topography lead to variation in the local incidence angle and, in turn, in the sputtering yield and erosion rate. The gradient dependent sputtering dominates the topography evolution at high incidence angles but not at near normal incidence. The reason for that is related to the incidence angle dependence of the sputtering yield. In Fig. 4.17 and 5.8 the curve for the variation Y_{Si} with the incidence angle for Kr$^+$ was shown. It is observed that at low incidence angles $dY(\theta)/d\theta$ is small, while at high angles the slope of the curve is larger, i.e. $dY(\theta)/d\theta$ is larger. This means that small variations in the surface gradient produce large changes of Y and in turn in the local erosion rate. It was observed that as the incidence angle increased, the columnar structures evolved at lower fluences. This is also related to the $dY(\theta)/d\theta$; at larger incidence angles smaller local gradients are necessary to generate significant differences in the local erosion rate.

The observations agree with the predictions from Nobes et al. [147] that indicate that the most stable and probable of facets are normal and perpendicular to the ion beam. In subsection 4.3.2 their equation for the evolution of the surface slopes under ion erosion was presented.

Chapter 7
Summary and outlook

This study focuses on the self-organized pattern formation on Si(001) by Kr^+ erosion with energies up to 2000 eV, using a broad-beam ion source. Among the several erosion parameters that are involved in the pattern formation, here the ion beam incidence angle, ion energy, acceleration voltage, fluence, discharge voltage, operation time of the grid system, and grid distance were examined. Additionally, the simultaneous incorporation of Fe atoms during erosion was studied.

In the erosion facility used for this study, Fe atoms, together with other metals in lower concentrations, are sputtered from a stainless steel plate lining situated between the extraction system and the sample holder, and reach the sample together with the ions. Combining the results from simulations and measurements performed with RBS and SIMS it was shown that the flux of Fe atoms that reaches the substrate can be controlled by the ion beam divergence, which in turn is determined mainly by the acceleration voltage U_{acc} and ion energy E_{ion}. It was shown that the bombardment of the samples can be performed with or (almost) without co-sputtering of the stainless steel plate lining; i.e. with high and low ion beam divergence, respectively. It was also demonstrated after some minutes sputtering, a balance between the arrival of Fe atoms at the silicon substrate and its re-sputtering is achieved and the concentration of Fe remains constant. Due to its strong influence in the sputtering yield, the ion beam incidence angle can be used to regulate the concentration of Fe on the substrate.

It was shown in this study that when silicon surfaces were bombarded with low-energy ions without Fe incorporation (or very low Fe flux) no pattern evolved at incidence angles lower than ~ 65°. At higher incidence angles (α = 65° - 85°) different types of structures evolved. Perpendicular-mode ripples were formed first. They resemble those apparently generated by the interplay between curvature dependent sputtering and different relaxation mechanisms, predicted by most theoretical models based on Bradley and Harper model [37]. As the fluence increased, isolated protuberances oriented parallel to the beam direction evolved. Their density on the surface increased with the fluence until they covered the entire surface. They are faceted features showing two distinctive angles with respect to the ion beam, i.e. ~ 0° and ~ 90° on the upstream and

downstream, respectively. The dominant process responsible for the formation of these columnar structures seems to be the gradient dependent sputtering.

The evolution of the surface topography under ion erosion with Fe incorporation (with relatively high Fe flux) is different. Due to the high re-sputtering rate of Fe from the samples at high angles, the concentration of Fe at high incidence angles was observed to be low, and no significant effect on the topography evolution was observed with the incorporation of Fe atoms. However, at low angles, the evolution of the surface topography is affected. At this incidence angle range, ripples, dots or smooth surface were observed depending on the erosion conditions and with high Fe flux. The ripples, which are perpendicular to the ion beam direction and have a wavelength between ~ 40 nm – 70 nm and amplitude up to ~ 10 nm, are of special interest due to their relatively high regularity. With respect to the position of the Fe atoms in the samples, according to SIMS depth profile measurements, most of the Fe atoms are in the first 3 or 4 nm, and by HRTEM and EELS it was determined that they are situated mainly at the crest of the ripples.

In general, it was observed that when the concentration of Fe on the sample in the steady state was below ~ 0.5×10^{15} at cm^{-2} no pattern evolved while when it was above ~ 1.0×10^{15} at cm^{-2} nanostructures were formed.

The specific role of the Fe atoms has not been determined yet. One possibility could be the formation of iron silicides and their rearrangement by self-organization. Another possible process that may take place is spinodal decomposition [153-155], which would explain the lateral distribution of the Fe atoms. In turn, the non uniform [152] distribution of the Fe atoms on the surface may generate sputter protected areas, like in the case of seed cone formation [56, 57, 59, 156], which would lead to local differences in the sputter rate and high fluctuations on the surface.

It is evident that the role of Fe, and other surfactants, in the pattern formation should be further investigated. This issue is part of the current and future work of the Research Unit FOR-845, funded by the German Research Foundation (Deutsche Forschungsgemeintschaft). Different surfactants, miscible and inmiscible with silicon, are being studied.

List of acronyms and symbols

AES	Auger Electron Spectroscopy
AFM	Atomic Force Microscopy
BH	Bradley and Harper
ESD	Effective Surface Diffusion
EDX	Energy Dispersive X-Ray
EELS	Electron Energy Loss Spectroscopy
FFT	Fast Fourier Transform
FWHM	Full width at half maximum
GID	Grazing Incidence Diffraction
GISAXS	Grazing Incidence Small-Angle X-Ray Scattering
HRTEM	High Resolution Transmission Electron Microscopy
KPZ	Kardar-Parisi-Zhang
KS	Kuramoto-Sivashinsky
PIXE	Particle-Induced X-Ray Emission
PSD	Power spectral density
RBS	Rutherford Backscattering Spectrometry
RF	Radio frequency
RMS	Root mean square
RSF	Relative sensitivity factors
SEM	Scanning Electron Microscopy
SIMS	Secondary Ion Mass Spectrometry
SPIP	Scanning Probe Image Processor
SPM	Scanning Probe Microscopy
SR	Spectroscopy Reflectometry
SRIM	Stopping and range of ions in matter
STEM	Scanning Transmission Electron Microscopy
ToF	Time of Flight
WLI	White Light Interferometry
XPS	X-ray Photoelectron Spectroscopy

α	Ion beam incidence angle
θ	Local ion incidence angle
θ_c	Critical ion incidence angle (Bradley and Harper model)
θ_p	Ion incidence angle at which the sputtering yield is maximal
E_{ion}	Ion energy
U_{acc}	Acceleration voltage
U_b	Beam voltage
U_{scr}	Screen voltage
I_{dis}	Discharge current
U_{dis}	Discharge voltage
Φ	Fluence
j_{ion}	Ion current density
J	Ion flux
λ	Wavelength
ζ	System correlation length
Y	Sputter yield
a	Mean depth of the deposited energy
σ	Width of the deposited energy parallel to the ion beam
μ	Width of the deposited energy perpendicular to the ion beam
n	Atomic density
S	Stopping cross section
S_n	Nuclear stopping cross section
R	Average path length
R_p	Average projected length

References

[1] M. Navez, C. Sella, and D. Chaperot, C.R. Acad. Sci. **254**, 240 (1962).

[2] R. Gago, R. Cuerno, M. Varela, C. Ballesteros, and J. M. Albella, Appl. Phys. Lett. **78**, 3316 (2001).

[3] R. Gago, L. Vázquez, R. Cuerno, M. Varela, C. Ballesteros, and J. M. Albella, Nanotechnol. **13**, 304 (2002).

[4] A. D. Brown and J. Erlebacher, Phys. Rev. B **72**, 075350 (2005).

[5] G. Carter, M. J. Nobes, F. Paton, J. S. Williams, and J. L. Whitton, Radiat. Eff. Defects Solids **33**, 65 (1977).

[6] E. Chason, T. M. Mayer, B. K. Kellermann, D. N. McIlroy, and H. A. J, Phys. Rev. Lett. **72 (19)**, 3040 (1994).

[7] S. Facsko, T. Dekorsy, C. Koerdt, C. Trappe, H. Kurz, A. Vogt, and H. L. Hartnagel, Science **285** (5433), 1551 (1999).

[8] F. Frost, A. Schindler, and F. Bigl, Phys. Rev. Lett. **85 (19)**, 4116 (2000).

[9] C. Boragno, F. Buatier de Mongeot, G. Constantini, A. Molle, D. de Sanctis, and U. Valbusa, Phys. Rev. B **68**, 094102 (2003).

[10] D. Ghose, J. Phys.: Condens. Matter **21** (22), 224001 (2009).

[11] P. Karmakar and D. Ghose, Surf. Sci. **554**, L101 (2004).

[12] S. Rusponi, G. Constantini, C. Boragno, and U. Valbusa, Phys. Rev. Lett. **81** (13), 2735 (1998).

[13] A. Toma, B. Šetina Batič, D. Chiappe, C. Boragno, U. Valbusa, M. Godec, M. Jenko, and F. Buatier de Mongeot, J. Appl. Phys. **104**, 104313 (2008).

[14] U. Valbusa, C. Boragno, and F. Buatier de Mongeot, Mater. Sci. Eng., C **23**, 201 (2003).

[15] S. van Dijken, D. De Bruin, and B. Poelsema, Phys. Rev. Lett. **86** (20), 4608 (2001).

[16] A. Toma, F. Buatier de Mongeot, R. Buzio, G. Firpo, S. R. Bhattacharyya, C. Boragno, and U. Valbusa, Nucl. Instrum. Methods Phys. Res. B **230**, 551 (2005).

[17] D. Flamm, F. Frost, and D. Hirsch, Appl. Surf. Sci. **179**, 96 (2001).

[18] T. M. Mayer, E. Chason, and A. J. Howard, J. Appl. Phys. **76** (3), 1633 (1994).

[19] C. C. Umbach, R. L. Headrick, and K.-C. Chang, Phys. Rev. Lett. **87** (24), 246104 (2001).

[20] M. Cornejo, B. Ziberi, C. Meinecke, D. Hirsch, J. W. Gerlach, T. Höche, F. Frost, and B. Rauschenbach, Appl. Phys. A, (in Press) (2010).

[21] S. Macko, F. Frost, B. Ziberi, D. Förster, and T. Michely, Nanotechnol. **21** (08), 085301 (2010).

[22] G. Ozaydin, A. S. Özcan, Y. Wang, K. F. J. Ludwig, H. Zhou, R. L. Headrick, and D. P. Siddons, Appl. Phys. Lett. **87** (16), 163104 (2005).

[23] G. Ozaydin-Ince and K. F. J. Ludwig, J. Phys.: Condens. Matter **21** (22), 224008 (2009).

[24] J. A. Sánchez-García, R. Gago, R. Caillard, A. Redondo-Cubero, J. A. Martin-Gago, F. J. Palomares, M. Fernández, and L. Vázquez, J. Phys.: Condens. Matter **21**, 224009 (2009).

[25] J. A. Sánchez-García, L. Vázquez, R. Gago, A. Redondo-Cubero, J. M. Albella, and Z. Czigány, Nanotechnol. **19** (35), 355306 (2008).

[26] J. Erlebacher, M. J. Aziz, E. Chason, M. B. Sinclair, and J. A. Floro, Phys. Rev. Lett. **82 (11)**, 2330 (1999).

[27] S. Facsko, H. Kurz, and T. Dekorsy, Phys. Rev. B **63**, 165329 (2001).

[28] D. Carbone, A. Alija, O. Plantevin, R. Gago, S. Facsko, and T. H. Metzger, Nanotechnol. **19** (03), 035304 (2008).

[29] B. Ziberi, *Ion Beam Induced Pattern Formation on Si and Ge Surfaces*. (Engelsdorfer Verlag, Leipzig, 2007).

[30] F. J. Ludwig, C. R. J. Eddy, O. Malis, and R. L. Headrick, Appl. Phys. Lett. **81**, 2770 (2002).

[31] B. Ziberi, F. Frost, T. Höche, and B. Rauschenbach, Phys. Rev. B **72** (23), 235310 (2005).

[32] B. Ziberi, F. Frost, H. Neumann, and B. Rauschenbach, Appl. Phys. Lett. **92** (06), 063102 (2008).

[33] B. Ziberi, F. Frost, M. Tartz, H. Neumann, and B. Rauschenbach, Thin Solid Films **459**, 106 (2004).

[34] F. Frost and B. Rauschenbach, Appl. Phys. A **77**, 1 (2003).

[35] T. K. Chini, M. K. Sanyal, and S. R. Bhattacharyya, Phys. Rev. B **66**, 153404 (2002).

[36] K. Zhang, F. Rotter, M. Uhrmacher, C. Ronning, H. Hofsäss, and J. Krauser, Surf. Coat. Technol. **201**, 8299 (2007).

[37] R. M. Bradley and J. M. E. Harper, J. Vac. Sci. & Technol. A **6 (4)**, 2390 (1988).

[38] B. Ziberi, F. Frost, T. Höche, and B. Rauschenbach, Vac. **81**, 155 (2006).

[39] B. Ziberi, F. Frost, and B. Rauschenbach, Appl. Phys. Lett. **88** (17), 173115 (2006).

[40] C. S. Madi, H. Bola George, and M. J. Aziz, J. Phys.: Condens. Matter **21** (22), 224010 (2009).

[41] S. Habenicht, K. P. Lieb, J. Koch, and A. D. Wieck, Phys. Rev. B **65** (11), 115327 (2002).

[42] C. S. Madi, B. Davidovitch, H. Bola George, S. A. Norris, M. P. Brenner, and M. J. Aziz, Phys. Rev. Lett. **101** (24), 246102 (2008).

[43] G. Ozaydin, F. J. Ludwig, H. Zhou, L. Zhou, and R. L. Headrick, J. Appl. Phys. **103** (03), 033512 (2008).

[44] R. Gago, L. Vázquez, O. Plantevin, J. A. Sánchez-García, M. Varela, C. Ballesteros, J. M. Albella, and T. H. Metzger, Phys. Rev. B **73** (15), 145414 (2006).

[45] A. Keller, S. Roßbach, S. Facsko, and W. Möller, Nanotechnol. **19**, 135303 (2008).

[46] T. K. Chini, D. P. Datta, and S. R. Bhattacharyya, J. Phys.: Condens. Matter **21** (22), 224004 (2009).

[47] F. Frost, R. Fechner, B. Ziberi, J. Völlner, D. Flamm, and A. Schindler, J. Phys.: Condens. Matter **21**, 224026 (2009).

[48] B. Ziberi, F. Frost, and B. Rauschenbach, Appl. Phys. Lett. **87**, 033113 (2005).

[49] B. Ziberi, F. Frost, B. Rauschenbach, and T. Höche, Surf. Sci. **600**, 3757 (2006).

[50] M. Cornejo, B. Ziberi, M. Tartz, H. Neumann, F. Frost, and B. Rauschenbach, "Importance of internal ion beam parameters on the self-organized pattern formation with low-energy broad beam ion sources", in *MRS Spring Meeting*, edited by D Ila, P K Chu, J K N Lindner, N Kishimoto, and J E E Baglin (Materials Research Society, San Francisco, 2009), Vol. 1181, pp. 9.

[51] J. Erlebacher, M. J. Aziz, E. Chason, M. B. Sinclair, and J. A. Floro, J. Vac. Sci. & Technol. **A 18**, 115 (2000).

[52] B. Ziberi, M. Cornejo, F. Frost, and B. Rauschenbach, J. Phys.: Condens. Matter **21**, 224003 (2009).

[53] M. Cornejo, J. Völlner, B. Ziberi, F. Frost, and B. Rauschenbach, "Ion beam sputtering, a route for fabrication of highly ordered nanopatterns", in *New trends in the fabrication and*

characterization of micro- and sub- micrometer three dimensional structures, edited by A F Lasagni and F A Lasagni (Springer-Verlag (in Press), Berlin-Heidelberg, 2010).

[54] S. Hazra, T. K. Chini, M. K. Sanyal, J. Grenzer, and U. Pietsch, Phys. Rev. B **70** (12), 121307 (2004).

[55] A. Güntherschulze and W. Tollmien, Z. Phys. **119**, 685 (1942).

[56] X. L. Ma, N. G. Shang, Q. Li, I. Lee, I. Bello, and S. T. Lee, J. Cryst. Growth **234**, 654 (2002).

[57] G. K. Wehner, J. Vac. Sci. & Technol. A **3** (4), 1821 (1985).

[58] G. K. Wehner and D. J. Hajicek, J. Appl. Phys. **42 (3)**, 1145 (1971).

[59] S. Morishita, Y. Fujimoto, and F. Okuyama, J. Vac. Sci. & Technol. A **6** (2), 217 (1988).

[60] G. Ozaydin, F. J. Ludwig, W. Zhou, and R. L. Headrick, J. Vac. Sci. & Technol. B **26** (2), 551 (2008).

[61] G. Ozaydin, A. S. Özcan, Y. Wang, F. J. Ludwig, H. Zhou, and R. L. Headrick, Nucl. Instrum. Methods Phys. Res. B **264**, 47 (2007).

[62] H. Hofsäss and K. Zhang, Appl. Phys. A **92**, 517 (2008).

[63] H. Hofsäss and K. Zhang, Nucl. Instrum. Methods Phys. Res. B **267**, 2731 (2009).

[64] J. Kim, D. G. Cahill, and R. S. Averback, Phys. Rev. B **67**, 045404 (2003).

[65] M. Nozu, M. Tanemura, and F. Okuyama, Surf. Sci. Lett. **304**, L468 (1994).

[66] M. Tanemura, S. Aoyama, Y. Fujimoto, and F. Okuyama, Nucl. Instrum. Methods Phys. Res. B **61**, 451 (1991).

[67] F. Frost, R. Fechner, D. Flamm, B. Ziberi, W. Frank, and A. Schindler, Appl. Phys. A **78**, 651 (2004).

[68] F. Buatier de Mongeot and U. Valbusa, J. Phys.: Condens. Matter **21** (22), 224022 (2009).

[69] A. Toma, D. Chiappe, B. Šetina Batič, M. Godec, M. Jenko, and F. Buatier de Mongeot, Phys. Rev. B **78**, 153406 (2008).

[70] M. Stepanova and S. K. Dew, J. Phys.: Condens. Matter **21** (22), 224014 (2009).

[71] K. Zhang, M. Uhrmacher, H. Hofsäss, and J. Krauser, J. Appl. Phys. **103** (08), 083507 (2008).

[72] H. Gnaser, *Low-energy ion irradiation of solid surfaces*. (Springer-Verlag, Berlin-Heidelberg, 1999).

[73] R. Hellborg, H. J. Whitlow, and Y. Zhang (eds), *Ion beams in nanoscience and technology*. (Springer-Verlag, Berlin-Heidelberg, 2009).

[74] P. Sigmund, "Sputtering by Ion Bombardment: Theoretical Concepts", in *Sputtering by Particle Bombardment I*, edited by R Behrisch (Springer-Verlag, Berlin-Heidelberg, 1981), Vol. 47, pp. 9.

[75] R. Behrisch and K. Wittmaack (eds), *Sputtering by particle bombardment III. Characteristics of sputtered particles, technical applications*. (Springer Verlag, Berlin Heidelberg, 1991).

[76] P. Sigmund, Phys. Rev. **184**, 383 (1969).

[77] P. Sigmund, J. Mater. Sci. **8**, 1545 (1973).

[78] R. Cuerno, H. A. Makse, S. Tomassone, S. T. Harrington, and H. E. Stanley, Phys. Rev. Lett. **75** (24), 4464 (1995).

[79] I. Koponen, M. Hautala, and O.-P. Sievänen, Phys. Rev. Lett. **78**, 2612 (1997).

[80] I. Koponen, M. Hautala, and O.-P. Sievänen, Phys. Rev. B **54**, 13502 (1996).

[81] www.srim.org.

[82] J. F. Ziegler, J. P. Biersack, and U. Littmark, *The Stopping and Range of Ions in Solid*. (Pergamon, New York, 1985).

[83] G. Carter and V. Vishnyakov, Phys. Rev. B **54**, 17647 (1996).

[84] M. Castro, R. Cuerno, L. Vázquez, and R. Gago, Phys. Rev. Lett. **94**, 016102 (2005).

[85] S. Facsko, T. Bobek, A. Stahl, H. Kurz, and T. Dekorsy, Phys. Rev. B **69**, 153412 (2004).

[86] M. A. Makeev, R. Cuerno, and A.-L. Barabási, Nucl. Instrum. Methods Phys. Res. B **197**, 185 (2002).

[87] S. Park, B. Kahng, H. Jeong, and A.-L. Barabási, Phys. Rev. Lett. **83** (17), 3486 (1999).

[88] M. Rost and J. Krug, Phys. Rev. Lett. **75** (21), 3894 (1995).

[89] S. Vogel and S. Linz, Phys. Rev. B **72**, 035416 (2005).

[90] R. Cuerno and A.-L. Barabási, Phys. Rev. Lett. **74**, 4746 (1995).

[91] Y. Kuramoto and T. Tsuzuki, Prog. Theor. Phys. **55**, 356 (1977).

[92] G. I. Sivashinsky, Acta Astronaut. **6**, 569 (1979).

[93] C. Misbah and A. Valance, Phys Rev E **49**, 166 (1994).

[94] S. Vogel and S. Linz, Europhys. Lett. **76**, 884 (2006).

[95] M. A. Makeev and A.-L. Barabási, Appl. Phys. Lett. **71** (19), 2800 (1997).

[96] H. H. Andersen, Appl. Phys. **18**, 131 (1979).

[97] G. Carter, M. J. Nobes, C. Cave, and N. Al-Qadi, Vac. **45**, 71 (1994).

[98] J. M. E. Harper, J. J. Cuomo, and H. R. Kaufman, Annu. Rev. Mater. Sci. **13**, 413 (1983).

[99] H. R. Kaufman, J. J. Cuomo, and J. M. E. Harper, J. Vac. Sci. & Technol. **21**, 725 (1982).

[100] H. Neumann, M. Tartz, F. Scholze, T. Chassé, H. Kersten, and H. Leiter, Contrib. Plasma Phys. **47** (No. 7), 487 (2007).

[101] M. Zeuner, H. Neumann, F. Scholze, D. Flamm, M. Tartz, and F. Bigl, Plasma Sources Sci. Technol. **7**, 252 (1998).

[102] R. Becker and W. B. Herrmannsfeldt, Rev. Sci. Instrum. **63**, 2756 (1992).

[103] M. Tartz, E. Hartmann, and H. Neumann, Rev. Sci. Instrum. **79**, 02B905 (2008).

[104] G. Aston and P. J. Wilbur, J. Appl. Phys. **52(4)**, 2614 (1981).

[105] M. Tartz, *Simulation des Ladungstransportes in Breitstrahlionenquellen* (PhD Thesis. Leipzig, 2003).

[106] M. Tartz, R. Deltschew, E. Hartmann, and H. Neumann, Surf. Coat. Technol. **142-144**, 34 (2001).

[107] M. Zeuner, J. Meichsner, H. Neumann, F. Scholze, and F. Bigl, J. Appl. Phys. **80**, 611 (1996).

[108] http://www.mikropack.de/e/tfm/refle/applications.html.

[109] G. J. Legget, "Scanning Tunneling Microscopy and Atomic Force Microscopy", in *Surface Analysis: The Principal Techniques*, edited by J C Vickerman (John Wiley & Sons, Chichester, 1997), pp. 393.

[110] S. N. Magonov and N. A. Yerina, "Visualization of Nanostructures with Atomic Force Microscopy", in *Handbook of Microscopy for Nanotechnology*, edited by N Yao and Z L Wang (Springer, Berlin, 2005), pp. 113

[111] K. S. Birdi, *Scanning Probe Microscopes: Applications in Science and Technology*. (CRC Press, Boca Raton, 2003).

[112] Y. Sugawara, "Atomic Force Microscopy", in *Roadmap of Scanning Probe Microscopy*, edited by S Morita (Springer, Berlin - Heidelberg, 2007), pp. 15.

[113] J. E. Castle and P. A. Zhdan, J. Phys. D: Appl. Phys. **30**, 722 (1997).

[114] http://www.bruker-axs.com/atomic_force_microscopes.html.

[115] http://www.asylumresearch.com/Products/Products.shtml.

[116] Image Metrology A/S, (http://www.imagemet.com).

[117] http://probe.olympus-global.com/en/.

[118] Y. Zhao, G.-C. Wang, and T.-M. Lu, *Characterization of Amorphous and Crystalline Rough Surface: Principles and Applications*. (Academic Press, London, 2001).

[119] E. A. Eklund, E. J. Snyder, and R. S. Williams, Surf. Sci. **285**, 157 (1993).

[120] F. R-PSD developed by Frost and A. Nickel, ((IOM Leipzig)).

[121] A. Duparré, J. Ferre-Borrull, S. Gliech, G. Notni, J. Steinert, and J. M. Bennet, Appl. Optics **41** (1), 154 (2002).

[122] D. K. Schroder, *Semiconductor material and device characterization*. (John Wiley & Sons, Inc., Hoboken, New Jersey, 2006), 3rd ed.

[123] B. G. Yacobi, D. B. Holt, and L. L. Kazmerski, "Scanning Electron Microscopy", in *Microanalysis of solids*, edited by B G Yacobi, D B Holt, and L L Kazmerski (Plenum Press, New York, 1994), pp. 25.

[124] P. S. Turner, C. E. Nockolds, and S. Bulcock, "Electron Microscope Techniques for Surface Characterization", in *Surface Analysis Methods in Materials Science*, edited by D J O'Connor, B A Sexton, and R St C Smart (Springer-Verlag, Berlin Heidelberg, 2003), pp. 85.

[125] H. Czichos, T. Saito, and L. Smith (eds), *Springer Handbook of Materials Measuremtent Methods*. (Srpinger-Verlag, Heidelberg, 2006).

[126] http://www.zeiss.de.

[127] A. J. Garrat-Reed, "Transmission Electron Microscopy", in *Microanalysis of Solids*, edited by B G Yacobi, D B Holt, and L L Kazmerski (Plenum Press, New York, 1994).

[128] N. Yao and Z. L. Wang (eds), *Handbook of microscopy for nanotechnology*. (Kluwer Academics Publishers, New York, 2005).

[129] A. I. Kirkland and J. L. Hutchison (eds), *Nanocharacterisation* (RSC Publishing, Cambridge, 2007).

[130] C. C. Ahn (ed), *Transmission Electron Energy Loss Spectrometry in Materials Science and the EELS ATLAS*. (Wiley-VCH Verlag GmbH & Co, Weinheim, 2004), 2nd ed.

[131] R. J. MacDonald and B. V. King, "SIMS - Secondary Ion Mass Spectrometry", in *Surface analysis methods in materials science*, edited by D J O'Connor, B A Sexton, and R St C Smart (Springer, Berlin Heidelberg, 2003), pp. 127.

[132] D. McPhail and M. Dowsett, "Dynamic SIMS", in *Surface Analysis: The Principal Techniques*, edited by J C Vickerman and I Gilmore (John Wiley & Sons, Manchester, 2009).

[133] E. Niehuis and T. Grehl, "Dual Beam Depth Profiling", in *ToF-SIMS: Surface Analysis by Mass Spectrometry*, edited by J C Vickerman and D Briggs (IM Publications and SurfaceSpectra Limited, Chichester, West Sussex and Manchester, 2001).

[134] J. C. Vickerman and D. Briggs (eds), *ToF-SIMS Surface Analysis by Mass Spectrometry*. (IM Publications and Surface Spectra Limited, Chichester, West Sussex and Manchester, 2001).

[135] J. C. Vickerman and A. J. Swift, "Secondary Ion Mass spectrometry - the Surface Mass Spectrometry", in *Surface Analysis: The Principal Techniques*, edited by J C Vickerman (John Wiley & Sons, Chichester, 1997).

[136] R. G. Wilson, Int. J. Mass Spectrom. Ion Process. **143**, 43 (1995).

[137] A. Climent-Font, M. T. Fernández-Jimenez, U. Wätjen, and J. Perrière, Nucl. Instrum. Methods Phys. Res. A **353**, 575 (1994).

[138] J. A. Davies and R. Siegele, "High Energy Heavy Ion RBS, ERDA and Channelling", in *Application of Particle and Laser Beams in Materials Technology*, edited by P Misaelides (Kluwer Academic Publishers, Dordrecht, 1995), pp. 341

[139] E. Taglauer, "Low-energy Ion Scattering and Rutherford Backscattering", in *Surface Analysis: The Principal Techniques*, edited by J C Vickerman (John Wiley & Sons, Chichester, 1997), pp. 215.

[140] H. R. Verma, *Atomic and Nuclear Analytical Methods. XRF, Mössbauer, XPS, NAA and Ion-Beam Spectroscopic Techniques*. (Springer, Berlin Heidelberg, 2007).

[141] S. A. E. Johansson, J. L. Campbell, and K. G. Malmqvist (eds), *Particle-Induced X-Ray Emission Spectrometry (PIXE)*. (John Wiley & Sons, New York, 1995).

[142] T. Butz, R.-H. Flagmeyer, J. Heitmann, D. N. Jamieson, G. J. F. Legge, D. Lehmann, U. Reibetanz, T. Reinert, A. Saint, D. Spemann, R. Szymanski, W. Tröger, J. Vogt, and J. Zhu, Nucl. Instrum. Methods Phys. Res. B **161-163**, 323 (2000).

[143] D. J. W. Mous, R. G. Haitsma, T. Butz, R.-H. Flagmeyer, D. Lehmann, and J. Vogt, Nucl. Instrum. Methods Phys. Res. B **130**, 31 (1997).

[144] L. R. Doolittle, Nucl. Instrum. Methods Phys. Res. B **9** (3), 344 (1985).

[145] http://nmp.csiro.au/GeoPIXE.html.

[146] C. G. Ryan, Nucl. Instrum. Methods Phys. Res. B **181**, 170 (2001).

[147] M. J. Nobes, J. S. Colligon, and G. Carter, J. Mater. Sci. **4**, 730 (1969).

[148] W. Eckstein, Radiat. Eff. Defects Solids **130**, 239 (1994).

[149] G. K. Wehner, Appl. Phys. Lett. **43**, 366 (1983).

[150] D. Carbone, A. Biermanns, B. Ziberi, F. Frost, O. Plantevin, U. Pietsch, and T. H. Metzger, J. Phys.: Condens. Matter **21** (22), 224007 (2009).

[151] S. Liang, R. Islam, D. J. Smith, P. A. Bennett, J. R. O'Brien, and B. Taylor, Appl. Phys. Lett. **88**, 113111 (2006).

[152] T. I. Kamins and Y.-L. Chang, United States Patent No. US 6,248,674 B1 (2001).

[153] F. A. Garner, H. R. Brager, R. A. Dodd, and T. Lauritzen, Nucl. Instrum. Methods Phys. Res. **B16**, 244 (1986).

[154] V. S. Khmelevskaya, V. G. Malynkin, and S. P. Solov'ev, Phase. Transit. **29**, 157 (1991).

[155] M. S. Veshchunov and L. V. Matveev, Atomic Energy **76**, 29 (1994).

[156] C. S. Bhatia, Thin Solid Films **96**, 249 (1982).